UNIVERSITY OF CALIFORNIA SAN DIEGO

How a landscape responds to changes in the world around it: The Dynamic Critical Zone in the Luquillo Mountains, Puerto Rico

A dissertation submitted in partial satisfaction of the
requirements for the degree
Doctor of Philosophy

in

Earth Sciences

by

Emma Jayne Harrison

Committee in charge:

Professor Jane K. Willenbring, Chair
Professor Adrian Borsa
Professor Elsa Cleland
Professor Neal Driscoll
Professor Isabel Rivera-Collazo

2020

The Dissertation of Emma Jayne Harrison is approved, and it is acceptable in quality and form for publication on microfilm and electronically:

_____

_____

_____

_____

_____
Chair

University of California San Diego

2020

DEDICATION

The nights I spent in the rivers with the fireflies and the coquis made everything worth it.

TABLE OF CONTENTS

LIST OF FIGURES

LIST OF TABLES

ACKNOWLEDGEMENTS

This dissertation work was conducted on stolen and occupied Kumeyaay, Lenape, and Taino land. As a researcher working in Puerto Rico, a colonial territory of the United States, I acknowledge the role that colonialism and Western academic institutions play in structural violence against land and its people today. I honour the Boriken people for their work of collective rebuilding and mutual relief in the disastrous wake of Hurricane Maria in 2017.

I would like to acknowledge and thank the members of my dissertation committee for their guidance, support, and availability. I extend my thanks as well to Dr. Ron Dorn and Dr. Ben Crosby for their good mentorship. Without a doubt, my co-authors are the best in the world: Dr. Gilles Brocard, Dr. Nicole Gasparini, and Dr. Nathan Lyons. They have been excellent mentors and even better friends.

Thank you to the numerous field assistants who have survived with me, and to the undergraduates who I had the invaluable opportunity to mentor and teach. I've been blessed to see many iterations of the Willenbring Lab Group – and every person in it has been a unique character and a good friend to me. I send love and support to my comrades in the graduate school at UPENN and in my new home at Scripps Institution of Oceanography.

Thank you to the community gardeners in West Philadelphia and my neighbours and friends on the best little block in the world: South Saint Bernard St.

Thank you to CIEJ, my colectivo, for teaching me, keeping me inspired, grounded, and doing things that matter with people that I love. Thank you to the communities of Salinas Grande and Coyo for working with us and inviting us to join their struggle.

This work would not have been possible without the wonderful community of the Luquillo Critical Zone Observatory, whose excellence in research is only exceeded by their vibes. This would also not have been possible without the people in Puerto Rico who have become my great friends and adventure partners.

To my family: Jon, Jennifer, Michael, Kathleen, Julian and Ursula. To my best friend Tiffany Hinchey. To Laura, to Aurora, to Vinayak, Marisa, Ian, Bianca, Olivia, sweet Yuki, and my maiti Jon. And most of all, thank you Dr. Jane Willenbring!

Chapter two has been submitted for publication and has been accepted with revisions in the Journal of Geophysical Research: Earth Surface and will appear as: Harrison, E. J., Brocard, G. Y., Gasparini, N. M., Lyons, N. J., and Willenbring, J. K. Dynamic Critical Zone architecture driven by subsurface flow in the Luquillo Mountains, Puerto Rico. *Journal of Geophysical Research: Earth Surface.* (2020). The dissertation author was the primary investigator and author of this paper.

Chapter three has been prepared for submission to the journal Quaternary Science Reviews and may appear as: Harrison, E. J., Brocard, G. Y. and Willenbring, J. K., Quaternary record of terrestrial environmental change in response to climatic forcing and anthropogenic perturbations. *Quaternary Science Reviews.* (2020). The dissertation author was the primary investigator and author of this paper.

Chapter four has been prepared for submission to the journal Nature and may appear as: Harrison, E. J., Brocard, G. Y. and Willenbring, J. K. Global rates of soil production independent of soil depth. *Nature*. (2020). The dissertation author was the primary investigator and author of this paper.

VITA

2020 Doctor of Philosophy, Scripps Institution of Oceanography, University of California San Diego

2013 Master of Arts, Geographical Science and Urban Planning, Arizona State University

2011 Bachelor of Science, Geographical Science and Urban Planning, Arizona State University, Honors College

PUBLICATIONS

Brito-Millán, M., Cheng, A., **Harrison, E.,** Mendoza Martinez, M., Sugla, R., Belmonte, M., Salomón, A., Quintanilla, L., Guzman-Morales, J., Martinez, A. (2019) *No Comemos Baterías*: Solidarity Science Against False Climate Change Solutions. *Science for the People Magazine,* 22:1

Harrison, E., R.I. Dorn (2013), Introducing a terrestrial carbon pool in warm desert bedrock mountains. *Global Biogeochemical Cycles, 28(3),* 253-268.

Larson, P., R. Dorn, R. Palmer, Z. Bowles, **E. Harrison**, S. Kelley, M. Schmeeckle, J. Douglass (2014), Pediment response to drainage basin evolution in south-central Arizona. *Physical Geography, 35*, 369-389.

Larson, P., **E. Harrison**, R. Palmer, eds. (2013) *Introductory Physical Geography 11th edition*. Haven McNeil LLC., Arizona State University, 28, 253-268.

Dorn, R. I., J. Dorn, **E. Harrison**, E. Gutbrod, S. Gibson, P. Larson, N. Cerveny, N. Lopat, K. M. Groom, and C. D. Allen (2012), Case hardening vignettes from the western USA: Convergence of form as a result of divergent hardening processes, *Association of Pacific Coast Geographers Yearbook*, *74*, 1-12.

Dorn, R.I., S.J. Gordon, C.D. Allen, N. Cerveny, J.C. Dixon, K.L. Groom, K. Hall, **E. Harrison**, L. Mol, T.R. Paradise, P. Sumner, T.J. Thompson (2012), The role of fieldwork in rock-decay research: case studies from the fringe, Special Issue: Binghamton 2012

FIELDS OF STUDY

Major Field: Geoscience

Studies in Geography

Studies in Remote Sensing

ABSTRACT OF THE DISSERTATION

How a landscape responds to changes in the world around it:
The Dynamic Critical Zone in the Luquillo Mountains, Puerto Rico

by

Emma Jayne Harrison

Doctor of Philosophy in Earth Sciences

University of California San Diego, 2020

Professor Jane K. Willenbring, Chair

The processes that shape Earth's surface are constantly in flux. Continuous movements of soil and water and growth of ecosystems are what create the perfect stillness in Ansel Adam's landscapes. In this dissertation, we investigate how a landscape responds to changes in the world around it. The tectonic uplift of Puerto Rico continues to shape the critical zone of the Luquillo Mountains today. We find that it has modified patterns of groundwater emergence, such that the river network is entrenching into ridgelines, in part, via the flux of groundwater. We demonstrate this with measurements of groundwater discharge and the grain size of the sediment it carries,

compared to long-term channel incision rates derived with the cosmogenic radionuclide ^{10}Be. Rock uplift enhances erosion rates, and a long-held belief in Earth Science is that soil production processes are linked and will respond to an enhanced erosive flux. By applying ^{10}Be dating to measure soil production rates in the evolving landscape of the Luquillo Mountains, we determined that there is no such functional relationship. We re-evaluated the methods and assumptions that have been applied to this question elsewhere, and determined that in fact, soil production is independent of soil depth across the globe. This implies that no safety net will save us from the massive loss of soil due to anthropogenically accelerated erosion. Even outside of managed landscapes, accelerated erosion under climate change is an imminent possibility. We demonstrate this with a record of physical erosion over 26 ky recorded by ^{10}Be concentrations in the layers of floodplain sediments. Erosion rates are greatly accelerated by the predominance of landsliding that occurs due to the onset of intense, frequent tropical storms in the Caribbean. The floodplain sediments contain a contemporaneous record of ecosystem dynamics in the δ^{13}C isotope ratios of buried organic material. Similar to physical erosion in the watershed, ecological dynamics shift to a disturbance-dominated state due to coupling with a more volatile climate.

CHAPTER 1

INTRODUCTION

1. BACKGROUND

1.1. Geomorphology and the Critical Zone

"The only constant in life is change" -Heraclitus of Ephesus (c. 500 BCE)

Interactions and feedbacks functionally link all the natural systems co-operating in Earth's landscapes. Science in the "critical zone" adopts a holistic framework for integrating research disciplines that have historically existed as discrete entities. The critical zone is defined spatially as the boundary layer between the atmosphere and the deep solid Earth. It is often referred to as living, evolving, because it is a locus of energetic chemical, biological and physical transformations (Amundson, Richter, Humphreys, Jobbágy, & Gaillardet, 2007; Brantley, Goldhaber, & Vala Ragnarsdottir, 2007; Chorover, Kretzschmar, Garica-Pichel, & Sparks, 2007). This dissertation adopts the framework of critical zone science through the study of multiple Earth systems allied in a single environment: the Luquillo Mountains of Puerto Rico. The focus of this research is understanding the feedbacks between geomorphic processes and the soil, water and ecosystems in the Luquillo Mountains critical zone.

Geomorphology is scientific investigation of the origin and evolution of landforms on Earth's surface and has been well described as the "science of scenery" (@jkwillenbring). Geomorphic processes are those that generate and shape the physical features of Earth, which may be broadly organized as uplift, weathering, and erosion. Rock uplift generates relief. Weathering disintegrates rock material. Erosion removes rock material and reduces relief. The style and rate

of each process may change over time as a function of the others. For example, rapid uplift is hypothesized to accelerate weathering rates (Raymo & Ruddiman, 1992) and favour mass wasting erosion over diffusive transport (Larsen & Montgomery, 2012; Roering et al., 2015). Landscapes in geomorphic equilibrium are places where the rate of long-term rock uplift is balanced everywhere by an equal rate of denudation - the summed mass lost though weathering and erosion (Hack, 1960). Disequilibrium, or the exceedance of one geomorphic process over another, may be induced by any number of perturbations to the boundary conditions that set the parameter space for geomorphic processes.

Geomorphic disequilibrium causes structural change in landforms (Hurst, Mudd, Attal, & Hilley, 2013). In an illustration of a two-dimensional hillslope, the slope is set by the elevation and horizontal position of the peak and the base – these are the boundary conditions. A climatological perturbation might raise sea level or a tectonic perturbation might raise the peak. Either process will affect the vertical and horizontal distance between the peak and the base, forcing a response in the slope of the profile. The regrading of the hillslope is accomplished through increased erosion (Roering, Kirchner, & Dietrich, 1999). Thus, the boundary conditions and the rates of geomorphic processes are linked in a given landscape.

In this thesis, we focus on the transmission of external perturbations to critical zone systems through geomorphic processes. Although this has rarely been studied explicitly, the results of this feedback are potent where it has been observed. In the Luquillo Mountains, a tectonically-triggered erosion wave controls the spatial pattern of plant-available nutrients in soil (Porder et al., 2015) and has restructured the forest canopy (Wolf, Brocard, Willenbring, Porder, & Uriarte, 2016). In intensively managed landscapes, anthropogenically accelerated erosion alters nutrient cycles and triggers locust outbreaks (Cease et al., 2012). Landslides impacting fluvial dynamics have been

shown to cause genetic divergence in fish populations (Mackey, Roering, & Lamb, 2011). Even the life history of the iconic Puerto Rican coqui frog was altered by geomorphic processes, as the uplift of the island separated populations and drove their subsequent speciation (Barker, Rodríguez-Robles, & Cook, 2015).

1.2. **The Luquillo Mountains**

Research for this dissertation was conducted entirely within the Luquillo Mountains of north-eastern Puerto Rico. This site has a long research tradition. It has been home to the International Institute of Tropical Forestry (IITF) since 1939, a Long Term Ecological Research (LTER) site since 1988, and the Luquillo Critical Zone Observatory (LCZO) since 2009. Recently, the imprints of Puerto Rico's tectonic history in the landscape of the Luquillo Mountains was described by Brocard et al. (2015, 2016). In the mid-Miocene, Puerto Rico was a subsiding, low-relief carbonate reef (Van Gestel, Mann, Grindlay, & Dolan, 1999). Approximately 4 My ago tilting uplifted the island and generated ~600 m of relief rapidly, in 14-40 ky (Ten Brink, 2005). A wave-cut terrace of the former shoreline is preserved as a notch in the Luquillo Mountains topography (Figure 1) (Brocard, Willenbring, Scatena, & Johnson, 2015).

Rock uplift – or baselevel fall – triggers waves of enhanced erosion that propagate though river networks (Brocard, Willenbring, Miller, & Scatena, 2016; Crosby & Whipple, 2006). Increased erosion rates are transmitted upstream via the migration of knickpoints, or sharp breaks in the stream gradient (Kirby & Whipple, 2012). Geomorphic adjustment has not occurred uniformly across the topography of the Luquillo Mountains, most likely due to geological factors. Bedrock lithologies in the Luquillo Mountains are interbedded volcanoclastic rocks intruded by a quartz diorite pluton (Seiders, 1971). The volcanoclastic lithologies weather approximately three times faster than the quartz diorite (Dosseto, Buss, & Suresh, 2011). In watersheds that are

underlain entirely by volcanoclastic rocks, stream profiles are low-gradient and concave-up and the hillslope morphology preserves no evidence of geomorphic disequilibrium (Pike, Scatena, & Wohl, 2010). Any knickpoint migration or hillslope adjustment triggered by the uplift of Puerto Rico has already propagated through the entirety of these watersheds.

The relatively resistant quartz diorite has impeded the erosion wave traveling up the Rio Blanco (Brocard et al. 2016). Brocard et al. (2015) identify a boundary in the Rio Blanco watershed at the frontline of knickpoint propagation in the river network. At this erosion front, sharp knickpoints separate concave-up alluvial stream reaches with limited stream power from steep bedrock lined channels (Figure 2). The erosion front separates a zone of slowly eroding "relict" topography from rapidly eroding, steep topography that is adjusting to the new baselevel (Whipple, DiBiase, & Crosby, 2013). The Rio Blanco watershed, and the Luquillo Mountains as a whole, are a landscape divided into a patchwork of domains eroding at different rates due to this tectonic perturbation. Much of this thesis exploits the contrast in geomorphic processes across these differently affected domains.

Figure 1 – A view of the Luquillo Mountains with an arrow pointing to the notch left by the wave-cut terrace of the former shoreline.

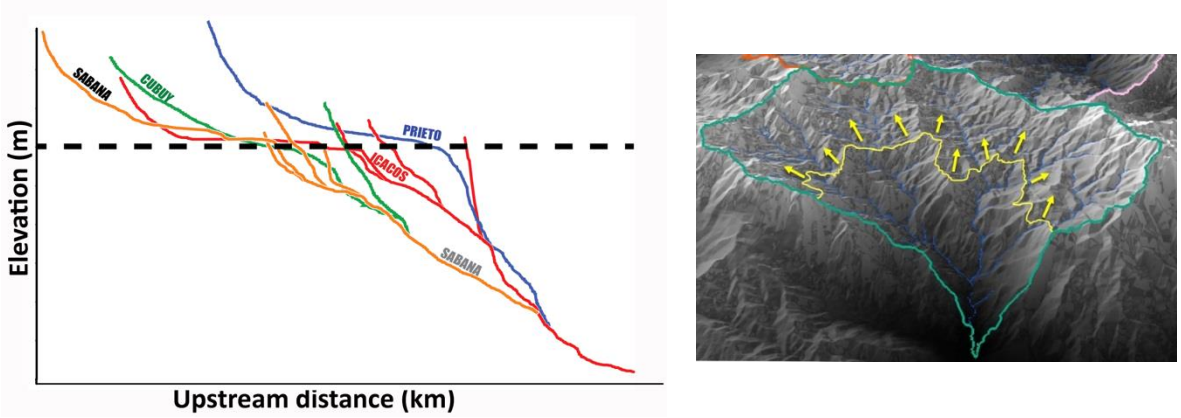

Figure 2 – Left: River long profiles. Long profiles of the major tributary rivers forming the Rio Blanco watershed. The names of each tributary channel appear next to their respective profiles. The dashed line represents the upstream extent of knickpoint propagation. Right: An oblique view of a LiDAR DEM. The extent of the Rio Blanco watershed is delineated by the green line. The yellow line demarks the erosion front in the topography. Yellow arrows annotate the direction of erosion front migration

1.3. Cosmogenic ^{10}Be

We develop many of the datasets in this thesis using the cosmogenic radionuclide ^{10}Be as a tracer of physical and chemical erosion. Cosmogenic radionuclides have exceptional utility in Earth Surface processes because they typically do not exist in Earth materials prior to exposure to cosmic radiation (Von Blanckenburg & Willenbring, 2014). Therefore, the accumulation of these nuclides is directly related to how long they have been exposed to radiation, i.e. the length of time they have spent in the near surface (Lal, 1991). ^{10}Be is a cosmogenic radionuclide of Beryllium. It is radioactive, and decays with a half-life of 1.39 Ma (Chmeleff, von Blanckenburg, Kossert, & Jakob, 2010). Radioactive elements are useful tracers of processes operating at timescales similar to the nuclide half-life (Dunai, 2010). Measurements of mass fluxes recorded through ^{10}Be dating may be accurately reported using unit measurements such as mm ky^{-1} or tons km^{-2} yr^{-1}. This spatial and temporal resolution makes ^{10}Be ideal for measuring long-term average rates of landscape change (Von Blanckenburg & Willenbring, 2014).

^{10}Be is produced by an incessant flux of highly charged atomic particles radiating from the cosmos (Dunai & Lifton, 2014). The energy level of these cosmic rays exceeds the typical binding

energies of atomic nuclei (Eidelman & Group, 2004). These charged particles smash into elements found within Earth's surface and atmosphere and induce the nuclei to spall or eject protons and neutrons (Gosse & Phillips, 2001). ^{10}Be is most frequently generated by spallation of ^{16}O, which is abundant in the atmosphere and in minerals. There are two primary production pathways for ^{10}Be (Figure 3) (von Blanckenburg & Willenbring, 2014). *Meteoric* ^{10}Be is produced in the atmosphere and transmitted to Earth's surface in precipitation or dry fallout. *In situ* ^{10}Be is produced by spallation of elements in the crystal structures of minerals. Both varieties are useful tracers of Earth surface processes, but the applications they are best suited for vary due to differences in environmental abundance and chemical behaviour.

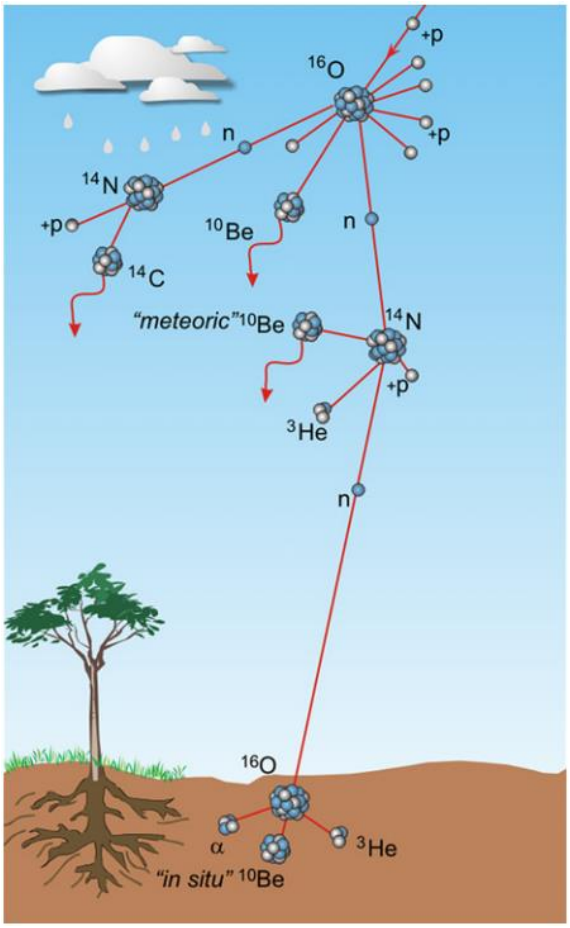

Figure 3 - Schematic of ^{10}Be production by cosmic rays, composed primarily of charged protons (+p). Collision of the charged particles with target nuclei (e.g. ^{16}O and ^{14}N) cause a shower of secondary particles, mostly neutrons (n). These reactions produce cosmogenic radionuclides (e.g. ^{10}Be and ^{3}He) in the atmosphere and upper few meters of Earth's surface. Image from (von Blanckenburg & Willenbring, 2014)

The production of meteoric ^{10}Be occurs approximately 10^3 times faster than in geologic materials (Dunai, 2010). Concentrations of meteoric ^{10}Be at the surface of Earth far exceed *in situ* concentrations, which allows measurements to be made using lesser volumes of sample material (Willenbring & von Blanckenburg, 2010). Beryllium has a high binding energy, causing meteoric ^{10}Be nuclides to adhere tightly to particles in the near surface (Boschi & Willenbring, 2016). A discussion of the particle affinity and sorption capacity of meteoric ^{10}Be can be found in chapter three, section 5.1. Meteoric ^{10}Be associates with many mineralogies and grain sizes, and therefore can be used as a tracer in quartz-poor lithologies, suspended sediments, and fine-grained

lithologies where in situ ^{10}Be cannot (Willenbring & von Blanckenburg, 2010). Challenges may arise in determining accurate concentration values if ^{10}Be has disassociated from particle surfaces (Boschi & Willenbring, 2016). Constraining the site-specific nuclide flux is also more complicated for meteoric than in situ ^{10}Be, because the delivery can be moderated by short-term atmospheric processes (Graly, Bierman, Reusser, & Pavich, 2010; Heikkilä, Beer, Abreu, & Steinhilber, 2013).

Quartz is the most widely applied target mineral for *in situ* ^{10}Be studies because it is abundant in most geologic settings, contains little to no natural ^{9}Be, and has a well-constrained ^{10}Be production rate (Dunai, 2010). Accurate measurements of in situ concentrations require chemical processing to remove meteoric ^{10}Be nuclides attached to the mineral surface (Kohl & Nishiizumi, 1992). The production of in situ ^{10}Be is greatest at Earth's surface and decreases exponentially due to the attenuation of cosmic energy as it passes through Earth materials (Lal, 1991). Attenuation is faster in denser material, and therefore the concentration of in situ ^{10}Be records mass lost through the combination of physical and chemical erosion, the sum of which is called denudation. The average attenuation length of cosmic energy is ~165 cm^2 (Gosse & Phillips, 2001). Below this depth ^{10}Be is effectively not produced by spallation. In settings where the chemical erosion front exists deeper than ~2 m ^{10}Be concentrations record only mass lost by physical erosion (Dixon, Heimsath, Kaste, & Amundson, 2009). This is the case for sediments in the Luquillo Mountains. Deeper than 2 m, ^{10}Be is produced by muon capture but in much lower quantities (Dunai, 2010; Dunai & Lifton, 2014). A practical discussion of the methods for calculating in situ ^{10}Be production and presentation of the relevant equations can be found in chapter four section 2.2.

By employing different sampling strategies, ^{10}Be concentrations can be used to investigate process rates at multiple scales. ^{10}Be measured from a single sample on Earth's surface records a

local erosion or denudation rate (Balco, Stone, Lifton, & Dunai, 2008). ^{10}Be measured in the material actively transported in a river channel derives an average erosion rate integrating the range of surficial erosion upstream of the sampling point in the watershed (Brown, Stallard, Larsen, Raisbeck, & Yiou, 1995; Jungers et al., 2009; Bierman & Nichols, 2004). Soil production rates can be calculated from the concentration of ^{10}Be in samples collected at the base of the soil mantle in settings where the thickness of the soil profile has remained constant over the timeframe of ^{10}Be accumulation (Heimsath, Dietrichs, Nishiizuml, & Finkel, 1997). Each one of these sampling strategies is applied to answer the research questions in this thesis.

2. RESEARCH FOCUS

The aim of this thesis is to address significant knowledge gaps in our understanding of the feedbacks between the geomorphic evolution of landscapes in response to external perturbation and critical zone processes. To this end, we examined the behaviour of three critical zone systems in the geomorphically evolving landscapes of the Luquillo Mountains, in Puerto Rico. These systems are mechanistically linked to aspects of the external environment, which are referred to as boundary conditions. Changes in boundary conditions perturb the functioning of the critical zone systems in complex ways that have not been well quantified. Here, we seek to quantify and explain responses in the water, ecosystem, and soil of the Luquillo Mountains to perturbations in the two most powerful and deterministic boundary conditions: climate and tectonics.

3. RESEARCH SIGNIFICANCE

As the name suggests, critical zone processes are crucial to maintaining a habitable Earth. Soil, water, and ecosystems directly impact human health, climate, and global biogeochemical cycles. Locally, issues of drought and sedimentation have had devastating impacts on communities

living near the Luquillo Mountains. Globally, the stability of agriculture and ecosystems hangs in the balance between the erosion of soil and its continued rejuvenation from bedrock (Montgomery, 2007). Establishing an accurate model framework for the interdependence of these Earth systems is prerequisite to mitigating and adapting to anthropogenic climate change. As specific contributions to this goal, the research in this thesis advances our understanding of the adaptive capacity of the rainforest ecosystem to climate change and disturbance. Our work finds that a previously unidentified structural control exists on the groundwater hydrology in the Luquillo Mountains. We also demonstrate that a longstanding paradigm in Earth Science is flawed. This paradigm suggests that a mechanistic link between the depth of soil and the rate of soil production exists globally, such that internal feedbacks will accelerate soil production under very thin soils and maintain the presence of a soil mantle. Here, we find that the evidence supporting this claim is methodologically flawed and that the global data instead suggest no dependence exists between soil production and soil depth. This has dramatic implications for soil sustainability in the context of anthropogenically accelerated soil erosion.

4. STATEMENT ON CONTENT AND ORGANIZATION

This thesis contains three research chapters, all of which have been submitted to academic journals for publication. The text and structure of each submission is preserved in the chapters. As such, the style of writing and formatting of the research chapters reflects the guidelines of the target journal. For consistency, in the introduction and conclusion chapters descriptions of the research design, objectives, conclusions, recommendations, and contributions to knowledge are presented separately for each of the research chapters.

5. RESEARCH OBJECTIVES AND DESIGN

5.1. Water

The objective of chapter two is to assess the role that groundwater plays in the geomorphology and hydrology of the fluvial network in the Rio Blanco. As demonstrated by the studies of Brocard (2015, 2016) and Pike et al. (2010), the structure of the Rio Blanco fluvial network indicates that it is responding to different boundary conditions upstream vs downstream of a tectonically-triggered erosion front. We endeavour to identify the impacts of this on the interaction between groundwater and the surface water network. Our hypothesis is that a persistent, near-surface groundwater table sets a local baselevel in the relict topography of the Rio Blanco - and that this water table can induce channel incision in the fluvial network. In contrast, downstream of the erosion front the groundwater table is not a boundary condition for fluvial incision, and sapping is impeded by the emergence of corestones at spring sites.

Our research design takes as a theoretical framework the work of Lamb et al. (2006) describing the conditions under which sapping erosion can drive fluvial incision into a ridge network. A first-order condition is that the velocity of discharge must be great enough to transport sediment from the seep face for channel incision to proceed (Dietrich & Dunne, 1993; Dunne, 1990). We directly measured the baseflow discharge at a population of small, seep-fed headwater channels in the Rio Blanco. We estimated an average baseflow discharge for other channels using a linear model relating the measured baseflow rate to the channel's contributing drainage area, estimated with GIS. We improved the predictive capacity of the model by including baseflow measurements for a series of differently sized sub-catchments within the watershed and normalizing the discharge values to the annual average precipitation in each catchment (Murphy et al. 2017). We improved the robustness of the linear fit to the data through bootstrapping. This

model results in a prediction for the average baseflow velocity at any point in the Rio Blanco watershed from the contributing drainage area.

Through field surveys, we categorized spring sites as either emerging from beneath piles of corestones or emerging visibly from the hillslope adjacent to the channel. We draw this distinction because large corestones are clearly beyond the transport capacity of baseflow velocities. At the other spring sites, we sampled the bedload moving under baseflow discharge, measured its grain size distribution and calculated the critical shear stress required to mobilize the sediment (Shields, 1936; Weiner & Yu, 1987). From these measurements, we determined which spring sites in the Rio Blanco fluvial network are capable of incising through sapping erosion based on their physical properties. Our results show that groundwater discharge can induce erosion through sapping and excavate sediment in channels where corestones are not in the channel. The erosion front in the Rio Blanco delineates the presence/absence of sapping channels, suggesting that this mechanism depends on the geomorphic evolution of the deep critical zone (Comas, Wright, Hynek, Fletcher, & Brantley, 2018; Orlando, Comas, Hynek, Buss, & Brantley, 2016).

We measured the ^{10}Be-derived long-term erosion rate for five channels where sapping is a likely mechanism for incision to determine if sapping generates relief by increasing erosion in river channels relative to the ridgelines. For some sites, channel erosion rates are higher than erosion rates measured for ridgeline soils and the greater catchment area (Brocard et al. 2015, Brown et al. 1995). At other locations, channel erosion is practically identical to the surrounding environment. An important advance is made in this work by comparing channel incision rates from ^{10}Be to baseflow discharge rates for the landscape. Using this approach, we find that the incision rate of sapping channels relates linearly to discharge – a different behavioural model than the stream power model used to describe fluvial networks (Whipple & Tucker, 1999).

5.2. **Ecosystems and erosion**

The objective of chapter three is to evaluate the sensitivity of the ecosystem and physical erosion rates in the Rio Fajardo watershed to perturbations over the Holocene and late-Pleistocene. In this chapter, we present a new archival record of terrestrial processes from a stratigraphic section of stacked paleosols the Rio Fajardo floodplain exposed by cut bank incision. We constrained the chronology of the sediments from the radiocarbon ages of organic deposits. The entire stratigraphic sequence spans 26 ky to the present, capturing major shifts in the Caribbean climate (Haug et al., 2011), the intensification of the El Nino-Southern Oscillation (Donnelly & Woodruff, 2007), and the arrival of humans on the island (Burney, Burney, & MacPhee, 1994). In this chapter, we contextualize the dataset with a literature review of the paleo-climate records for the Caribbean and studies documenting anthropogenic land cover change in north-eastern Puerto Rico (Scatena, 1989). We analyse this literature to evaluate the potential of perturbations to drive the environmental changes we documented in the floodplain sedimentary record.

We constructed a record of the ecosystem composition using measurements of the stable carbon isotopic ratio of organic material (Smith & Epstein, 1971). To interpret changes in this ratio, we compared our measurements to the isotopic ratios of carbon transported in the modern river and to that of plants, litter, and soils, which may act as carbon sources. We also considered the effects of decomposition prior to transport or diagenetically on trends in the record (Marin-Spiotta, Silver, Swanston, & Ostertag, 2009). Using basic statistical methods, we determined when apparent changes in the isotopic record exceeded the magnitude of variability in the natural system, and thus indicated dynamic competition between C_3 and C_4 photosynthesizing plant groups. Through comparisons to the paleo-climate and land use records, we identified the most important

drivers of ecosystem change and evaluate whether the rate and style of response differed depending on the agent of change.

We derived a record of the paleo-erosion rates in the catchment from the concentration of meteoric ^{10}Be in layers of the floodplain sediments. Meteoric ^{10}Be has been used as a paleo-erosion tracer in marine and lake sediments (Marshall et al., 2015; Willenbring & Von Blanckenburg, 2010), but this work is the first application in a floodplain. Therefore, we included an additional dataset aimed at assessing the reliability of meteoric ^{10}Be as an erosion tracer for this context. We measured meteoric ^{10}Be concentrations in surface soils and at the base of a landslide scar to determine whether ^{10}Be is leached out of the surface soils after deposition. We also measured the ^{10}Be concentration in the suspended sediment at flood stage and compared it to the ^{10}Be concentration at the surface in the floodplain to test if deposition affected the inferred erosion record. ^{10}Be may absorb more tightly to certain size fractions and mineralogies (Boschi and Willenbring, 2016), therefore we compared ^{10}Be concentrations in the stratigraphy to the sediment size distribution, Fe-oxide and clay mineral abundances, and geochemical properties derived from elemental composition. Furthermore, we added an error calculation to account for the fallout of ^{10}Be on the surface of the floodplain based on the aggradation rate of the floodplain sediments. As a result, this record is also a methodological development for the application of meteoric ^{10}Be in the Earth Sciences.

We generated the conclusions of this chapter by examining trends in both records for distinct timeframes. Our analysis is enhanced by the ability to compare shifts in ecology and physical erosion side-by-side, because these environmental processes are responsive to similar external perturbations and may cause feedbacks in each other. Overall, erosion rates track likely precipitation trends but remain stable within timeframes. This indicates a sensitivity to climate

change over all, but not to short-term excursions in global temperature. The composition of the ecosystem reveals competition between tropical grasses and primary forest vegetation that is better explained by temperature trends than by precipitation. Both systems change gradually in an apparent dynamic equilibrium with climate from the start of the record until approximately 5 ky before present. At that time the variability and magnitude of change increases significantly in both records. This shift is coincident with an intensification in the frequency and magnitude of tropical storms in the Caribbean (Donnelly & Woodruff, 2007; Woodruff et al. 2008).

We conducted a detailed review of the impacts of Hurricane Hugo on the forest and erosive processes in the Rio Fajardo and analysed the effect such an event would have on the two proxy records. From this work, we found that the ecological dynamics and physical erosion processes in the watershed shifted to a state of pulsed-response to storm-driven disturbance. From 5 ky to the present, these climate-coupled critical zone systems are characterized by disturbance ecology and landslide-dominance. Finally, the greatest documented anomaly in both records occurs coincident with the colonization of Puerto Rico and large-scale anthropogenic land cover change in the watershed. Over the timeframe of this record, human impacts can drive changes significantly exceeding the rate and magnitude of natural disturbance.

5.3. **Soils**

In chapter four, we designed a mixed methods approach to quantify soil production rates in the relict and adjusting portions of the Rio Blanco watershed. We collected a dataset of soil production rates in the relict topography following standard methods (Dixon & Riebe, 2014; Heimsath et al., 1997). This dataset did not conform to the theoretical predictions of the soil production function. The soil production function is a widely accepted paradigm in Earth Science positing that the rate of soil production from saprolite (or bedrock in the absence of saprolite) is

mechanistically linked to the thickness of the overlaying soil mantle. The exact mechanisms of this association are not specified, rather a range of top-down acting pedogenic processes may be invoked, tailored to the study location. This very logical prediction was made first by Gilbert, (1877) in a seminal text that is widely considered to originate the discipline of geomorphology. Two mathematical functions predicting the relationship between soil thickness and soil production rate were developed by Carson & Kirkby (1972) (Figure 4). A "humped" or "exponential" soil production function has been the subject of much debate and research in the intervening years (Humphreys & Wilkinson, 2007) – motivated by the consequences of erosion outstripping soil production in an irreversible way (Dietrich, Hsu, & Montgomery, 1995; Montgomery, 2007). The first empirical dataset of soil production rates was introduced by Heimsath et al. (1997) whose results supported the exponential dependence of soil production upon soil depth. This study outlined a methodological approach for measuring soil production rates. Since this advance, the term *soil production function* now popularly refers to the best fit equation given by a least squares regression measurements for an entire study area.

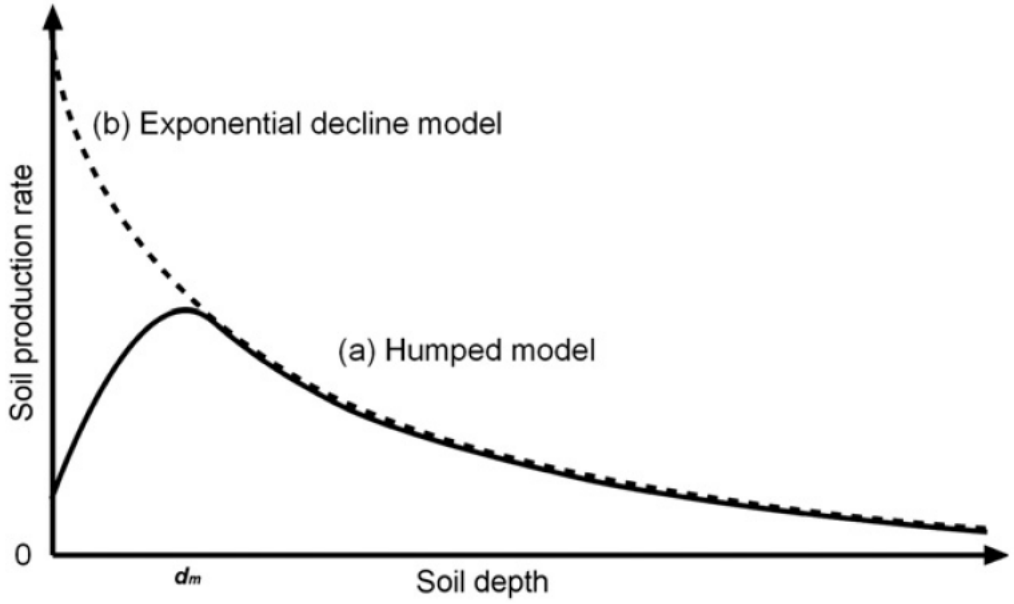

Figure 4 - An illustration of the conceptual framework for the soil production function. The exponential form predicts a maximum soil production rate is achieved when the soil cover is absent (Carson & Kirkby, 1972; Heimsath et al., 1997). The humped version predicts a maximum soil production rate under some critical soil mantle thickness (d_m) (Gilbert, 1877). Both models predict the self-arrest of soil producing processes under a thickening soil mantle. Image from Humphreys and Wilkinson (2007)

The Heimsath et al (1997) method has been used to generate datasets of soil production rates at a global scale. Many of the datasets that exist today, ours included, do not conform to the prediction of a negative exponential relationship between soil depth and soil production rate. We first endeavoured to explain the split by testing the hypothesis that the non-conforming sites are places where pedogenic processes work from the bottom-up, i.e. that soil production is a rate of "thickening" driven by the deposition of decomposing plant litter and dust on the surface. Reviewing the relevant site-specific factors, we found that the non-conforming sites are not united by a common thread of soil forming factors, aridity, plant decomposition rate, ecosystem composition, leaf area index, intensity of biotic disturbance, or dust deposition (see Appendix). We noticed instead that several of the other studies were also conducted in relict topography, perhaps suggesting the position of the base level may be related to the rate of soil production.

However, from the existing publications it is not clear whether the position of the water table, hillslope gradient, or the degree of weathering in the soil or saprolite can be invoked as clear controls on the variation in soil production rates globally.

Our breakthrough came from flipping the problem. What if the non-conforming datasets are accurate and the conforming datasets are not? In the non-conforming datasets, soil production rates vary randomly around a local mean rate. If this were accurate, then the dependence of soil production rates on soil depth was more likely a methodological artefact. We designed a simple numerical simulation of a hillslope profile covered by a soil mantle in steady-state. We populated the soil mantle with ^{10}Be nuclides assuming arbitrary, constant values for external erosion rate, production of ^{10}Be at the surface, and material bulk density. We fixed the position of the soil-saprolite boundary in space and held the concentration of ^{10}Be nuclides at the interface constant for the rest of the simulation. Then, we modelled two different erosion scenarios. First, we simulated a spatially constant loss of material from the surface, resulting in a new depth to saprolite that is equal at every point along the hillslope. Second, we simulated spatially variant loss of material from the surface, generating different depths to saprolite along the hillslope profile.

The remaining steps in the simulation follow the procedure that a researcher would use to conduct a field study. At a series of points along the hillslope profile the model records the post-erosional depth to saprolite, as a researcher would record the depth of their soil pit. The model calculates the rate of ^{10}Be production at the soil-saprolite interface using the apparent soil depth as an input parameter. This derivation decreases ^{10}Be production rates exponentially as a function of the product of the soil depth and soil density terms. This depth-specific ^{10}Be production rate is used to back calculate the time required to accumulate the measured concentration of ^{10}Be and derive the apparent soil production rate. A soil production function is fit to the depth and soil

production rate data for point along the model hillslope using least squares regression. In the constant erosion scenario, soil production rates are independent of soil depth. In the spatially varying erosion scenario, soil production rates decline exponentially with soil depth.

In a subsequent version we added random noise to the ^{10}Be concentration at the soil-saprolite interface. The noise was generated by a random number simulator having a normal distribution around a mean of zero with a standard deviation equal to 25% of the steady-state ^{10}Be concentration with no erosion. For these simulations, the spatially constant erosion scenario produced the same result as the non-conforming datasets from real-world studies: soil production varied randomly around a mean value. The spatially variant erosion scenario continued to derive soil production functions with exponent values in the range of the studies finding an exponential decline in soil production rates with increasing soil thickness.

We experimented with the model outputs by varying the input parameters: surface production rate, soil bulk density, and external erosion rate. Increasing the soil bulk density term results in higher exponent values in the soil production function. Increasing the external erosion rate raises the value of the coefficient in the equation. Varying the surface production rate influences the apparent soil production rate but not the parameters of the soil production function. This led us to conclude that the parameters derived by the regression fit are related to the energy attenuating properties of the overburden substrate and the environmental context. They are not related, as has often been interpreted, to the coupling between soil depth and soil production for a given landscape.

The Heimsath et al. (1997) method assumes steady-state soil thickness over the time span of ^{10}Be accumulation in the subsurface. Both of our erosion simulations violate that assumption

and would lead to the calculation of erroneous soil production rates. The effects of inconsistent soil cover on ^{10}Be concentrations over time has been considered by other authors and the uncertainty introduced by pulsed or stochastic erosion has been modelled (Heimsath, 2006). This simulation is a novel test of the impact of surface lowering rates that vary in space across a landscape and are decoupled from the propagation of the soil-saprolite interface. In fact, material transport laws predict that surface lowering rates will vary in space as a function of the local topographic curvature (Roering et al., 1999).

Returning to the global dataset of soil production rates, we find that the difference between the population of sites that do versus those that do not conform to the paradigm is best explained by their connection to a locally incising baselevel. Strong soil production functions emerge in actively uplifting mountain ranges and in topography with strongly convex curvature approaching the angle of material repose. Weak or non-existent soil production functions characterize relict topography, parabolic hillslopes, and plateaus. We conclude from this analysis that evidence supporting the exponential soil production function is a computational artefact of exponentially declining ^{10}Be production in landscapes where surface lowering varies across space. In sites where surface lowering is likely constant across space, there is no global dependence of soil production on soil depth.

GLOSSARY OF TERMS

- **Fluvial:** sub-aerial, channelized water system
- **Critical zone architecture:** Rock and soil substrate of the critical zone
- **Soil:** Decomposed rock that retains no appearance of the mineral fabric of the parent material
- **Saprolite:** Soft, decomposed rock that retains the appearance of the mineral fabric of the intact rock.
- **Seepage:** Sub-aerial emergence points of subsurface water
- **Sapping:** Process of erosion by headwall collapse above a groundwater seep
- **Corestones:** Spheroidal weathering products characteristically produced in granitoid bedrock
- **Equilibrium:** Equal rates of oppositional geomorphic processes over space and time
- **Disequilibrium:** Rate exceedance of opposing geomorphic processes over another
- **Dynamic equilibrium:** State of balance between ongoing processes
- **Steady-state:** Constant rate over space and time
- **Transient:** Change in rate over space or time
- **Baselevel:** Low point beyond which no erosion occurs
- **Runoff:** Overland discharge of water
- **Weathering:** Chemical reactions that break-down geologic material
- **Erosion:** Physical displacement of material under gravity
- **Denudation:** Combined loss of mass due to chemical and physical erosion
- **Knickpoint:** A sharp break in gradient along the longitudinal profile of a fluvial channel

CHAPTER 2

DYNAMIC CRITICAL ZONE ARCHITECTURE DRIVEN BY SUBSURFACE FLOW IN THE LUQUILLO MOUNTAINS, PUERTO RICO

Emma J. Harrison[1] • Gilles Y. Brocard[2] • Nicole M. Gasparini[3] • Nathan J. Lyons[3] • Jane K. Willenbring[1]

[1] Scripps Institution of Oceanography, University of California San Diego, La Jolla, CA, USA.

[2] Institut des Sciences de la Terre, Observatoire des Sciences de l'Univers, University of Grenoble, France

[3] Department of Earth and Environmental Sciences, Tulane University, New Orleans, LA, USA.

ABSTRACT

Subsurface flow can affect Critical Zone processes and shape landscapes. In this study, we examine the emergence and behaviour of water stored in the subsurface across a watershed that is divided into a patchwork of domains eroding at different rates. Our field surveys reveal a sharp divide in the presence of springs. Springs are common in the relict upland landscape and are frequently associated with amphitheatre-shaped erosional features and waters that coalesce into tributary streams. We measure the geometric properties of the upland valleys and baseflow discharge of these seep-fed stream to construct a model relating drainage area to local baseflow discharge rates. We document erosion in the seep-fed channels using a bedload sampler and long-term erosion rates from cosmogenic ^{10}Be. We find a linear correlation between baseflow discharge and long-term incision for individual seep-fed channels, suggesting a role for groundwater erosion (i.e. sapping) in landscape evolution within the relict topography of the watershed. In the adjusting

topography, indications from stream chemistry and geomorphic structures suggest a predominance of runoff over groundwater discharge in hillslope erosion and in delivery of water to the stream channel.

1. INTRODUCTION

Subsurface critical zone architecture is a strong control on the volume, spatial distribution and residence time of groundwater. In humid regions, groundwater storage is moderated primarily by the depth of weathering that creates porosity and the fracture density in the bedrock substrate (Rempe and Dietrich, 2018). In turn, the recharge of subsurface reservoirs with oxidized water delivered by precipitation drives the chemical weathering reactions that disaggregate bedrock and produce regolith and soils. The nature of this relationship is dynamic in places where the topography is rejuvenated by a pulse of past uplift. Changes in the boundary conditions that parameterize landscape form, such as the relative position of sea level, initiate waves of progressive adjustment in the gradient of river channels and hillslopes (Crosby & Whipple, 2006; Hilley & Arrowsmith, 2008). Recent investigations demonstrate that the adjustment of surface topography to new boundary conditions after rock uplift is linked to the depth of weathering in the subsurface on the timescales of landscape evolution (Comas et al., 2018). This coupling implies that a dynamic relationship could link the evolution of surface topography, the subsurface storage of water, and the ways in which that water is delivered to stream conduits. In this investigation, we aim to 1) characterize the impact of subsurface water on the long-term denudation and geomorphology of the Rio Blanco watershed and 2) investigate the impact of tectonically-induced landscape evolution on the subsurface storage of water and the entry of that water into the surface stream network.

The Luquillo Experimental Forest in eastern Puerto Rico is a well-constrained setting to study the impact of landscape evolution on groundwater storage, flow paths, and residence time. A tectonically-triggered wave of erosion is propagating up the Rio Blanco watershed, dividing the landscape into a patchwork of domains eroding at different rates (Brocard et al., 2016, 2015). Slowly eroding parts of the watershed are underlain by deep profiles of weathered saprolite (Buss, Sak, Webb, & Brantley, 2008), which store a groundwater reservoir perched in the headwaters of the Luquillo Mountains. The Rio Blanco sustains a high baseflow discharge due to groundwater inputs from springs and diffuse, hyporheic fluxes (Chestnut & McDowell, 2006; Shanley, McDowell, & Stallard, 2011). In the last decade, Puerto Rico has experienced a series of severe droughts that mimic future, predicted climate change scenarios for the region project that include heightened variability in precipitation (Miller, Mote, & Ramseyer, 2019; Ramseyer, Miller, & Mote, 2019). The stable base flow level of this river system, which supports a large population centre, exists in part because of positive feedbacks between the fluctuating groundwater table and the production of porosity (by chemical erosion) for water in the subsurface.

The evolution of critical zone architecture coupled to the trajectory of knickpoints alters the feedbacks between subsurface water and regolith. Solutes derived from chemical weathering appear to double away from the rapidly eroding knickzone (Bhatt & McDowell, 2007). Upstream of the knickzone, the Rio Blanco consists of small channels fed by groundwater springs – which are rare in the adjusting topography downstream of the knickpoint lips. In this work, we infer spatial information about the aquifer feeding the Rio Blanco by mapping the springs. We posit that the springs emerge where the aquifer surface intersects the topographic surface. We attempt to understand whether groundwater seepage plays a role in physical erosion within the watershed by studying a population of channels with seeps at their source points. In these channels, we made

measurements of the baseflow discharge rate, measured the grain size distribution of the bedload material mobilized under baseflow, and calculated channel denudation rates from cosmogenic ^{10}Be concentrations of the detrital material. We also made measurements of the channels' geometric properties including the dimensions of the channel tips, the width and the depth of channel banks, in an attempt to elucidate whether seepage is important in shaping the channel form.

1.1. **Field Setting**

The Luquillo Experimental Forest is located in the Luquillo Mountains in north-eastern Puerto Rico. The highest mountain peaks reach ~1,050 m and represent the first topographic barrier encountered by the Westerly trade winds (Scatena & Larsen, 1991). Consequently, orographic forcing makes this area the wettest region in Puerto Rico with mean annual precipitation ranging from 2,500 mm yr^{-1} at the coast to 4,500 mm yr^{-1} at the peaks (Figure 5), (García-Martinó, Warner, Scatena, & Civco, 1996; Murphy, Stallard, Scholl, González, & Torres-Sánchez, 2017). Hurricanes and tropical storms are important, but the majority of precipitation is delivered in low-intensity rainfall (Brown et al. 1983). The mountains host a tropical rainforest biome that is compositionally zoned by elevation and by topography (Brown et al. 1983; Wolf et al. 2016). The mountains are drained by several large river systems. This study is conducted in the Rio Blanco watershed, which drains the southern flank of the mountains into the Caribbean Sea. The Rio Blanco incises principally into a quartz diorite bedrock, which is compositionally homogenous at length scales of 10^1-10^3 m (inclusions exist at smaller scales) and is rich in quartz (~23%) (Smith, Schellekens, & Diaz, 1998). This quartz diorite weathers along fracture planes into spheroidal core stones (Buss et al., 2013, 2008). Core stones are bounded by concentric rindlets where the weathering of plagioclase, hornblende and the initiation of biotite weathering occurs (Fletcher, Buss, & Brantley, 2006; Turner, Stallard, & Brantley, 2003).

Rapid uplift of the Caribbean plate initiated approximately four million years ago, bringing the island of Puerto Rico to its present-day elevation (Brocard et al. 2016). Tectonic uplift - or baselevel fall - triggers progressive waves of erosion upstream through river networks and, eventually, to hillslopes (Crosby and Whipple 2006; Grieve, Mudd, and Hurst 2016; Hilley and Arrowsmith 2008; Reinhardt et al. 2007; Whipple and Tucker 2002). In a landscape that is still adjusting to rock uplift, knickpoints migrating upstream often separate slowly eroding "relict" topography from rapidly eroding, steep topography that is adjusting to a new baselevel (Whipple, DiBiase, and Crosby 2013; Willenbring et al. 2013). An erosive wave traveling up the Rio Blanco watershed, generates sharp knickpoints that separate the landscape into a patchwork of domains eroding at various rates (Brocard et al., 2016, 2015). "Relict" and "adjusting" topographic zones have distinct differences in hillslope morphology (Hurst et al., 2013), available soil nutrients and chemistry (Porder et al. 2015; Brocard et al. 2015), river channel morphology (Brocard et al., 2016) and forest structure (Wolf et al., 2016).

Within the Rio Blanco watershed, the Rio Icacos is the largest tributary stream. It is outfitted with a USGS gaging station (Figure 5) slightly upstream of the knickpoint transition between relict and adjusting topographic zones. Rio Icacos above this USGS gage is a long-studied site in the Luquillo Experimental Forest (LEF) where hydrological and hillslope processes have been thoroughly characterized. In this section of the watershed, which is entirely within the relict topographic region, the ridgetops are believed to be eroding and producing soil in sync with each other (Brown et al. 1995; Chabaux et al. 2013; Turner, Stallard, and Brantley 2003). Hillslopes – especially hillslopes affected by mass wasting – river sediment, and solutes record erosion rates that are significantly faster than the ridgetops (Brown et al. 1995; Stallard 2012). Hillslope erosion

exceeding ridgetop erosion in the relict domain indicates relief is growing even above knickpoints where the river gradient is disconnected from the modern Rio Blanco baselevel position.

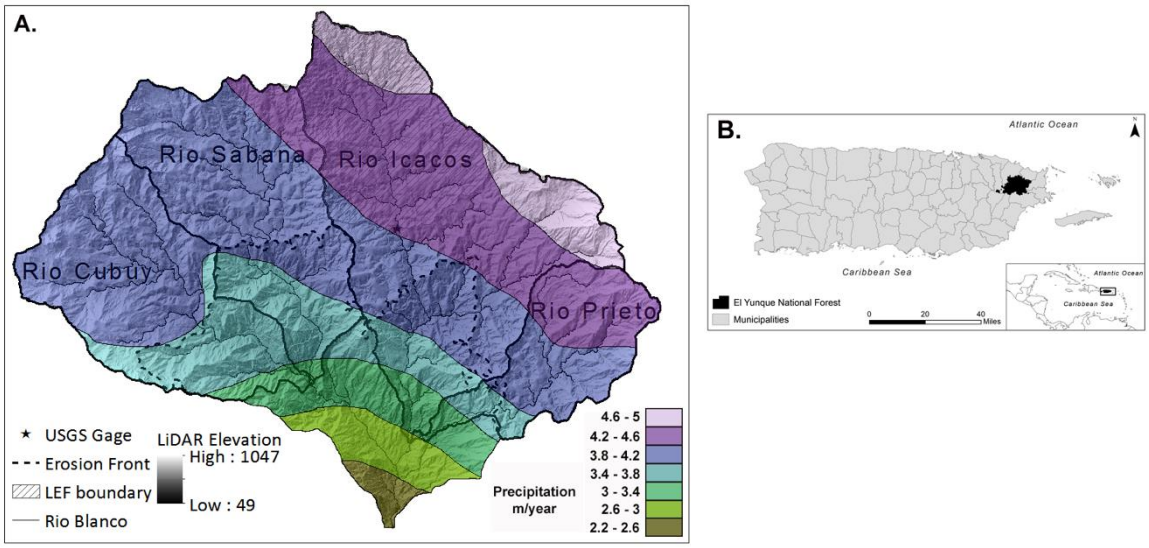

Figure 5 – A: Rio Blanco watershed with four major tributary rivers labelled. Dashed line indicates the location of the erosion front traveling through the watershed. Dashed line crosses each river at the knickpoint lip separating the relict and adjusting portions of the topography. The boundary of the Luquillo Experimental Forest watershed (LEF) indicated by the patterned lines and the location of USGS gage 50075000 is marked by the star symbol. Precipitation gradient from Murphy et al. (2017). B: Map of Puerto Rico showing the location of the El Yunque Mountains, where the LEF is located. Inset showing the position of Puerto Rico in the Caribbean region. Reproduced from Wood et al. (2019).

1.2. **Site Hydrology**

The chemical behaviour of the river water during and between storm events enhances our understanding of the routing and residence time of water in the subsurface. Long-term monitoring of stream chemistry (Shanley et al., 2011) and hydrograph separation of storm events (Scholl et al., 2015) delineate the chemical fingerprint of groundwater contribution to the stream. Groundwater chemistry is characterized by solutes derived from weathering products, principally Si, Ca, Na, Mg and alkalinity (Bhatt & McDowell, 2007; Shanley et al., 2011). These studies find a large, sustained groundwater contribution to the river levels. Except during intense storm events, approximately 75% of the discharge is groundwater fed (Chestnut & McDowell, 2006; Scholl et

al., 2015; Shanley et al., 2011). During large storm events stream chemistry is diluted almost instantaneously (Schellekens et al., 2004; Shanley et al., 2011) and returns to the pre-event composition quickly (Scholl et al., 2015). This behaviour is characteristic of a system where water is routed to the streams via overland flow or runoff, however, in a four-year-long study by Larsen, et al. (1999) monthly surface runoff equalled only 0.2-0.5% of monthly precipitation. Although difficult to document beyond qualitative observations, we speculate that the subsurface hydrology is influenced by the presence of pipes and macro porosity. These conduits are probably created by open tunnels left by decaying roots and burrowing earthworms (González et al., 2007) in the upper ~130 cm, which is the typical thickness of ridgetop soil profiles sitting on top of the weathered saprolite (Harrison, Brocard, & Willenbring, 2017). In the saprolite, the concentration of flow around the edges of core stones may likewise increase the infiltration rate and capacity beyond the apparent hydraulic conductivity of the material (Harden & Scruggs, 2003; White et al., 1998).

Groundwater enters the stream network via multiple, distinct pathways: hyporheic diffusion through the riparian zone of floodplains (Chestnut & McDowell, 2006), at the source points of the river network (Bhatt & McDowell, 2007), and in springs emerging from valley flanks and ridgelines. We wish to draw a distinction between populations of fluvial source points, or channel tips, that have different characteristics. At the most common source points, flowing water emerges from underneath piles of large corestones that have exhumed in situ or slid down the sides of ridgelines, or both. In these instances, while groundwater surely feeds the flow of water, it is impossible to assess the relative role of seeping water in the entrainment and transport of sediment. At other sites, amphitheatre-headed depressions form above seeps that feed into sandy-bottomed streams. We hypothesize that in this second population of channel tips, seepage itself - rather than quick flow, overland flow, or mass wasting – may play a dominant role in the erosive processes of

channel entrenchment and slope back wearing. Seepage erosion, if it indeed occurs, is a major driver of landscape change only in the relict portion of the topography. Based on our observations, the presence/absence of springs emerging from ridgelines and at the tips of sandy channels is delineated in space at the boundary of the erosion front. In the adjusting portion of the topography, to the best of our knowledge, all channel source points are choked with piled corestones.

Figure 6 – A: Image of the channel headwall and unchannelized flow from the seep. B: Seep waters are red when they emerge from the hillslope. The red colouring is indicative of oxidization of the dissolved iron when the water becomes oxygenated at the ground surface. C: Seep waters have channelized with well-defined banks.

2. METHODS

2.1. Field campaigns and digital terrain analysis

We located potential springs on a 1m resolution LiDAR DEM as depressions in ridgelines near river banks. We verified their locations through field campaigns and used their positions to determine a flow accumulation threshold for digital mapping. For the subset of seeps associated with incised channels, we made measurements of the channel geometries using the 1m DEM. For this process, we traced longitudinal profiles from the crest of the headwall to the point of the tributary's junction with the larger river network. We identified the first slope break in the profile

as the emergence point of the seep. We verified the start of channelized flow using cross-sectional profiles drawn in succession along the longitudinal profile. We fitted the tip of the incision with a circle whose diameter is equal to the width of the channel head (Dietrich and Dunne 1993). The radius of this circle and the bankfull width of the incised channel above where it joins the main stem were used to calculate the channel aspect ratios (Petroff et al., 2011) (Figure 7). At a subset of channels, we verified the dimensional measurements in the field with a laser range finder.

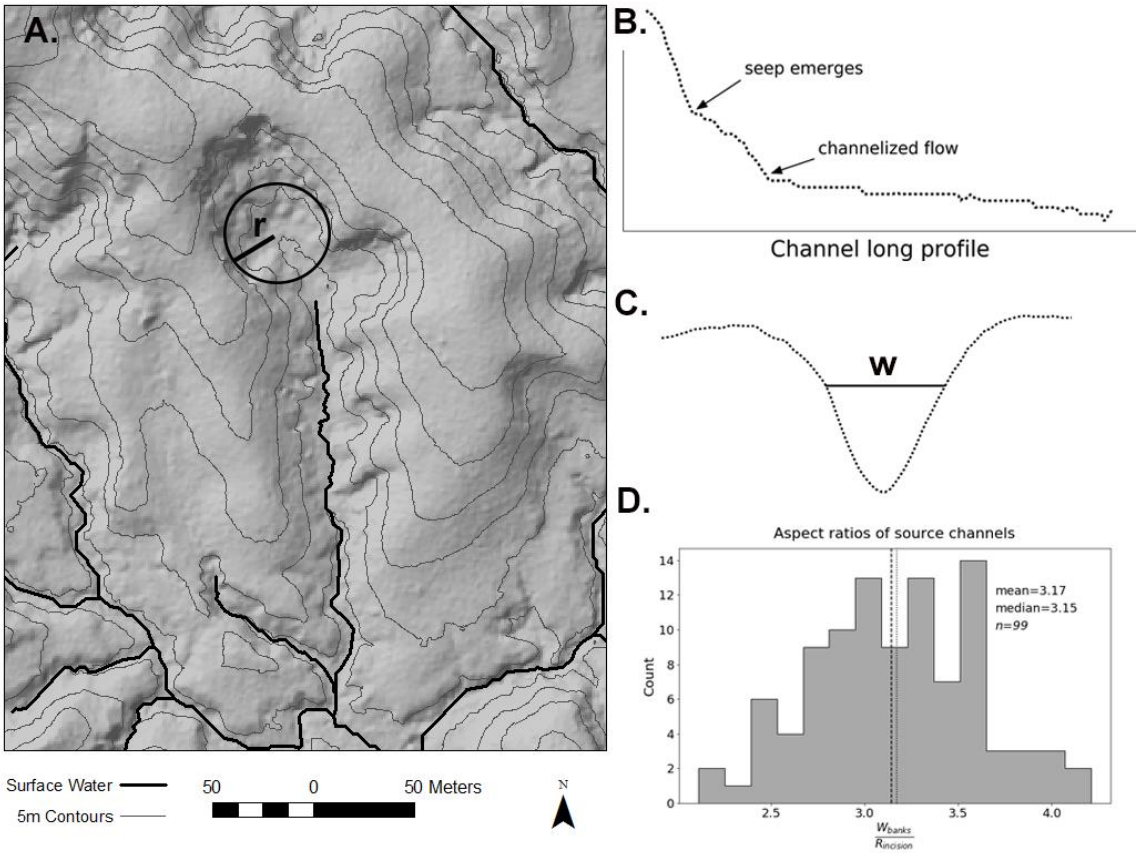

Figure 7 – A: Shaded contour map of a seep-fed channel in Rio Icacos where baseflow discharge and long-term erosion rates were measured. Circle fitted to the channel head is used to determine the radius term in the measured channel aspect ratio. B: Long profile of the channel pictured in 3A showing the location of the seep emergence (used to fit the circle) and the location where the flow becomes channelized. C: A cross-sectional profile of the channel, demonstrating measurement of the channel width term in aspect ratio measurements. D: Histogram with the results of the aspect ratio measurements for 99 seep-fed channels forming beneath amphitheatre-shaped erosional features in ridgelines. Average measurement for the dataset is 3.17 and the median value is 3.15.

2.2. **Baseflow discharge measurements**

Baseflow is the portion of river discharge that comes from groundwater storage (Hall, 1968). Long-term monitoring of Rio Icacos confirms that baseflow forms a significant portion of river discharge outside of storm peaks (Derry, Pett-Ridge, Kurtz, & Troester, 2006; Kurtz, Lugolobi, & Salvucci, 2011; Schellekens, Bruijnzeel, Scatena, Bink, & Holwerda, 2000; Schellekens et al., 2004; Scholl et al., 2015; Shanley et al., 2011). We expect that during low flow conditions, nearly all of the discharge in the small, sandy channels forming at the coalescence of seeps is groundwater. In June of 2016, the Luquillo Mountains had not received high-intensity rainfall for nearly two weeks. We made direct measurements of baseflow discharge for a subset of the seep-formed channels using a salt plug tracer injection (Moore, 2004a, 2004b) and using weirs for an additional group where the channel reaches were too short for the tracer method. As it would be challenging and impractical to measure discharge directly in all of these sites, we measured baseflow discharge in sub-catchments spanning a range of contributing drainage areas (0.003-3.4 km^2, n=11) and used these measured discharge rates to construct a discharge-to-drainage area relationship. We tested several models describing the relationship between drainage area and baseflow discharges and ran each model iteratively on randomly selected subsets of the observed data. Ultimately, we use a linear model averaging one thousand iterated regressions to predict the baseflow discharge at channels where the flow could not be measured directly (Figure 9). Drainage area was measured from a 1m LiDAR DEM and a field-verified flow accumulation threshold in ArcGIS. We adjusted predicted baseflow rates for the four watersheds based on spatial differences in precipitation reported in the rainfall model of Murphy et al. (2017).

2.3. **Bedload grain size analysis**

We deployed a Helley-Smith bedload sampler (Emmett, 1980) in one of the seep-tipped channels in the Rio Sabana watershed. We measured the mobile bedload in this channel because it's baseflow discharge was the median of our field measurements. The sampler was deployed for three hours and fifteen minutes under baseflow conditions, with a discharge of 0.94 L/s. We sieved the sample into size fractions (<0.063, 0.063-0.125, 0.125-0.25, 0.25-0.5, 0.5-2 mm diameter) and calculate the representative fraction of the bulk sample for each fraction. We use the function of the cumulative sum of the size fractions to determine the probabilistic D_{50} of the bedload sample. From this D_{50}, we calculate the critical shear stress for particle motion as:

$$\tau_c = \theta * (s-1)\rho_w g D_{50} \quad (1)$$

where θ is the Shield's parameter, determined from the Shield's diagram, s is the relative particle density ($\rho_s - \rho_w$), ρ_s is the sediment density (2650 kg/m^3), ρ_w is the density of water (1000 kg/m^3) and g is acceleration due to gravity (9.8 m/s^2).

2.4. **^{10}Be derived erosion rates**

We collected in stream sediment samples from the seep-fed tributary channels just above their junction with the river main stem, excluding any channels where we observed the emergence of core stones, rill and gully features, or mass wasting on the hillslopes. We calculated the average erosion rates of the channel catchments from the accumulation of *in situ* ^{10}Be in the sediments (Brown et al. 1995; Granger, Kirchner, and Finkel 1996). ^{10}Be is produced in the mineral lattice of quartz grains in the upper ~2 meters of Earth's surface at a well-constrained rate (Dunai, 2010; Gosse & Phillips, 2001; Lal, 1991). In many settings, ^{10}Be records the total volume of mass lost from chemical and physical erosion (Dixon & Riebe, 2014) – but here, saprolite production and

chemical weathering occurs at depths greater than the average attenuation length of two meters (Buss et al., 2013). Thus, we interpret these values as rates of physical erosion (Dixon & von Blanckenburg, 2012) since the primary minerals except quartz are already lost below 2 m depth (White et al., 1998) in the relict landscape. The in-stream collection method assumes that a random sample of material actively transported by a stream represents an average of the landscape contributions above the collection site (Brown et al. 1995; Granger, Kirchner, and Finkel 1996; Bierman and Nichols 2004).

Samples were prepared in the Scripps Cosmogenic Isotope Laboratory, UC San Diego. Sediments were sieved and the 0.25-0.5 mm size fraction was purified until only etched quartz remained following an adaptation of the technique developed by Kohl and Nishiizumi (1992). A ^{9}Be carrier (Supplier Purdue Rare Isotope Measurement Laboratory, Designation 2017.11.17-Be) was added to each sample prior to quartz dissolution in hot, hydrofluoric acid. We separated Be from other elements following von Blanckenburg et al. (2004). We oxidized the samples over a flame to convert the BeOH to BeO, added niobium powder to the BeO powder, then packed the samples into a cathode target. The ^{10}Be/^{9}Be ratio of the samples was measured by accelerator mass spectrometry at PRIME Laboratory, Purdue University. Results were normalized to the 07KNSTD standard (Nishiizumi et al., 2007) with a ^{10}Be/^{9}Be ratio of 2.79×10^{-11} (Balco et al., 2009).

We calculate catchment average erosion (ε) from the ^{10}Be concentrations of the samples using equation 2 (Lal, 1991; Dunai, 2001), where *P(z)* is the shielding corrected production rate, *C(z)* is the nuclide concentration, λ is the ^{10}Be decay constant, Λ is the attenuation length, and ρ_s is the material density.

$$\varepsilon = \left(\frac{P(z)}{C(z)} - \lambda\right) * \frac{\Lambda}{\rho_s} \quad (2)$$

For this calculation, we assign a material density of 1.6 g/cm^3 representing the average bulk density of the weathered saprolite and calculate a ^{10}Be production rate with the CRONUS calculator from the latitude, longitude, and elevation of sampling locations and an assigned shielding correction (Balco et al., 2008). Shielding corrections assume vegetative shielding (Plug, Gosse, McIntosh, & Bigley, 2007), invariant bedrock composition within the catchment feeding area (Codilean, 2006) and without correcting for topographic shielding (DiBiase, 2018).

3. RESULTS

3.1. Field campaigns and digital terrain analysis

Springs in the field area were numerous (n=254, Figure 8) although smaller springs are not constantly flowing. Most of the springs are not yet associated with large erosional features, however, a sizable population (n=99) exist beneath amphitheatre-shaped erosion features with steep, vegetated headwalls (Figure 6). For these 99 channels, we calculated an average channel aspect ratio of 3.17 and a median of 3.15 (Figure 7). Observationally, seeps at the tips of channels emerge from saprolite well below the depth of the surface soil (ranging from 4-40 meters below the ridge crests) or clay translocation horizon, which suggests that the flow emergence is not determined by a transition in the material properties of the substrate. Initially, the water tends to flow meandering and unchannelized over a sandy substrate for short reaches before being concentrated into small tributaries with cohesive banks. Bank cohesion may be aided, but is not necessarily armoured, by the presence of roots, and banks are often composed of soft sediment. Channel beds are sandy, hosting ripple bedforms. These waters are red when they emerge, indicating the oxidation of dissolved iron at the subaerial transition out of the anoxic aquifer (Figure 6).

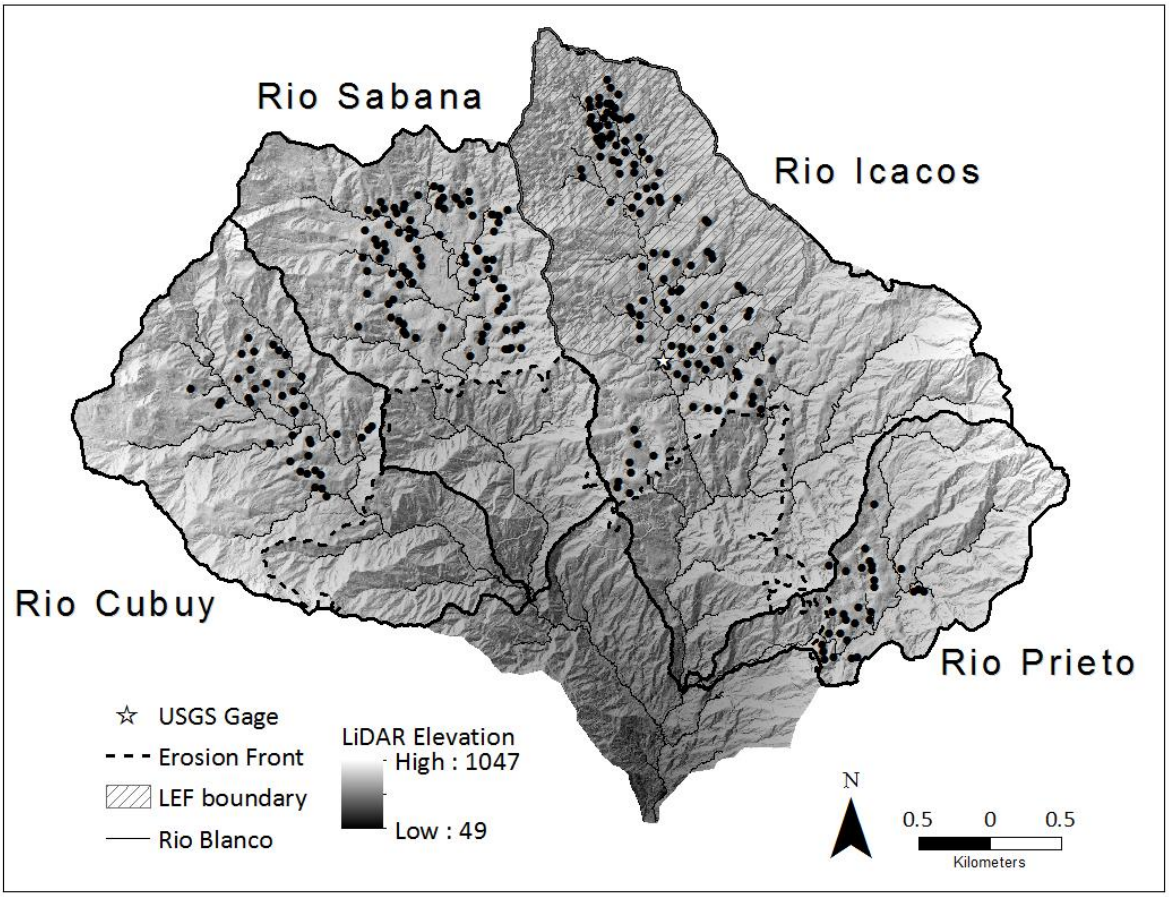

Figure 8 - Locations of springs within the Rio Blanco in black circles. Boundaries of the four major tributary rivers are identified by thick black lines. A dashed black line indicates the extent of knickpoint retreat up the river channels and the front of the erosive wave impacting the hillslopes. The location of the USGS gage on Rio Icacos and the boundaries of the Luquillo Experimental Forest are also identified

3.2. Baseflow discharge measurements

We tested several models for the scaling of groundwater discharge with the contributing drainage area. Our reported predictions come from a linear regression model with a slope derived as the mean of one thousand linear regressions run on an iterative, random sampling of the observations (9 out of 11) giving an r^2 value of 0.86. The model-predicted discharge values are plotted for the measured drainage areas of the 99 seep-tipped channels and model residuals are included as an inset (Figure 9). We tested various nonlinear models that had higher r^2 values, or more normally distributed residuals, but did poorly at very small drainage areas. The goal of the

modelling was to predict discharges of seeps where the flow was too low to be reliably measured in the field, and this guided our choice of predictive tool. The range of discharges into seep-tipped channels is 0.04 l/s to 4.4 l/s. These values are comparable to the groundwater discharges (1.1-1.9 l/s) measured in a series of wells along the riparian zone of a small tributary stream by Chestnut and McDowell (2000).

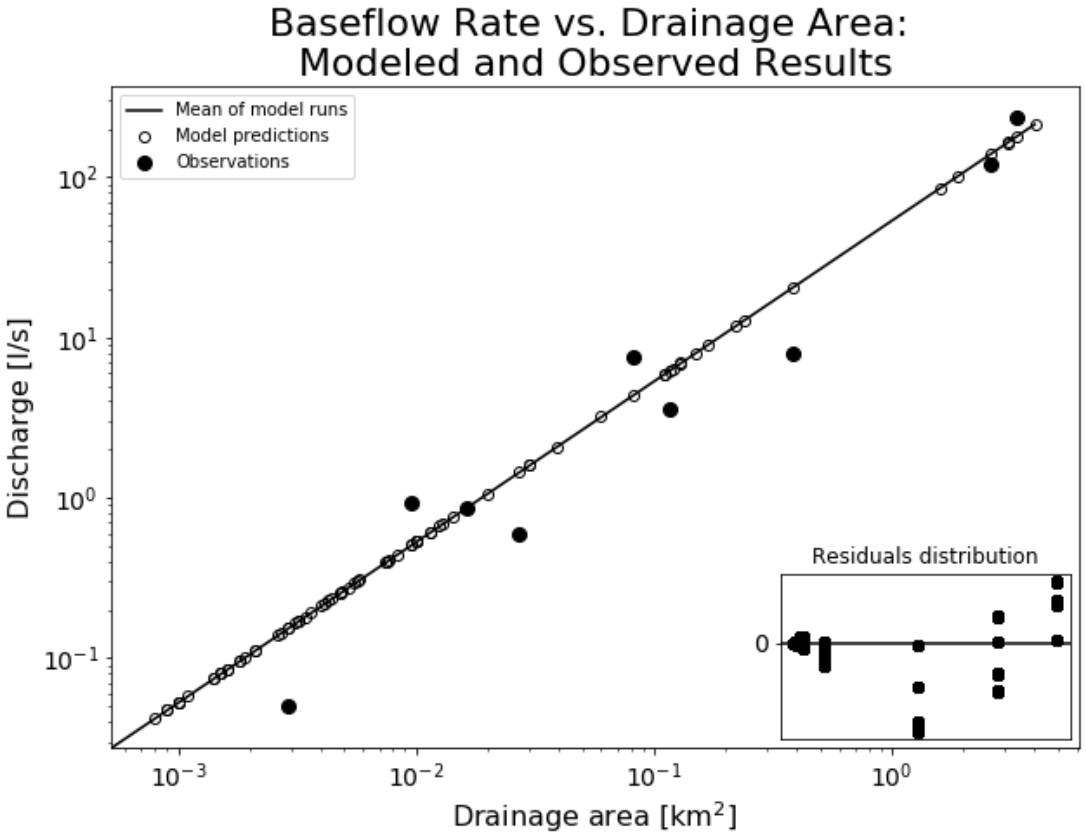

Figure 9 - A linear model relating the contributing drainage area to the baseflow discharge rate. Baseflow measurements made in the field for 11 sub-catchments with a range of contributing drainage areas. The black line represents the average outcome of iterative random resampling of the data and is the model prediction of the relationship between drainage area and discharge. The drainage areas of 99 additional catchments are plotted along the line showing the model-predicted range in baseflow discharge rate for seep-fed channels within the Rio Blanco. Residual distribution of the model is plotted in the bottom right inset.

3.3. **Bedload grain size analysis**

The D_{50} of the bedload sample is within medium sand size fraction 0.5-0.25 mm (Figure 10) which is similar to the median size of quartz grains in the saprolite (White et al., 1998). No grains larger than 2 mm were collected during the sampling. The critical shear stress for the incipient motion for this D_{50} is 0.194 – 0.27 N/m^2 (Berenbrock and Tranmer, 2008).

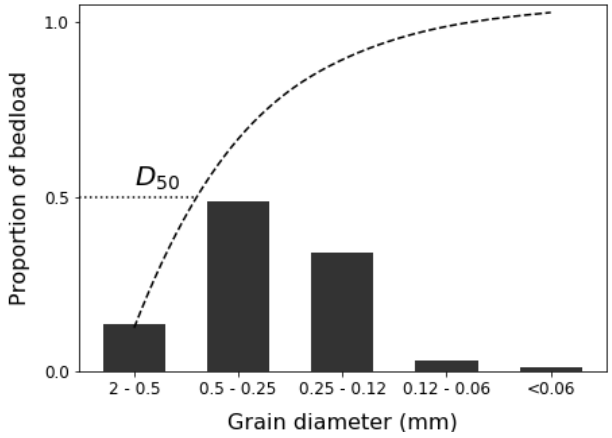

Figure 10 - Material mobilized under baseflow in a seep-fed channel, collected with a bedload sampler. Representative portion of size fractions plotted as a histogram, line plot showing the cumulative function of the size fractions. D_{50} is the median value of the cumulative function. Within size fraction 0.25-0.5 mm.

3.4. **^{10}Be derived erosion rates**

We measured erosion rates for five of the sapping channels in the Rio Blanco catchment with cosmogenic *in-situ* ^{10}Be (Table 1). These sites vary in their contributing drainage area (0.003-0.039 km^2), distance from the knickpoint, and were collected from two tributary catchments: Rio Icacos and Rio Sabana. ^{10}Be concentrations ranged from 287 - 88 x 10^3 atoms per gram, and four blanks had ^{10}Be/^{9}Be ratios ranging between 3.5 - 5 x 10^{-15}. Calculated erosion rates for the five channels range from 40 ± 3 m/My to 130 ± 10 m/My.

Table 1. Cosmogenic ^{10}Be derived erosion rates of sapping channels

Site ID	Lat	Long	Elevation (m)	Density	Shielding corr.	[10Be] atoms/g *	AMS Uncert. atoms/g %	Prod. rate (spall)	Erosion rate m/My	Rate Uncert. m/My
IC-GW2	-65.7884	18.288	623	1.6	0.98	134983	4623 3.4%	9.66	84.96	±7.16
IC-GW13	-65.7884	18.288	629	1.6	0.98	88491	1380 1.6%	9.71	131.43	±10.2
Sab-GW8	-65.7971	18.279	651	1.6	0.98	287067	5574 1.8%	9.91	40.01	±3.25
Sab-GW9	-65.7962	18.279	655	1.6	0.98	268924	4367 1.6%	9.95	42.96	±3.45
Sab-GW16	-65.8029	18.277	643	1.6	0.98	185315	3454 1.9%	9.84	62.43	±4.99

*The measured ratio of the carrier yielded a $^{10}Be/^{9}Be$ ratio of $0.5 \pm 0.1 \times 10^{-15}$.

4. DISCUSSION

4.1. Channel incision and seepage

Channel incision by seepage is a complex, multistep process, that has only been identified as a dominant erosive process in a limited number of environments (e.g. Abrams et al. 2009; Laity and Malin 1985). It encompasses the coalescing flux of groundwater through the substrate to a specific emergence point (spring), the undercutting of the slope above that emergence point leading to headwall collapse (sapping), and the entrainment and removal of material in the channel by spring discharged water. (Dunne, 1980, 1990) first described the circumstances for the formation of a seepage cut channel head: water percolating through a porous substrate moves in the direction of a gravitational gradient with a local baselevel set at the elevation of the stream network. Any heterogeneity in conductivity or porosity can act as the initial perturbation to concentrate flow across the field. Flow intensification initiates the removal of material, resulting in spatially varied curvature across the topographic surface. This change increases the hydraulic gradient, accelerating the flux of groundwater to the seep point. The positive feedback between flow concentration and erosion results in the formation of a channel whose source point is created

and fed by a spring. Continuing discharge must be sufficient to transport particles away from the face, or erosion by the seep will shut off (Lamb et al., 2006).

This suite of processes acting in concert produces channels with characteristic features. Channel heads are amphitheatre-shaped (Laity & Malin, 1985; Lamb et al., 2006; Petroff et al., 2011), as has been demonstrated in numerical simulations (Howard, 1988, 1995), sandbox models (Howard & Mclane, 1988) and observed in field studies (Abrams et al., 2009; Dunne, 1990; Higgins, 1982). At the channel head, the concentration of flow at the seep causes the back wearing of the slope to proceed faster than the widening of the valley walls (Dunne, 1980). The resulting channel aspect ratio (Figure 7) is numerically approximate to π (Petroff et al., 2011). The emergence of this geometry is not exclusive to sapping and to seepage (Lamb, Howard, Dietrich, & Perron, 2007; Lamb et al., 2006; Petroff et al., 2011). Therefore, although we observe these properties in the network of seep-tipped channels we study in the Rio Blanco, their form alone is not diagnostic of seepage driving channel incision.

What physical attributes of this study area could otherwise produce the channel form we observe and create uncertainty about the role of seepage erosion? We consider the presence of a clay-rich and cohesive topsoil, the influence of macropores on the subsurface hydrology (discussed in section 1.3), and the impact of flooding and vegetation on both disruption and stability of the channel network. Lateral zonation of grain size and hydraulic conductivity typically occur in the upper two meters of the ridgetop weathering profiles. In particular, a consistent, thick clay horizon exists ~35-50 cm below the surface that could impede or route subsurface flow. However, observations that the upper few meters of saprolite are typically unsaturated (Kurtz et al., 2011) suggest that the water table exists at sufficient depth for the groundwater flow field to be unperturbed by these zonation effects. Further, our finding that the majority of springs, and all

those flowing continuously, emerge well below the soil mantle indicates that the position of springs is not controlled by the soil structure. This site hosts a tropical rainforest, and plant roots are an important factor in sediment cohesion. Plant roots are visible (e.g. Figure 6) but so is scour behind the roots. Measurement of the differences in denudation between the ridgetops and the river channels indicates deepening incision for approximately 1.3 My (Brown et al. 1995).

The stage height of seep-fed channels rises quickly in flood conditions. Flood events are stochastic, but frequent (Phillips & Jerolmack, 2016; Pike et al., 2010) - and it is not possible to fully decouple the influence of flooding vs baseflow in the evolution of these small channels. However, the groundwater flux (i.e. baseflow) is sufficient to erode a small, seep-fed channel by collecting material moving as bedload during baseflow (section 2.3). We can approximate the role of groundwater discharge in channel erosion over longer timescales using ^{10}Be derived incision rates. Howard (1995) proposed that the incision rate of seep-eroded channels would be linearly related to the discharge of water at the seep. Abrams et al. (2009) demonstrate the consistency of this model with the channel network and hydrology of fluviodeltaic and marine deposits in the Apalachicola delta, Florida. To test this model in our field area, we compared baseflow discharge rates with sediment flux rates averaged over timescales of 10^4 years derived from ^{10}Be measurements (Figure 11). We make this comparison again for a population of streams with core-stone choked source points in the same watershed (data from Brocard, et al. 2016), where we do not expect groundwater discharge and erosion to scale dependently (Figure 11 inset).

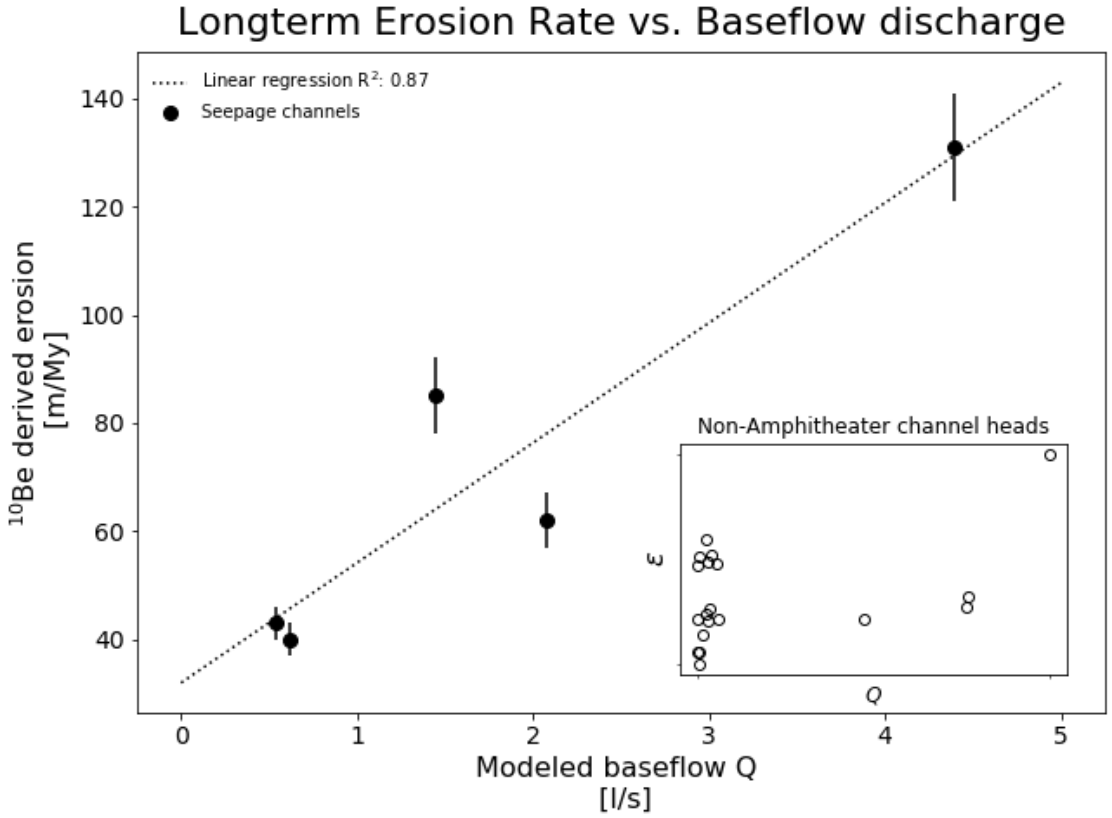

Figure 11 - Long-term erosion rates of five seep-fed channels are plotted vs. the baseflow discharge for each channel. Baseflow discharge rates were determined using the modelled relationship between drainage area and measured discharge presented in Figure 9. A linear regression between the two datasets has an r^2 value of 0.86. The inset on the lower right plots the ^{10}Be derived erosion rate of 19 river source points whose channel heads are choked with core stones, data from Brocard et al. (2016). We calculate the contributing drainage area of these 19 sub-catchments and plot this value vs the model derived baseflow rate. There is no significant correlation between these data (r^2 = 0.18).

For the seep-fed channels in this study, long-term incision rate has a strong, linear correlation with the baseflow discharge rate (r^2=0.87). This dependence is not expected for most fluvial systems but is believed to exist in sites where seepage erosion forms the channel network (Abrams et al., 2009; Dunne, 1980; Howard, 1995). No linear scaling between the baseflow discharge and the erosion rate exists in the 19 core-stone choked sub-catchments within the same watershed (r^2=0.18).

4.2. **Landscape (dis)equilibrium and seepage**

The four major tributary channels in the Rio Blanco are low-gradient and alluvium-bedded in their headwaters before plunging into a series of cascades downstream (Pike et al., 2010). The headward propagation rate of the knickpoints is slow ~1 mm/ky (Brocard et al., 2016). Therefore the initial outcropping of bedrock in the river channel proxies as a relatively stable baselevel for the trunk streams. However, multiple methods find geomorphic disequilibrium exists between the channel network and the topography upstream of the knickpoint (Brown et al. 1995; Stallard 2012). The erosion rates we measured in seep-fed channels (Table 1 and Figure 8) span a range comparable to the differences above and below the knickpoint reported by Brocard et al. (2015). What drives the differentiation between the stream channel and topography in this landscape, if it is not triggered by a change in the baselevel?

We have observed that groundwater discharged from springs can erode channels at short time scales, and find evidence suggesting this process may be important on longer timescales as well. Mechanistically, the lowering of the weathering front (deepening of the saprolite) would lower the emergence point of springs and could progressively entrench the channels forming by spring discharge. Exploring our data at a higher resolution we find there is spatial variation in the evidence for landscape change. At our sites in the Rio Sabana, channel incision rates match ridgetop erosion of ~40 m/My (Brown et al. 1995) suggesting a landscape in geomorphic equilibrium. In contrast, incision rates for similarly shaped, seep-fed channels in the Rio Icacos are higher than the erosion rate of the surrounding ridgetop topography. This disequilibrium indicates deepening relief by the channel processes.

^{10}Be measurements from the Rio Icacos seeps are comparable to the flux-weighted mean ^{10}Be concentration of Rio Icacos sediment. Brown et al. (1995) measured the ^{10}Be concentrations

of a range of quartz size fractions and determined the representative proportion of each size fraction in the bulk fluvial material. They used this measurement suite to estimate an approximate contribution of diffusive hillslope transport (~45%) and mass wasting events (~55%) to the stream load. Analogously, the Rio Sabana and Rio Icacos channels may be recording different erosive processes. Sapping describes the intermittent collapse of channel headwalls – an erosive style similar to the periodic contribution of sediment with low ^{10}Be concentrations delivered by landslides. An alternative mode for seepage erosion was proposed by Petroff et al. (2011), who predict coupling between the diffusion of hillslope transport and groundwater flux. Their model may apply in the Rio Sabana, where export of grains from the stream channel proceeds at the same rate as soil transport off of hillslopes.

How does geomorphic change restructure seepage processes below the knickpoint in contrast to what we observe in the relict topography? As principal lines of evidence, we take the absence of springs, the ubiquity of core-stones in channel heads, and data collected by Bhatt and McDowell (2007) finding that the concentration of weathering-derived solutes decreases sharply at the knickpoint boundary in Rio Icacos. The scarcity of springs in the adjusting topography may be due to the orographic increase in total precipitation with elevation in the watershed (Murphy et al., 2017). It could be caused in part by differences in the geomorphic structures affecting runoff, i.e. the lesser extent of floodplains and shallower depth to bedrock. We venture that the knickpoint boundary may also be a divide in average residence times of water in the subsurface due to these structural changes. Concentrations of weathering-derived solutes in streams depend on the residence time of water in the subsurface (Maher, 2010), which in turn is moderated by topographic form (Maher, 2011). For example, the neighbouring Rio Mameyes is watershed is underlain by faster-weathering and faster-eroding volcanoclastic bedrock, in which all traces of tectonic

adjustment have been completed (Pike et al., 2010). Solute concentrations in Rio Mameyes increase downstream reflecting longer flow lengths for groundwater entering the river channel away from the peaks (Scholl et al., 2015). In the adjusting topography of the Rio Blanco, we expect weathering in the near-surface to increase consistent with the erosion rate (Ferrier, Kirchner, Riebe, & Finkel, 2010; Hilley, Chamberlain, Moon, Porder, & Willett, 2010) enhanced by the presence of fresh mineral surfaces (Gabet & Mudd, 2009; Maher, 2010). This should *increase* the solute concentration of water discharged from hillslopes. The observed decrease in solute concentrations, therefore, is most likely caused by the increasing dominance of runoff over groundwater discharge.

5. CONCLUSIONS

This study examines spring emergence in a watershed that is geomorphically evolving in response to a tectonic perturbation. We find a large number of springs, both perennial and intermittent, in the relict portion of the topography but very few in the adjusting topography. Many springs in the relict topography emerge at the base of sandy, steep headwalls that form amphitheatre-shaped erosional depressions into ridgelines. These depressions form the heads of channels, that feed small tributaries to the river system. These channels have characteristics that match seepage-driven fluvial systems in other parts of the world, numerical models of sapping-generated topography, and experimental models of groundwater-incised channel networks. The baseflow into these channels is capable of transporting the channel bedload material and is, therefore, performing some portion of the geomorphic work in this river network. By measuring the baseflow discharge rates in a population of channels with varied drainage areas, we developed a model to predict the baseflow rate for sub-catchments within the watershed. From long-term channel incision rates measured with ^{10}Be, we determine that there is a linear scaling of channel

incision with the baseflow discharge rate in individual channels that appear to be formed and fed by springs.

ACKNOWLEDGMENTS

Data and the code for models are available online at https://www.hydroshare.org/resource/4bde564f41c146c68ce2d87a73f71526/.

Special thanks to Dr. Jon Lopez and Dr. Michael Lamb for helpful conversations that contributed to the advancement of this research. Thanks are due as well to the LCZO community and to our friends in Naguabo, Puerto Rico. This research was supported by NSF grants 1848637 and 1331841 awarded to Dr. Jane K. Willenbring.

Chapter two has been submitted for publication and has been accepted with revisions in the Journal of Geophysical Research: Earth Surface and will appear as: Harrison, E. J., Brocard, G. Y., Gasparini, N. M., Lyons, N. J., and Willenbring, J. K. Dynamic Critical Zone architecture driven by subsurface flow in the Luquillo Mountains, Puerto Rico. *Journal of Geophysical Research: Earth Surface.* (2020). The dissertation author was the primary investigator and author of this paper.

CHAPTER 3

QUATERNARY RECORD OF TERRESTRIAL ENVIRONMENTAL CHANGE IN RESPONSE TO CLIMATIC FORCING AND ANTHROPOGENIC PERTURBATIONS

Emma J. Harrison[1] • Gilles Y. Brocard[2] • Jane K. Willenbring[1]

[1] Scripps Institution of Oceanography, University of California San Diego, La Jolla, CA, USA.

[2] Institut des Sciences de la Terre, Observatoire des Sciences de l'Univers, University of Grenoble, France

ABSTRACT

Climatic change forces a response in the terrestrial environment. Our best understanding of these processes come from comparing proxy records of paleoclimate, paleo-ecology, and records of other processes, such as weathering and erosion, that are stored primarily in isotopes. Here, we present a 26 ky record of the ecosystem composition and the average physical erosion rate in the Rio Fajardo watershed. We derived these records from the river floodplain stratigraphy, using stable carbon isotopes to infer changes in the ecosystem and radiocarbon dating to constrain the stratigraphy. We present a new methodology for tracing erosion rates using $^{10}Be_{met}$ extracted from layers of the floodplain sediments. At the Pleistocene to Holocene transition, we see both records change gradually in response to warmer, wetter conditions in the Caribbean. In both records, we identify a state-change occurring approximately 5 kya in response to the intensification of ENSO and increased frequency and magnitude of tropical storm events. From that time forward,

both behavior in both systems pulsates in response to extreme disturbances, in a manner that reflects the modern behavior of the forest and mountain geomorphic processes.

1. INTRODUCTION

Predictions for the future suggest that Earth's climate will become increasingly varied and divergent from historic norms (Hoegh-Guldberg et al., 2018). How will these changes impact the surface of Earth where we live, and the terrestrial ecosystems on which we depend? We present a terrestrial proxy record from the Caribbean that spans the Quaternary period – a slice of time during which global climate changed dramatically. From the Pleistocene to the Holocene epochs, climate in the Caribbean became warmer, wetter and increasingly influenced by the El Niño/Southern Oscillation (ENSO) (Donnelly & Woodruff, 2007; Haug et al., 2011). In addition, the late Holocene marks the emergence of widespread, intensive anthropogenic land use.

In the context of this chronology, we present two proxy records from previously described, resampled floodplain stratigraphy of the Rio Fajardo (Figure 12), in north-eastern Puerto Rico (Mellon, 2000). Floodplain sediments accumulated from 26 ky BP to the present contain temporally and spatially contingent proxies of geomorphic activity and ecosystem composition. Basin-wide erosion rates are calculated from measurements of ^{10}Be concentrations in detrital sediment from radiocarbon-dated stratigraphic layers. Ecological change is inferred from stable carbon isotope ratios in sedimentary organic carbon. Both records contain periods of quiescence, of gradual change, and of dramatic changes attributable to external forcing. Ecogeomorphic systems in this watershed are dynamic and responsive to the regional climate and the human history of the island.

Earth surface processes and terrestrial ecosystems are both regulators of global-scale biogeochemical cycling. Carbon cycle models forecasting scenarios of anthropogenic climate change are driven by weathering/erosion and biotic uptake/release (Sarmiento & Gruber, 2002). Rates of change and the response sensitivity of these systems are areas of active debate (Herman & Champagnac, 2015; Norton & Schlunegger, 2017; Willenbring & Jerolmack, 2015). These systemic drivers respond to external forcing by the climate, but they also change in reaction to each other. Vegetation is hypothesized to regulate rates of geomorphic processes (e.g. Collins, Bras, & Tucker, 2004; Lyell & Deshayes, 1830) and landscape evolution can change ecosystem composition and structure (e.g. Wolf, Brocard, Willenbring, Porder, & Uriarte, 2016; Brocard, Willenbring and Scatena, 2019). Although sedimentary archives are among our most valued predictive tools (Franklin, Serra-Diaz, Syphard, & Regan, 2016) there are few instances where archives of terrestrial landscapes and ecosystems have been studied together (Marshall et al., 2015). When the external forcing changes significantly, do ecosystems and surface processes respond in sync, out of sync, or are they unresponsive? Tracing contemporaneous changes in the landscape and ecology of a single watershed reveals when behaviours are correlated and the differences that exist in the style or timescale of response to external perturbations.

Figure 12- Image of the Rio Fajardo floodplain exposed by river incision. A gravel mine in the watershed upstream of the sampling location has caused several meters of river incision in the last decade (personal communication) and exposed the floodplain stratigraphic section sampled in this study. Inset shows a close-up photograph of the profile that was sampled for analysis

1.1. **Sedimentary archives of ecogeomorphology**

Floodplains accumulate when rivers overtop their banks, and, unconfined by the channel walls, the flow spreads out and slows. Suspended sediment settles out of the low-velocity flow and is abandoned on the floodplain. Over time, this process leads to accumulated layers of sediment with the composition of the suspended load. The thickness and frequency of deposits laid down in floodplain stratigraphy is modulated by climate (Aalto et al., 2003), by changes in the sediment supply in the upstream watershed (Mertes, 1994), and by sea-level trends (Aslan & Autin, 1999). While floodplains occupy low gradient spaces with low surface erosion rates, sediment records preserved in floodplains are incomplete – especially in the deep past owing to hiatus and channel migration. The completeness of sedimentary records decreases with depth of time due to the intermittent nature of depositional processes. Sediment in is transported in pulses through fluvial channels (Leopold et al., 1964; Singh et al., 2009) and the cumulation of hiatuses in the sediment flux increases with the age of the depositional record (Schumer and Jerolmack, 2009; Jerolmack

and Sadler, 2007). Nevertheless, these terrestrial sedimentary archives provide unparalleled access into Earth's environmental, climatic and biological evolution (Berger, Vincent, & Thierstein, 1981).

River suspended loads include particulate organic carbon from plant litter and soil. Organic carbon is isotopically labelled by the plants that produce it (O'Leary, 1988). Stable carbon isotopic ratios (δ^{13}C) of organic material distinguish plant groups by their photosynthetic mechanism (Smith & Epstein, 1971). C_3 type plants (trees and shrubs) δ^{13}C ratios range from -26.5 $^{o}/_{oo}$ to -28.0 $^{o}/_{oo}$ (O'Leary, 1988; Tieszen, 1991). C_4 type plants (grasses and sedges) incorporate more ^{13}C, the heavier carbon isotope, and have δ^{13}C values falling between -12.5 $^{o}/_{oo}$ and -14.0 $^{o}/_{oo}$(O'Leary, 1988; Tieszen, 1991). Agricultural crops, such as corn and sugarcane, use the C_4 pathway (Tieszen, 1991). Freshwater phytoplankton are typically depleted in ^{13}C compared with land plants, having δ^{13}C values between -30$^{o}/_{oo}$ to -40 $^{o}/_{oo}$ (Rau, 1978). In the simplest case, organic material found in soil and litter has δ^{13}C ratio that matches the living plant material. Pools of organic matter, e.g. when it is stored in soils and sediments, have δ^{13}C values that integrate the isotope ratios of the carbon inputs. Organic carbon transported by rivers has a δ^{13}C ratio that represents a mixture of the biomass in the watershed (Hedges et al., 2000; Hedges, Turin, & Ertel, 1984; Thurman, 2012). As plant communities within the watershed shift, the changing ecosystem is reflected in the δ^{13}C ratios of organic material transported by the river. δ^{13}C has been used to assess the relative contribution of C_3 and C_4 plants to riverine organic matter in many global rivers (Bird, Fyfe, Pinheiro-Dick, & Chivas, 1992; Cai, Tan, & Edmond, 1988; Louchouarn, Lucotte, Canuel, Gagné, & Richard, 1997; Louchouarn, Lucotte, & Farella, 1999; Onstad, Canfield, Quay, & Hedges, 2000). Sedimentation of particulate organic material in floodplains records the history of ecological change within a watershed (Kohn, 2010; Planavsky, Partin, & Bekker, 2016).

Cosmogenic $^{10}Be_{met}$ ($t_{1/2}$=1.39 My) is produced in the atmosphere and delivered to Earth's surface with precipitation (Lal & Peters, 1967). The nuclide binds tightly to soil particles in the near surface, creating a reservoir that accumulates in proportion to the stability of the soil (Willenbring & von Blanckenburg, 2010). The erosion rate of the surface is calculated as the inverse of the $^{10}Be_{met}$ concentration (Jungers et al., 2009; von Blanckenburg, Bouchez, & Wittmann, 2012; Willenbring & von Blanckenburg, 2010) if the flux of $^{10}Be_{met}$ is known, and the site variables that may disassociate the nuclide from mineral surfaces is assessed. $^{10}Be_{met}$ has been widely applied as an erosion tracer in soils (Graly et al., 2010) on hillslopes (Jungers et al., 2009), in fluvial systems (Willenbring & von Blanckenburg, 2010), and marine sediments (Willenbring & von Blanckenburg, 2010b). However, this tracer has rarely been applied in terrestrial sedimentary contexts, where the $^{10}Be_{met}$ concentration in the each depositional layer contains an archived paleoerosion record (Jagercikova et al., 2015; Marshall et al., 2015)

2. FIELD SETTING

Rio Fajardo forms in the Luquillo Mountains in north-eastern Puerto Rico, then flows east to the Vieques Sound, an inlet body of the Atlantic Ocean. The bedrock lithologies are primarily interbedded volcanoclastic rocks and Quaternary alluvium filling the coastal plain (Figure 14) (Bawiec, 1999). The total catchment area is ~70 km^2. Rainfall in the headwaters is as high as 4500 mm/year and decreases to around 1500 mm/year along the coast (Murphy et al., 2017). Vegetation is zoned by elevation. The headwaters and mountain reaches are primary forest Tabanuco, Palo Colorado and Sierra Palm forest (Figure 15) (Lugo and Helmer, 2004). Along the coastal plain, the ecosystem today is largely abandoned pasture that has been reforested, with a portion remaining active cropland and pasture (Lugo & Helmer, 2004). The watershed delta is a developed urban area (USGS, 2001). Roughly 60% of the land area is dominated by C_3 type plants with $\delta^{13}C$

ratios between -26 and -30 $^{o}/_{oo}$. Nearly a third is actively cleared lands with mixed C_3 and C_4 species. These areas host an abundance of C_4 type plants whose $\delta^{13}C$ ratios range from -11 to -15 $^{o}/_{oo}$.

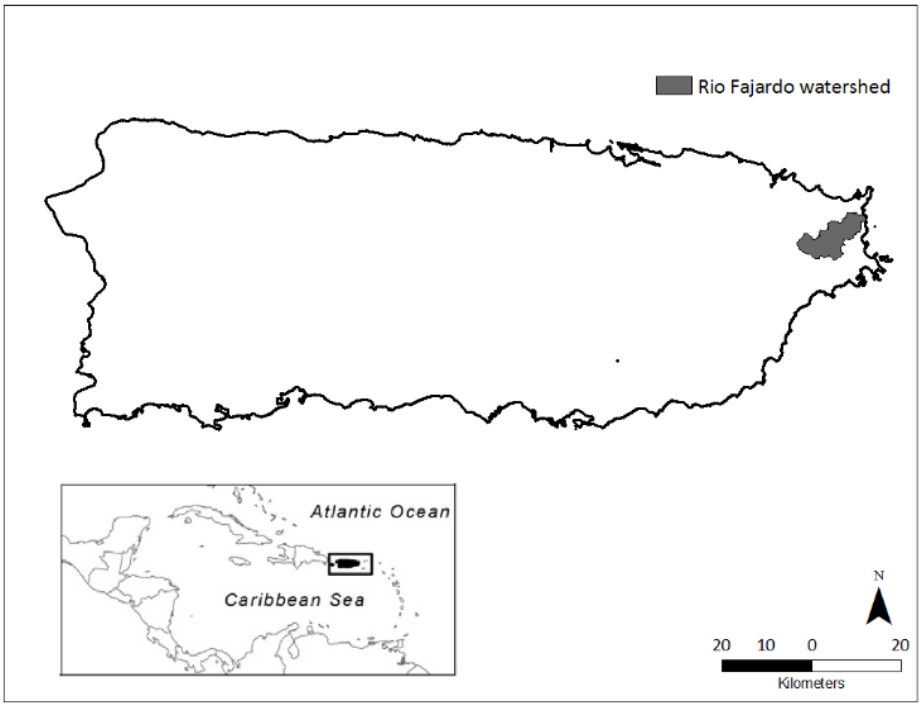

Figure 13- Map outline of Puerto Rico with the Rio Fajardo watershed area identified in grey shading. Inset map of the Caribbean with Puerto Rico identified, adapted from (Wood, González, Silver, Reed, & Cavaleri, 2019)

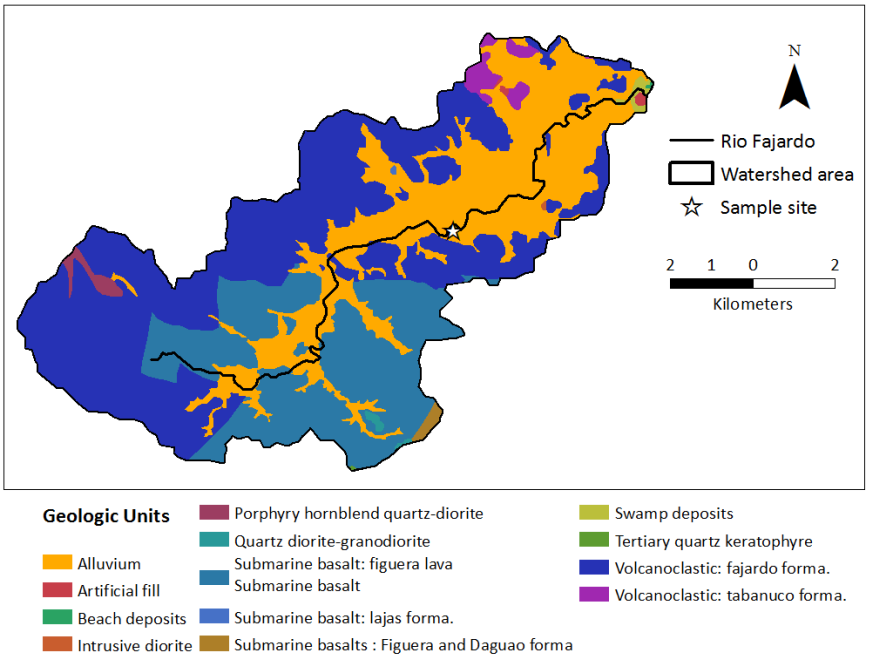

Figure 14 - Geologic map of the Rio Fajardo watershed adapted from (Walter J. Bawiec, 1999)

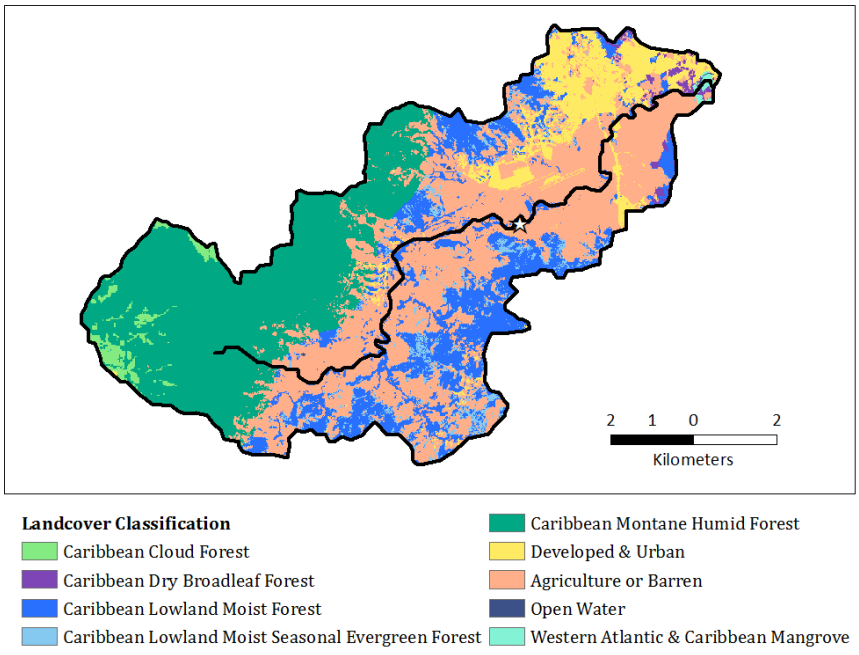

Figure 15 - Landcover units for the Rio Fajardo watershed adapted from (Homer, Huang, Yang, Wylie, & Coan, 2004)

3. METHODS

3.1. Radiocarbon dating

The chronology of the floodplain stratigraphy was established using radiocarbon measurements of organic material collected from the exposure at approximately 40 cm intervals from the surface to 2 m depth, and at 4.5 m depth. Samples were measured for ^{14}C at the University of Arizona Accelerator Mass Spectrometer (AMS) laboratory (Table 2) and previously reported in Mellon (2000). The samples were pre-treated, converted to CO_2 gas, and then reduced to graphite. The $^{14}C/^{12}C$ ratio of the graphite was measured via AMS. This ratio was used to calculate the radiocarbon age of the samples. We use the online Bayesian radiocarbon calibration tool BCall (Buck, Christen, & James, 1999) to determine probability distributions for the calibrated ages. Age of the samples between radiocarbon dates are inferred using linear interpolation.

3.2. Stable carbon isotopes

Stable carbon isotopes of organic material in the floodplain were measured at the Mountain Mass Spectrometry laboratory in Evergreen, Colorado (n=22). Replicates were sent for eight of the measurements to the University of Arizona for comparative analysis. Samples were measured for $\delta^{13}C_{org}$ using a Dumas combustion technique, in which combustion products are passed through a series of chemical and cryogenic traps to isolate the CO_2 gas. A helium carrier is used to transport the gas to the mass spectrometer ion source for analysis. Five replications produced a standard deviation of 0.2 parts per thousand. Results are reported in δ notation (Table 3):

$$\delta^{13}C_{org} = \left[\left(R_{sample} - R_{std}\right)/R_{std}\right] \times 100 \quad (1)$$

3.3. **Meteoric ^{10}Be concentrations**

Chemical extraction of ^{10}Be was performed in the University of Pennsylvania Cosmogenic Isotope Laboratory following procedures described in (Valletta, Willenbring, Lewis, Ashworth, & Caffee, 2015). A ^{9}Be carrier (Supplier Purdue Rare Isotope Measurement Laboratory) with a ^{10}Be/^{9}Be ratio of $0.5 \pm 0.1 \times 10^{-15}$ was added to each sample. The ^{10}Be/^{9}Be ratio of the samples was measured by accelerator mass spectrometry at PRIME Laboratory, Purdue University. Results were normalized to the 07KNSTD standard (Nishiizumi et al., 2007) with an assumed ^{10}Be/^{9}Be ratio of 2.79×10^{-11} (Balco et al., 2009).

Erosion rates are calculated following (Willenbring & von Blanckenburg, 2010):

$$E = \frac{Q}{\rho N_{surf}} \quad (2)$$

Where E is an erosion rate that averages erosion rates from the contributing areas of the watershed at the time the given sedimentary sequence was being deposited in the floodplain; we use a value of 8.70E+05 for Q, the flux of $^{10}Be_{met}$, which we assume to be constant on the timescale of soil ages in the catchment (Willenbring & von Blanckenburg, 2010); ρ is a density term for which we use an average value of 1.59 g/cm^3 and N_{surf} is the measured concentration of $^{10}Be_{met}$ extracted from the sediment sample. We use the sampling latitude to derive the $^{10}Be_{met}$ flux predicted by General Circulation Models (Heikkilä et al. 2008, 2013). Global datasets of $^{10}Be_{met}$ fluxes do not show unlimited supply in high precipitation environments (Willenbring & von Blanckenburg, 2010) therefore, we do not use a precipitation-scaled flux rate (Graly, Reusser, & Bierman, 2011). We account for the impact of $^{10}Be_{met}$ fallout on the surface of the floodplain using an aggradation rate of 0.02 cm/year based on the total thickness and age of the deposit. Erosion rates accounting for this in situ flux differ by <0.01%.

3.4. **Grain size and geochemistry**

Five meters of floodplain stratigraphy were sampled at 20 cm increments. Samples were measured for their grain size distribution, elemental composition, and organic carbon content. Macromorphological observations of horizons include texture, structure, the presence of roots and voids, and grain coatings (Figure 16). Elemental concentrations were measured with a Perkin Elmer Emission Spectrometer Plasma 400 ICP AES after a lithium metaborate and lithium tetraborate digestion. Canadian Certified Reference Materials Soil-2, Soil-3, and Soil-4 were used as standards. Samples with high Fe and Si were diluted to 1:2 and 1:5 concentration respectively. Standards were within 5-10% of reported values. Concentrations of Al-Ca-Sr-Ti-Zr, Ba-Mg-Mn-P, K-Na, Fe and Si are available in the online data repository. Results are presented as ratios calculated to show the relative degree of change throughout the profile (Figure 17). Calculated weathering ratios are the base cation loss (Retallack, 2008) the chemical index of weathering (Harnois, 1988) and salinization.

$$\textit{Base cation loss} = Al_2O_3/(CaO + MgO + Na_2O + K_2O) \quad (3)$$

$$\textit{Chemical Weathering Index} = [Al_2O_3/(Al_2O_3 + CaO + Na_2O)] \times 100 \quad (4)$$

$$\textit{Salinization} = Na_2O / K_2O \quad (5)$$

4. RESULTS

4.1. **Stratigraphy and Chronology**

Our sampling location is a cut bank exposure of ~5.5 meters of sediment above a layer of alluvial cobbles. The top 50 cm of the sediment column is bioturbated, brown soil with voids and roots (Mellon, 2000). Below the modern soil cover, sediment exhibits greater structural

development and clay concentration increases. The profile from 50 cm to ~2 m depth is yellow-brown to yellow-orange with a moderate columnar to blocky structure, with exception to two distinct but narrow bands in the deposit (see Figures 16&18). There is a single layer of sub-rounded basalt pebbles (D_{50}=4.5 cm) at 80 cm depth. The lithology of this pebble band is consistent with the alluvial cobbles at the base of the cut bank exposure. At a depth of ~1 m is a 20 cm thick band of sediment with a light grey colour that exhibits a small number of 2-5 mm diameter Fe-nodules. From ~2 m to the cobble deposit at ~5.5 m the exposed profile is strongly plinthic, highly weathered and Fe-rich, with a high clay content and massive structure (Mellon, 2000).

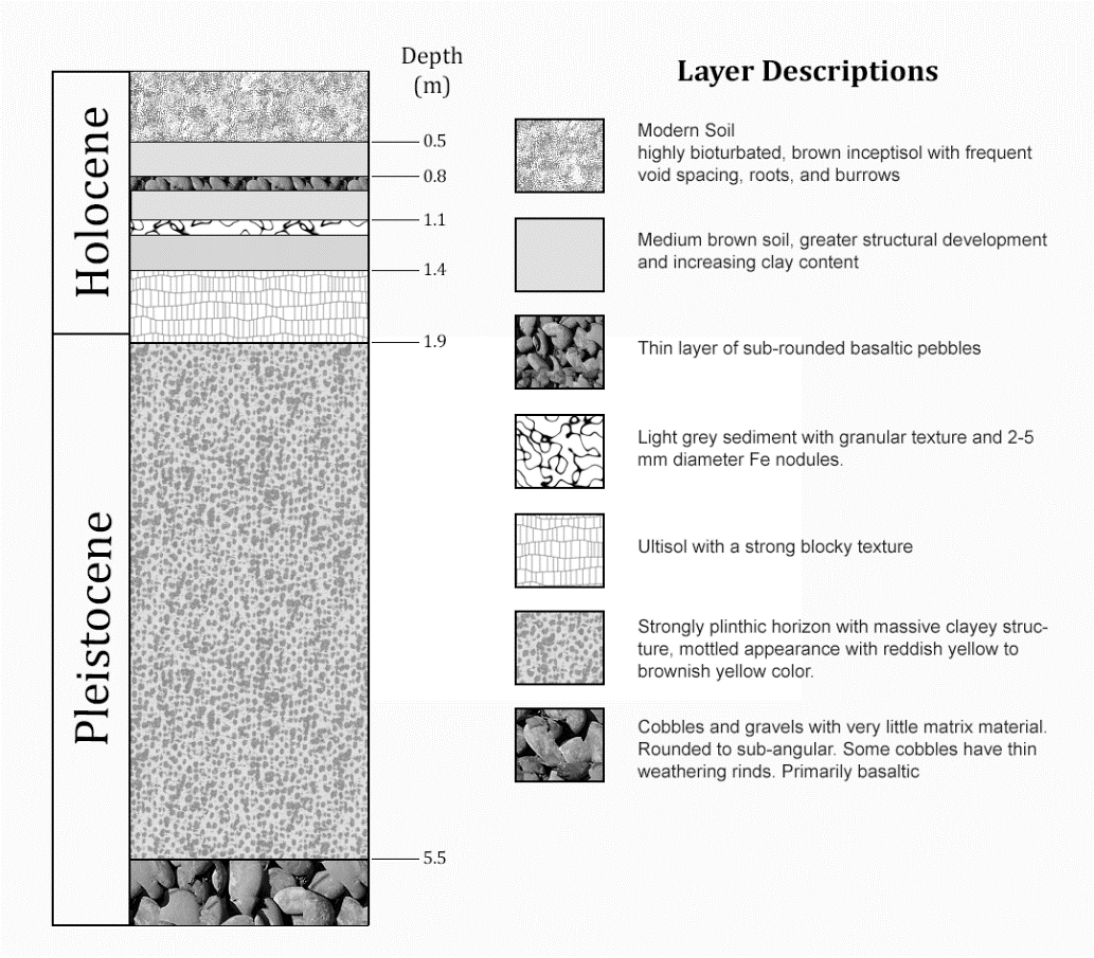

Figure 16 - Stratigraphic column and layer descriptions adapted from Mellon (2000)

The dated stratigraphic section is bookended with calibrated radiocarbon ages of 22,223 +/- 173 and 504 +/- 31 years BP (Table 2). Based on the age and thickness of the layers, we infer a gradually increasing sedimentation rate at this site, averaging ~20 mm/yr during the Pleistocene and early Holocene, and approximately doubled in the most recent two thousand years of the record. Increasing sedimentation rate is an expectation for a river system whose gradient is influenced by rising sea levels, which is documented for the Caribbean during this time span (Khan et al. 2015, 2017; Fairbanks, 1989).

Table 2. Calibrated radiocarbon ages and interpolated age of the floodplain

Depth	**^{14}C**	**+/-**	**Bcal**	**Bcal**	**age**	**+/-**	**Interpolated age**
m	years BP	years BP	min	max	years BP	68%	years BP
0.2	450	40	473	534	503.5	30.5	504
0.6	1325	55	1185	1297	1241	56	1241
0.8	1910	60	1812	1928	1870	58	1870
1.2	3920	160	4151	4532	4341.5	190.5	4342
1.6	5340	65	6025	6196	6110.5	85.5	6111
1.9	8975	65	9949	10227	10088	139	10088
4.4	18380	210	22050	22396	22223	173	22223

We interpret the chronology of the floodplain deposits using linear interpolation between the radiocarbon measurements, which assumes a constant deposition rate. Long hiatuses in sediment deposition or significant erosion of the surface would make this inappropriate. The stratigraphy shows no evidence of buried soil horizons, and the color and geochemical indices of the sediment are consistent with depth (Figure 17), suggesting it is unlikely that the floodplain was

abandoned for a lengthy time (Kraus & Aslan, 1993). Consistent grain sizes for most of the profile (Figure 17) suggests that the transport energy remained similar over the accumulation record. In the most recent 5 ky environmental proxies show dramatic fluctuations. For this part of the record we increased the density of radiocarbon sampling, in order to reduce the uncertainty inherited from the linear age interpolation method.

4.2. **Grain size and geochemistry**

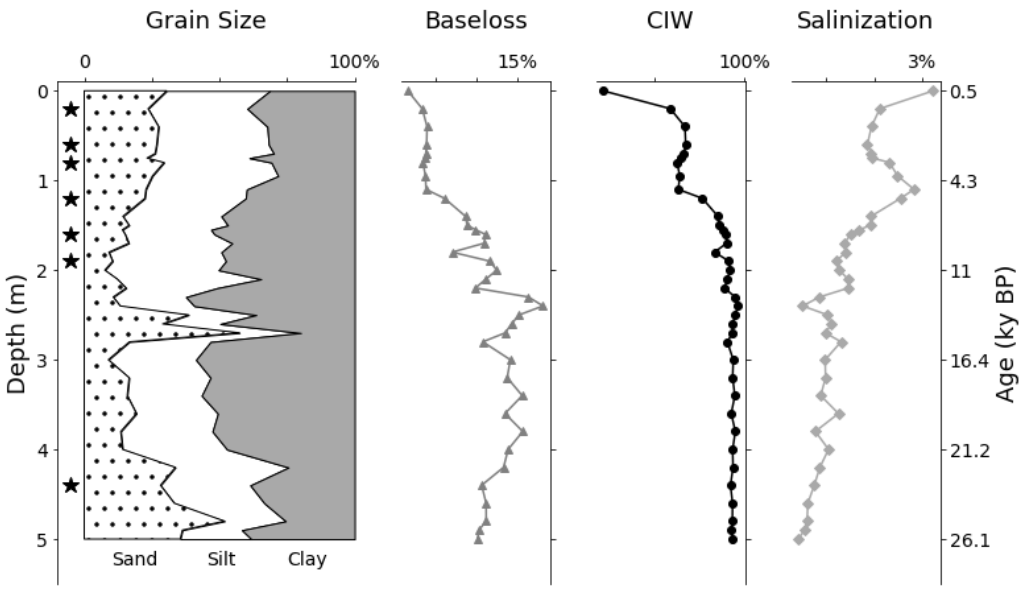

Figure 17 - Depth distribution of grain size shown in cumulative percent, the calculated geochemical indices Baseloss and Chemical Index of Weathering, and the location of radiocarbon samples.

Two anomalies are present in the grain size distribution: a sandier unit at ~2.6 m depth and a thin layer of gravels deposited 80 cm below the modern surface. Excess sand may be deposited during particularly large floods (Zwoliński, 1992), by crevasse splays (Burns, Mountney, Hodgson, & Colombera, 2017), or lateral accretion (Wolman & Leopold, 1957). Radiocarbon dating indicates deposition between 13.6-14.5 ky BP, during which time a spike in the rate of sea level rise is recorded in Caribbean sea level proxies (Fairbanks, 1989; Khan et al., 2017). Spiking sea levels could have affected river dynamics, causing aggradation that increased the frequency of

avulsions and/or sandy overbank deposits (Swanson et al., 2008; Weerts & Bierkens, 1993). As other sedimentary proxies and environmental change records are steady over this interval, these events are unlikely to have a large effect on the ecogeomorphic archive interpretation. Radiocarbon dates above and below the single layer of sub-rounded basalt gravels at ~80 cm depth constrains their deposition between 1.8-1.9 ky BP. The gravels are not continuous over bank exposure. In this section of the river, we observe some braiding and splitting of the river channel – and so consider it is possible that these stones were laid down by a smaller channel briefly flowing over the floodplain before being integrated into the main stem. An event like this would potentially affect the depositional record, however, the lithology of the gravels is the same material actively transported in the modern channel and forming the cobble deposit at the base of the floodplain. Therefore, we are confident that the source material entering the deposit should be derived from the same region.

4.3. Erosion rates from ^{10}Be

$^{10}Be_{met}$ derived erosion rates (Table 3) during the Last Glacial Maximum range from 69 ± 1.2 mm/ky to 93 ± 1.3 mm/ky. Thereafter, erosion decreases from 52.5 ± 1.0 mm/ky at 21 ky BP to a minimum of 13.4 ± 0.3 mm/ky at 12.3 ky BP, just before the transition to the Holocene. Early Holocene erosion rates are modest, with an early maximum of 79 ± 1.8 mm/ky at 11.2 ky BP and stable until ~4.3 ky BP. At that time, erosion more than doubled to 135 ± 2.7 mm/ky and remains high into the present. In this later time period, erosion rates fluctuate greatly between measured intervals, peaking at 356 ± 16 mm/ky at 500 years BP. The most recent erosion rate measured from the exposed surface is 111 ± 1.6 mm/ky. Erosion is plotted against the interpolated age of the deposit in Figure 20 in the discussion.

Table 3. $^{10}Be_{met}$ in floodplain sediments and calculated erosion rates

PRIME lab #	Sample depth	^{10}Be concentration	AMS uncertainty	Erosion rate
	m	atoms g^{-1}		mm/ky
201202860	0	4.92E+07	1.48%	111
201202861	0.13	2.47E+07	1.71%	222
201202862	0.19	1.54E+07	4.55%	356
201202863	0.44	2.72E+07	2.21%	201
201202864	0.69	3.63E+07	2.08%	151
201202865	0.95	6.66E+07	1.59%	82
201202866	1.2	4.05E+07	2.00%	135
201202867	1.38	1.07E+08	1.50%	51
201202868	1.55	1.18E+08	1.32%	46
201202869	1.73	9.24E+07	1.71%	59
201202870	1.9	9.48E+07	1.64%	58
201202871	2.12	6.94E+07	2.27%	79
201202872	2.34	4.09E+08	2.61%	13
201202873	2.56	1.39E+08	2.36%	39
201202874	2.78	1.51E+08	1.24%	36
201202875	3.0	2.54E+08	1.28%	22
201202876	3.22	1.22E+08	1.07%	45
201202877	3.44	1.26E+08	3.64%	43
201202878	3.66	1.41E+08	0.98%	39
201202879	3.88	1.41E+08	0.97%	39
201202880	4.1	1.51E+08	1.22%	36
201202881	4.32	1.04E+08	1.82%	53
201202882	4.54	7.32E+07	1.12%	75
201202883	4.76	5.86E+07	1.35%	93
201202884	4.98	7.89E+07	1.68%	69
201202885	5.2	6.42E+07	1.67%	85

4.4. **Stable carbon isotope ratios**

For the duration of the Pleistocene the average δ^{13}C value is -26.28 $^{o}/_{oo}$ with a standard deviation of 1.36, reflecting a relatively stable biomass structure. There is much greater variability during the Holocene, δ^{13}C values range from -25.6 $^{o}/_{oo}$ in the first Holocene sample (12.5 ky BP) to -15.291 $^{o}/_{oo}$ 504 years BP. δ^{13}C values closer to 1 reflect greater incorporation of the heavy carbon isotope ^{13}C. There are several time periods in this record exhibiting distinct trends, described in Table 6 in the discussion. Analytical errors for the δ^{13}C measurements are <2%. The replicate measurements at the University of Arizona are generally in good agreement with the measurements made at the Mountain Mass Spectrometry Lab, but in one case deviates by a significant value (4.77 $^{o}/_{oo}$). This variability can either represent differences in the lab processing or variability between separates from the same depositional layer of the floodplain.

Table 4. Stable carbon isotopes of sedimentary organic carbon

Depth m	$\delta^{13}C$ Mountain Mass Spectrometry	$\delta^{13}C$ University of Arizona
0.2	-17.275	-15.291
0.4	-21.39	
0.6	-24.805	-21.332
0.7	-24.97	
0.8	-22.265	
0.95	-21.66	
1.1	-20.615	
1.2	-19.465	-19.776
1.4	-23.62	
1.6	-24.265	-21.136
1.8	-22.155	
1.9	-24.09	-24.372
2.2	-23.38	
2.4	-25.6	
2.6	-24.945	-29.715
3	-25.875	
3.4	-26.07	
3.8	-26.28	
4.4	-25.59	-26.846
4.8	-24.753	
4.9	-25.82	
5.2	-26.135	-27.103

5. DISCUSSION

5.1. Paleo-erosion record

Interpreting paleo-erosion rates from the floodplain sediments assumes that the $^{10}Be_{met}$ concentration of suspended sediment is a valid representation of the average erosion in the river catchment today. To interrogate this, we use the nearby Bisley watershed as an analogue because it is underlain by the same volcanoclastic bedrock formation and has been studied for decades as part of the Luquillo Experimental Forest (Scatena, 1989). To accurately calculate soil residence time, $^{10}Be_{met}$ must be retained in the near-surface. Whether it exists as a hydroxide compound or as an organic complex, Be binds tightly to sediment where the environmental pH is greater than

four (Willenbring & von Blanckenburg, 2010; You, Lee, & Li, 1989). Spatially extensive measurements of soil pH in the Bisley watershed ranged from 4.7-5.3 (Silver, Scatena, Johnson, Siccama, & Sanchez, 1994) which suggests Be retention. We measured $^{10}Be_{met}$ in a surface soil (0-10 cm) and in a sample exposed by a landslide scar (160-170 cm) to look for evidence of leaching or translocation. The surface soil $^{10}Be_{met}$ concentration was an order of magnitude higher than the landslide exposure (Table 5).

The Bisley surface soil yields an erosion rate approximately double that of the measurement from the top ten cm of the Fajardo floodplain. This is reasonable, because the Bisley soil represents a point measurement from the steep mountain peaks, whereas Rio Fajardo at the floodplain integrates a significant area of lowlands. High rates of chemical erosion in a Bisley weathering profile likewise reflect the difference in mass loss on the peaks compared to lower in the watershed (Dosseto, Buss, & Suresh, 2012). In June of 2011 we collected a bucket of water from Rio Bisley during the early stages of a flood event. We separated suspended sediment using a 0.7 μm filter and measured the concentration of $^{10}Be_{met}$ for the load. The yield was similar to the modern floodplain deposit, suggesting that $^{10}Be_{met}$ concentrations are a valid approximation for catchment-averaged erosion in the watershed today.

Table 5. $^{10}Be_{met}$ concentrations in Bisley watershed soils and active channel

Site	$^{10}Be_{met}$ atoms g^{-1}	AMS Uncertainty
Fajardo floodplain sediment 0-10 cm	4.92E+07	1.48%
Surface soil in Bisley 0-10 cm	2.46E+07	3%
Landslide scar in Bisley 170 cm depth	5.52E+06	28%
Bisley suspended sediments 1.7 ft flood stage	2.65E+08	2%

Floodplain accumulation is an inherently selective process that preferentially retains small particles. We explore the bias introduced by sorting during entrainment to determine whether floodplain settings can be meaningful paleo-erosion proxies. The first question is whether the sub-sample of sediment retained in the floodplain carries a $^{10}Be_{met}$ concentration that is representative of the suspended sediment population as a whole. Willenbring & von Blanckenburg (2010) measured $^{10}Be_{met}$ variability within size fraction populations, finding a tight distribution of $^{10}Be_{met}$ concentrations in small size fractions. Furthermore, Boschi and Willenbring (2016) measured the strength of Be sorption under a range of conditions, and found that grain size was among the least important variables in sorption capacity. Certain mineralogies have stronger Be sorption than others (Boschi & Willenbring, 2016) however, clay mineral abundances and total % clay in our

samples do not correlate with concentrations of $^{10}Be_{met}$ (Figure 18). Therefore, we find no evidence of $^{10}Be_{met}$ redistribution following deposition in the floodplain. We note that the two peaks in $^{10}Be_{met}$ concentration occur at 10,088 and 13,398 years BP, each approximately 1000 years after the two major pulses in sea level rise rate recorded in Caribbean sea level proxies (Fairbanks, 1989; Khan et al., 2017).

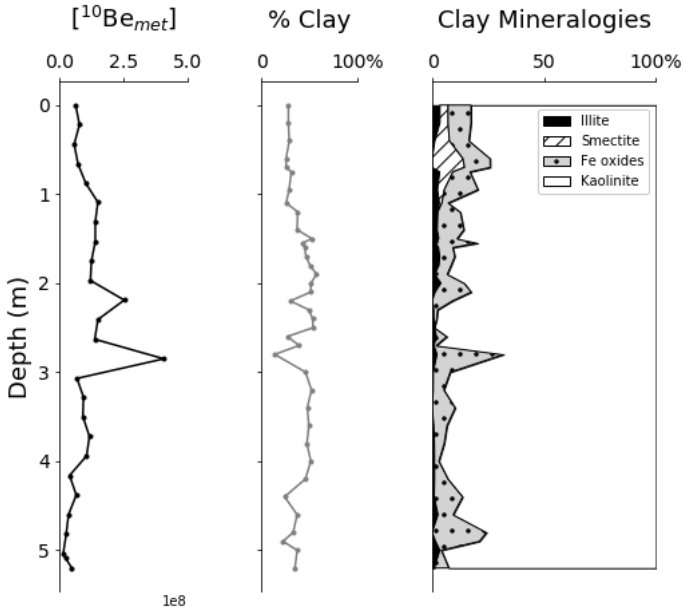

Figure 18 - Distribution of $^{10}Be_{met}$ concentration, percent clay, and clay mineral abundances. $^{10}Be_{met}$ concentrations are in 10^8 atoms gram^{-1}. Total clay and the abundance of clay minerals are plotted as a percentage of the total mass. The peak in ^{10}Be is at 2.63 m depth and the minimum percent clay and maximum percent Fe-oxides is at 2.8 m depth.

5.2. Carbon sources and evidence for ecological succession

Pools of organic matter, such as is stored in soils or sediments, have $\delta^{13}C$ ratios that integrate the $\delta^{13}C$ values of source material. Decomposition further fractionates these isotopic ratios, such that the $\delta^{13}C$ value of the bulk material becomes more like the $\delta^{13}C$ of the recalcitrant fraction. Marin-Spiotta et al. (2009) reported measurements of Puerto Rican soil organic matter in primary and successional stand forests and agricultural fields to quantify the outcome of microbial decomposition and humification on the bulk $\delta^{13}C$ ratios. Litter in primary forests contained high-

density, decomposition-resistant fractions that were depleted in ^{13}C relative to the light, quickly-recycling fractions. With time, the bulk $\delta^{13}C$ progressed towards the ^{13}C depleted, heavy-fraction component. $\delta^{13}C$ ratios of Tabanuco forest living biomass and litter from von Fischer and Tieszen (1995) show the same trend of old litter being ^{13}C depleted relative to wood and roots. Marin-Spiotta et al. (2009) found the opposite pattern in pastures, reflecting different organic carbon inputs. Decomposition rate and the residence times of organic soils on hillslopes can vary greatly within a given watershed, and often correlates with the local erosion rate.

A study of riverine organic carbon in active transport along the Rio Fajardo channel found that the $\delta^{13}C$ of particulate carbon changed downstream (Moyer, Bauer, & Grottoli, 2013). Carbon in the river headwaters was dominated by forest litter and soil organic matter. Downstream, where the watershed area contains more agriculture and grassland, the river integrates a larger percentage of ^{13}C-enriched sources. Their study found that organic carbon in the headwaters had modern radiocarbon ages due to short soil residence times and fast erosion on steep mountain slopes. At the downstream sampling location a few tens of meters away from our floodplain site, particulate organic carbon ranged from modern to ~200 years old. Integration of shallower slopes with slower erosion increased the residence time of carbon sources at lower elevations in the watershed.

Young particulate organic carbon in the active channel reduces several uncertainties associated with carbon archived in the floodplain. First, it suggests minimal alteration by decomposition of organic matter prior to fluvial transport. Also, that radiocarbon ages are probably modern, or close to it, when carbon is entrained in the floodplain. Decomposition is slow in floodplain sediments due to anoxia, which promotes preservation of organic carbon (Boye et al., 2017). Oxidation of organic material during fluvial transport and transient storage is documented for large watersheds (Bouchez et al., 2010; Galy, France-Lanord, & Lartiges, 2008) but Rio

Fajardo is a small, steep catchment where carbon is unlikely to degrade during transport in the channel (Scheingross et al., 2019).

We compare δ^{13}C values of sedimentary organic matter in the Fajardo floodplain to carbon sources in the Fajardo watershed (Figure 19). Pleistocene-age organic carbon overlaps tightly with the δ^{13}C of forest biomass, litter, and soil organic matter. There is only a narrow band of overlapping δ^{13}C values between Pleistocene and Holocene-age sedimentary carbon. All Holocene-age samples are significantly enriched in ^{13}C relative to samples from the Pleistocene. Climate change can affect the δ^{13}C of plants because they respond to changing water availability and temperature with behaviours that affect their carbon uptake during photosynthesis (Farquhar, Ehleringer, & Hubick, 1989; O'Leary, 1988). The δ^{13}C of most C_3 plants increases slightly as the plant responds to higher temperature and aridity. The effect of glacial/interglacial climates can produce intra-species variations of ~2 $^{o}/_{oo}$ (Heaton, 1999). The differences between Pleistocene and Holocene age carbon in the Fajardo floodplain is greater than this value, indicating new biomass derived from C_4 plants. The magnitude of change is evidence that the pattern is caused by ecological succession in the Fajardo watershed over time.

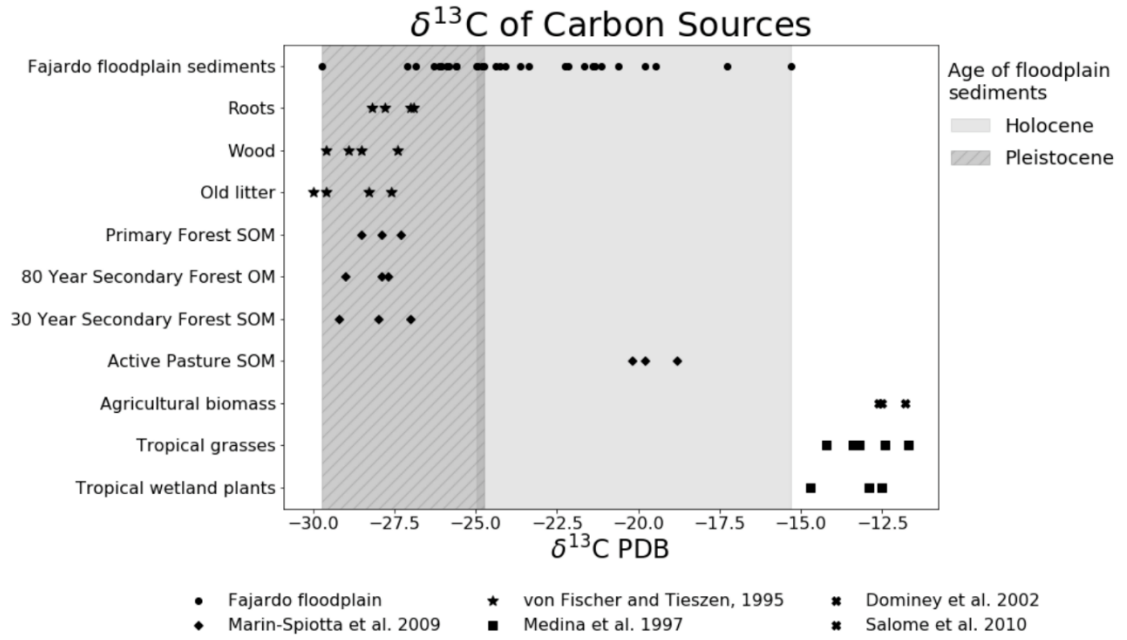

Figure 19 - $\boldsymbol{\delta}^{13}$C ratios of organic carbon that potentially source the material transported by Rio Fajardo. The $\boldsymbol{\delta}^{13}$C distribution of the samples collected from the Fajardo floodplain are plotted, and the radiocarbon calibrated ages of the carbon are indicated by the shaded regions. Light grey shading represents the extent of $\boldsymbol{\delta}^{13}$C values for organic material of Holocene age. Grey shading with hatch marks indicates the range of $\boldsymbol{\delta}^{13}$C values for organic carbon of Pleistocene age. Literature sources of $\boldsymbol{\delta}^{13}$C values are cited in the legend

5.3. Agents of ecogeomorphic change

5.3.1. Climate change

The modern Caribbean climate is dominated by three factors: the position of the Intertropical Convergence Zone (ITCZ), the intensity of the El Niño/Southern Oscillation (ENSO) and the North Atlantic Oscillation (NAO) (Enfield, 1996; Enfield & Alfaro, 1999). Annual seasonality is more pronounced in precipitation than in insolation (Giannini, Kushnir, and Cane 2000). Paleoclimate proxies spanning the Quaternary indicate that region was sensitive to climate perturbations in North America and the northern Atlantic, e.g. the Heinrich events, the Younger Dryas, and the Little Ice Age (Haug et al., 2011; Peterson & Haug, 2006). Generally, the transition from the Pleistocene to the Holocene (~12.6 ky BP) marks increasing temperatures and humidity around the Caribbean (Bradbury, 1997; Fensterer et al., 2013; L. A. González & Gómez, 2002;

Haug et al., 2011; Hodell et al., 1991). However, proxy records demonstrate that the Caribbean region is a complex mosaic of microclimates. Climate patterns can split abruptly along longitudinal boundaries due to the relative influences of the North Atlantic Ocean, Gulf of Mexico, and Pacific Ocean on landmasses within the region (Bradbury, 1997; Leyden, Brenner, Hodell, & Curtis, 1994; Metcalfe, Bimpson, Courtice, O'Hara, & Taylor, 1997)

At the decadal scale, climate variability is driven by the ENSO cycle (Giannini, Cane, and Kushnir 2001). During El Niño years, the trade winds are stronger, sea surface temperatures cooler, and seasonality is more extreme in the Caribbean and tropical Atlantic Ocean (Giannini, Cane, and Kushnir 2001). Either the onset of ENSO cycles or a dramatic uptick in ENSO activity at ~5 ky BP is indicated by modelling studies (Clement, Seager, & Cane, 2000), geoarchaeological evidence (Sandweiss, Richardson, Reitz, Rollins, & Maasch, 1996), and paleoclimate reconstructions from proxy data (Rodbell et al., 1999). From 4-2.8 ky BP appears as particularly intense ENSO cycling in proxy records (Haug et al., 2011; Rodbell et al., 1999). For this interval, speleothems record anomalously high precipitation in Puerto Rico, and floods disrupted the occupation patterns in two major archaeological sites on the north and south coasts of the island (Rivera-Collazo et al., 2015).

The last three thousand years of climate data indicate a gradual drying trend (Nyberg, Malmgren, Kuijpers, & Winter, 2002; Winter, Ishioroshi, Watanabe, Oba, & Christy, 2000). However, proxy records for this time are dominated by anthropogenic impacts (Bradbury, 1997; Huang et al., 2001; Islebe, Hooghiemstra, Brenner, Curtis, & Hodell, 1996; Peten et al., 1998)

5.3.2. Extreme weather events

Extreme weather from tropical storm systems and hurricanes are central components of the modern Caribbean climate and have massive impacts on ecosystems and on geomorphic processes. ENSO cycles drive the frequency and intensity of hurricanes (Tartaglione, Smith, & O'Brien, 2003). There is strong evidence that hurricanes have been more frequent and intense over the past 5 ky BP in correlation with ENSO activity during the mid-Holocene. (Donnelly & Woodruff, 2007; Woodruff, Donnelly, Mohrig, & Geyer, 2008). Numerical models of atmospheric circulation during the Last Glacial Maximum demonstrate that if hurricanes did form in the tropical Atlantic at that time, they would have been substantially less powerful than contemporary storms (Hobgood & Cerveny, 1988). Growth structures of Pleistocene age coral reefs in the Caribbean indicate minimal impacts by major storms (Giry et al., 2012; Meyer, Bries, Greenstein, & Debrot, 2003). Individual hurricane landfalls recorded in lagoon deposits on Vieques Island, ~30 km southeast of the Fajardo delta, share the same temporal pattern.

Soil salinization is a major impact of hurricane landfalls, and has been documented in the Luquillo Mountains and adjacent coastal plain areas following hurricanes (Gardner et al., 1992; Jean Lodge & McDowell, 1991). Our measurements of soil geochemistry show a major spike in salinization during the past 5 ky (Figure 17). The relative increase we observe in salt deposition could be related to an increased frequency of storm surges and salt water delivered in tropical storms.

5.3.3. Anthropogenic activity

Anthropogenic land-use also restructures ecosystems and alters geomorphic processes. There are many examples of impactful land cover change by pre-colonial peoples in the Caribbean region (Burney et al., 1994; Koch, Brierley, Maslin, & Lewis, 2019; Peten et al., 1998). Puerto

Rico may have been occupied as early as 5.5 ky BP (Burney et al., 1994) by people already possessing sophisticated social and technological adaptations (Hofman, Bright, & Ramos, 2010; Pestle, Curet, Ramos, & López, 2013). Archaeological evidence suggests that pre-colonial populations used fire for land clearance and planted crops including maize, sweet potato, and beans (Pagán-Jiménez, Rodríguez-Ramos, Reid, van den Bel, & Hofman, 2015; Ramos, Jiménez, Santiago-Blay, Lambert, & Craig, 2013). There are no known archaeological excavations within the floodplain area, but petroglyphs exist in the nearby Rio Blanco watershed and are attributed to the Taino people (Scatena, 1989), who inhabited Puerto Rico at the time of European colonization.

Historic land use has completely restructured the terrestrial landscape of the Rio Fajardo watershed. Sugar cane cultivation began in 1498, and an aerial photographic survey shows that the region was intensely developed as agricultural fields or pastures in 1936 (Thomlinson, Serrano, Lopez, Aide, & Zimmerman, 1996). In the 1950's agricultural land use declined, and by 1988 a repeat aerial survey found the majority of the landscape had been reforested (Thomlinson et al., 1996). Reforestation has been dominated by invasive trees (Lugo & Helmer, 2004). Mining in the Luquillo Mountains occurred between the 14th and 19th centuries and kilns for industrial and personal charcoal production were constructed (Scatena, 1989). Today, a gravel mine in the watershed upstream of the sampling location has enhanced river incision for approximately the last decade (personal communication), exposing the floodplain stratigraphic section sampled in this study.

5.4. **Archives of ecogeomorphic change**

How sensitive are environmental systems to external perturbation? The 26 ky Fajardo floodplain record demonstrates that terrestrial systems respond in concert with external perturbations (Figure 20). In the earliest part of the record, between 26-22 ky ago, the two proxies

show low magnitude variability that could reflect climatic excursions (e.g. Heinrich event II) (Arienzo et al., 2015) or be caused by stochasticity in the collection, transport, and retention of eroded material in fluvial and floodplain systems. Over the remainder of the Pleistocene both records have extremely little variability. Erosion rates are well below the modern rates, averaging 50 mm/ky. The δ^{13}C of organic material is within the range of the modern forest biomass. At the end of the Pleistocene, trends in the two records begin to diverge. The δ^{13}C record starts shifting gradually towards the heavier carbon isotope and shows greater changes between sampled horizons. The simultaneous record of erosion rates increases modestly and stabilizes. Quiescence and gradual change are replaced in both records by dynamic fluctuations ~4.4 ky ago. Erosion rates more than double, peak ~500 years ago, and remain high into the present. The δ^{13}C record begins to change sharply between sampling horizons, becoming lighter (more like the Tabanuco forest) then dramatically heavier (dominated by grasses and wetlands). The heaviest values in record were deposited approximately 500 years BP, coincident with the peak in erosion. Both proxies become increasingly distinct from their prior norms, suggesting that external perturbations became more powerful in the late Holocene.

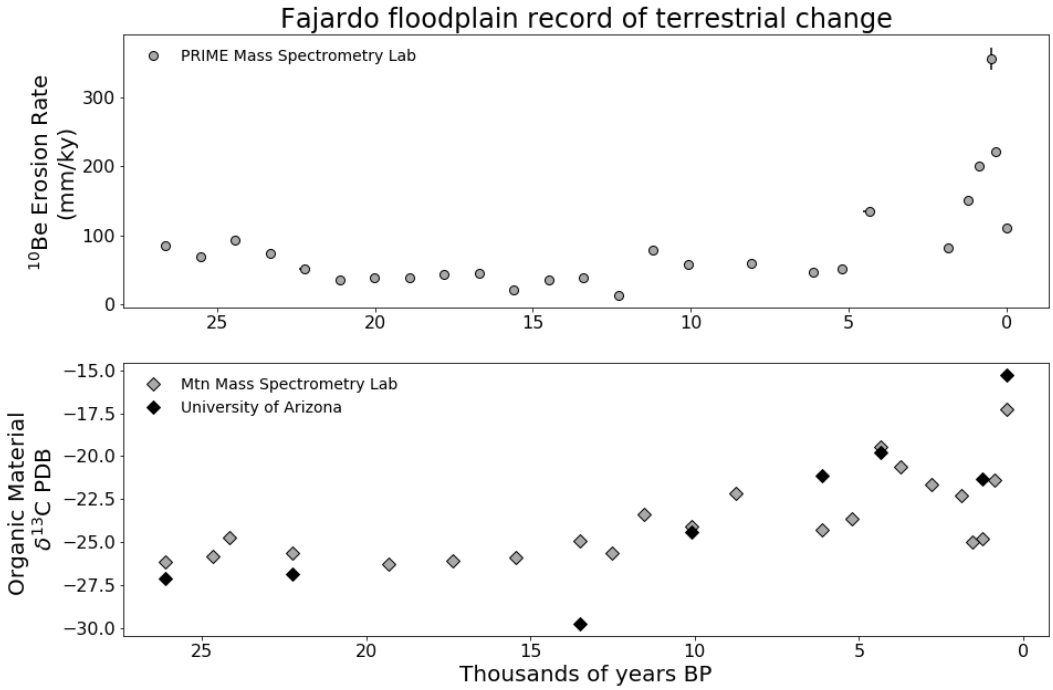

Figure 20 - Age calibrated measurements of paleoerosion rates (top) derived from $^{10}Be_{met}$ concentrations and $\boldsymbol{\delta}^{13}C$ ratios of organic material (bottom) retrieved from the sedimentary record of the Rio Fajardo floodplain.

5.5. **Sensitivity of environmental processes**

5.5.1. Geomorphology

Using the chronology of changing climate and trends in the $^{10}Be_{met}$ erosion proxy record, we consider the Fajardo floodplain archive in four timeframes: the mid-Pleistocene, late-Pleistocene, early-Holocene, and mid-Holocene to the present day (Table 6). We draw a distinction between the mid and late Pleistocene because of a significant decrease in the average erosion rates, from 75±1 mm/ky to 37±1 mm/ky. This may be a representation of precipitation trends driven by global climate cycles. Over the Quaternary, cyclic glacial stadials and interstadials have been identified from the changing $\delta^{18}O$ of foraminifera. The transition from an interstadial phase (marine isotope stage 3) to a stadial phase (marine isotope stage 2) occurs just prior to decreasing erosion rates in the Fajardo watershed (Lisiecki & Raymo, 2005). Low erosion rates persist until

the end of the Last Glacial Maximum and the start of the Holocene, when the erosion rate and variability in the record start to increase. The mid-Holocene to present day is distinct in both magnitude and variability, which we posit is evidence of changing external perturbations Scatena et al., 2012).

Table 6. Erosion rate changes over the Fajardo floodplain stratigraphic record

Time frame*	Date range	Average ε	Coefficient of variance	Maximum change**
	ky BP	mm/ky		mm/ky
Mid-Holocene to present	0 - 4.4	180±5	47%	155
Early-Holocene	5 - 12.3	51±1	38%	-65
Late-Pleistocene	13 - 21	37±1	18%	23
Mid-Pleistocene	22 - 26.6	75±1	19%	24

*Timeframes are delineated according to the radiocarbon ages of sampling horizons

**Greatest difference in calculated erosion rate between sampling horizons

Until the mid-Holocene, erosion rates change modestly in a manner that tracks the general trend of regional climatic conditions. This trend is explained mechanistically by the link between river discharge and sediment transport capacity (e.g. DiBiase & Whipple, 2011). Positive correlations between precipitation and long-term erosion rates have been documented in landscapes that are in steady-state with respect to rock uplift (Ferrier et al., 2013; Reiners, Ehlers, Mitchell, & Montgomery, 2003). Bedrock weathering and the production of mobile regolith also depends on rates of mean annual precipitation (Dixon, Heimsath, Kaste, et al., 2009; Owen et al., 2011). However, research compiling multiple study areas finds no dependence of denudation on mean annual temperatures or precipitation (Riebe, Kirchner, & Finkel, 2004; von Blanckenburg,

2005). In the context of this single watershed, bedrock composition and fracture density are constants, and steady-state rock uplift is indicated by the watershed geomorphology (Pike et al., 2010) and geochemical tracers of surface lowering (Anthony Dosseto et al., 2012). Therefore, climate is the clearest driver of changes in the paleoerosion archive. While erosion in the Rio Fajardo is apparently responsive to climate change, there are no abrupt changes during short-term climate excursions (e.g. Heinrich or Dansgaard/Oeschger events) as appear in proxies that relate directly to climate (Arienzo et al., 2017).

In the most recent 5 ky of the Fajardo floodplain the average erosion rate is more than double any time in the past. Overall variability and change between sampled horizons are much greater. Temporally, this behaviour aligns with the onset of ENSO-driven hurricanes as a disturbance regime (Donnelly & Woodruff, 2007; Woodruff et al., 2008). High precipitation during extreme weather increases slopewash and surface erosion (Larsen et al., 1999) and is key to triggering landslides. Mass wasting events occur when thresholds in soil pore-pressure are exceeded, which is directly linked to the intensity and duration of rainfall (Larsen, & Simon, 1993). Well documented impacts of modern hurricanes provide a valuable insight into the dependence of long-term erosion rates on hurricane landfalls. Larsen & Sanchez (1992) document more than 400 landslides triggered in the Luquillo Mountains by Hurricane Hugo in 1989. In the Rio Fajardo watershed, the landsides density was 10 per km^2 after this hurricane. The authors determine a recurrence interval for long-duration/high-intensity storms using historic precipitation data and calculate a storm-triggered average erosion rate of 164 mm/ky for the Luquillo Mountains (Larsen & Torres Sanchez, 1992; Larsen & Torres-Sanchez, 1998). This value is extremely close to the 180 mm/ky average since the mid-Holocene indicated by the $^{10}Be_{met}$ proxy record. Erosion rates dependent on landslide frequency and a hurricane-driven disturbance regime agrees with the

results of geomorphic studies in the Luquillo Mountains that use other methodologies (Brown et al., 1995; Larsen et al., 1999; Stallard, 2012).

The extremely high erosion rate of 356±16 mm/ky during approximately 500 years BP is most likely caused by land use practices within the watershed. Erosion rates from agricultural fields globally are 1-2 orders of magnitude higher than erosion under native vegetation and measured by long-term proxies (Montgomery, 2007). Intensive agricultural and pastoral land use likely drove watershed erosion rates well above the pre-colonial level (Scatena, 1989). Recent reforestation in the watershed, likewise, may have contributed to the subsequent lowering of erosion rates (Aide, Zimmerman, Herrera, Rosario, & Serrano, 1995; Aide, Zimmerman, Pascarella, Rivera, & Marcano-Vega, 2000; Aide, Zimmerman, Rosario, & Marcano-Vega, 1996).

5.5.2. Ecology

The δ^{13}C of sedimentary organic matter has an overall tendency towards ^{13}C-enrichment and specific trends that delineate behavioural patterns within time frames (Table 7). We do not distinguish between the mid- and late-Pleistocene for these samples, because the mean and standard deviation of the sample populations do not change between those intervals. Pleistocene-age δ^{13}C values are constant over time, recording no changes in the ratio between C_3 and C_4 plants over this interval. The average δ^{13}C for the Pleistocene (-26.28 $^{o}/_{oo}$) suggests little biomass derived from C_4 plants. The δ^{13}C distribution is extremely tight if we remove one outlier (-29.72$^{o}/_{oo}$) giving an average δ^{13}C of -25.94$^{o}/_{oo}$, a standard deviation of 0.7 $^{o}/_{oo,}$ and a 3% coefficient of variance. Difference between sample intervals in the Pleistocene (excepting the outlier) is <1.1 $^{o}/_{oo}$, less than the differences measured between the δ^{13}C of leaf, wood, and root tissues from the same plant (Heaton, 1999).

In the early-Holocene the $\delta^{13}C$ of sedimentary organic carbon is progressively enriched in ^{13}C. The average $\delta^{13}C$ is heavier than the Pleistocene and lighter than the mid-Holocene to present. The standard deviation and coefficient of variance are similar to Pleistocene values, signifying a period of gradual, progressive change within the watershed. In the early-Holocene the greatest difference between sampled horizons is 2.2 $^{o}/_{oo}$ and the average difference between samples is 0.2 $^{o}/_{oo}$. The change from sample to sample is small enough to be caused by photosynthetic differences, rather than the introduction of new plant types in the watershed. However, for the 12 ky of the early-Holocene, the measured $\delta^{13}C$ is enriched from -25.6 to -21.14 $^{o}/_{oo}$ indicating the presence of C_4 plants in the ecosystem.

We differentiate between patterns in the early- and mid-Holocene, before and after 5 ky BP. The transition between these two time-frames is marked by the single largest $\delta^{13}C$ difference between sampling horizons (+4.16 $^{o}/_{oo}$). The mid-Holocene to present is a dynamic period exhibiting two distinct trends. First, a steep and rapid decline in $\delta^{13}C$ values between sampling horizons from a high value of -19.47 $^{o}/_{oo}$ at ~4.4 ky BP to a low value of -24.9$^{o}/_{oo}$ at 1.25 ky BP. The trend towards ^{13}C-depleted $\delta^{13}C$ ratios reverses course ~1 ky BP, which could reflect reduced precipitation during the Little Ice Age (Haug et al., 2011). $\delta^{13}C$ ratios spike to -15.29$^{o}/_{oo}$ in the most recent sample radiocarbon dated to ~500 years BP. The difference between the samples dated at 872- and 504-years BP is +4.12$^{o}/_{oo}$ - the second largest change between sampled horizons in the entire record. This change should be attributed to the introduction of agriculture and the expansion of grasses in the watershed by anthropogenic practices. With exception to this sample, the $\delta^{13}C$ values for the mid-Holocene are have the same range of $\delta^{13}C$ values as the early Holocene, reflecting an ecosystem composed of a mixture of C_3 and C_4 vegetation types. However, the rate of change in ecosystem composition is accelerated.

Table 7. Ecological changes over the Fajardo floodplain stratigraphic record

Time Frame	Date range	Average	Standard deviation	Coefficient of variance	Minimum	Maximum
	ky BP	δ^{13}C	$^{o}/_{oo}$		δ^{13}C	δ^{13}C
Mid-Holocene to present	0 - 4.4	-20.8	2.74	13%	-24.97	-15.29
Early Holocene	5 - 12.5	-23.58	1.30	6%	-25.6	-21.14
Pleistocene	13 - 26	-26.28	1.27	5%	-29.72	-24.75
Holocene*	12.5 - 0.5	-22.64	1.84	8%	-25.6	-19.47
Pleistocene**	13 - 26	-25.94	0.7	3%	-27.1	-24.8

*Holocene values as a whole, with the samples influenced by humans removed as outliers

**Pleistocene values considered with the minimum removed as an outlier

Quiescence in the Pleistocene replaced by the trends of the Holocene indicates that climate change favoured the encroachment of tropical grasses, sedges, and wetland plants. C_4 plants are more efficient with respect to light and water and are advantaged when conditions become arid (Schulze, Ellis, Schulze, Trimborn, & Ziegler, 1996). However, if moisture is not a limiting factor, C_4 plants are favoured by a warming climate (Collatz, Berry, & Clark, 1998) suggesting that insolation changes were significant exiting the last glacial stadial. From 5 ky BP to ~1.2 ky BP the Fajardo floodplain indicates a shift favouring the abundance of C_3 type plants that may be driven by Holocene climate fluctuations. Cooling temperatures at the end of the Holocene Thermal Maximum (~10-5 ky BP) are inferred from the Caricao Basin sediments (Haug et al., 2011). Increased precipitation is recorded in a speleothem from central Puerto Rico (Rivera-Collazo et al., 2015) and pollen assemblage in Lake Valencia, Venezuela, ~2° east and ~8° south of Rio Fajardo (Bradbury et al., 1981; Leyden, 2009).

The onset of intense ENSO activity, and with it, increasing frequency and magnitude of disturbance also alters the ecosystem (Brokaw & Grear, 1991), and affects the quantity and quality of carbon in fluvial transport (McDowell & Asbury, 1994; Wohl & Ogden, 2013). Catastrophic events impact above ground biomass, successional growth patterns, litter fall/decomposition, and nutrient cycling. These processes before and after major storms have been quantified in the Luquillo Experimental Forest (Scatena, Moya, Estrada, & Chinea, 1996; Silver, Hall, & González, 2014; Zimmerman et al., 1995; Zimmerman et al., 2014). Hurricane Hugo reduced above ground biomass and nutrient pools of N, P, K, Ca, and Mg by ~50% and generated a pulse of litter ~400 times daily background inputs (Jean Lodge, Scatena, Asbury, & Sanchez, 1991). In the forest today, the recurrence interval of major disturbance events is shorter than the recovery time of biomass and soil nutrient pools (Lugo & Scatena, 1996). Massive growth pulses occur after hurricane events, however, the ecosystem does not attain steady state with respect to biomass or soil nutrients and always retains biomass volume below its support capacity (Sanford, Parton, Ojima, & Lodge, 1991; Scatena et al., 1996). Nutrient cycles and ecosystem structure in the Luquillo Mountains today are specifically adapted to a disturbance regime Lodge, McDowell, & McSwiney, 1994; Scatena et al., 2012).

In the wake of a hurricane, forest stand defoliation, breakage, and uprooting opens the canopy, creating niche sites that successional species occupy (Brokaw, 1998). Likewise, landslides open the canopy to successional growth (Taylor, Silander, Waide, & Pfeiffer, 1995). Ferns, palms, and woody shrubs are the dominant successional plants following hurricanes (e.g. *Cecroppia schreberiana*, *Guarea glabra*) (Brokaw, 1998; Lugo, Francis, & Frangi, 1998; Scatena et al., 1996). These trees have fast growth habits and rapidly consume nutrients deposited on the forest floor (Zimmerman et al., 1995). They close openings in the canopy quickly and prevent the

encroachment of grasses in the forest, as commonly occurs in other disturbed ecosystems (Brokaw & Grear, 1991). Considering the δ^{13}C pattern in the Fajardo floodplain record, it is plausible that the onset of a hurricane-driven disturbance ecology could cause the depletion of δ^{13}C ratios at this time. Hurricane defoliation is greatest on mountain slopes than in lowlands, subsequently increasing the delivery of forest litter and woody debris to the stream channel (Brokaw & Grear, 1991). The successional species are C_3-photosynthesizers, so their ecological abundance will create a similar trend in the δ^{13}C. In the recent history of land cover change in the Fajardo watershed, researchers observe the rapid colonization of abandoned pasture by pioneer trees (Lugo, 2004; Lugo & Helmer, 2004). Taking these abandoned agricultural plots as disturbance analogues, trees have a competitive advantage even in parts of the landscape that are suitable for the growth of tropical grasses.

Holocene age carbon retained in the Rio Fajardo floodplain has a natural range falling roughly between -25 and -18 $^{o}/_{oo}$ PDB. The values measured 500 years ago likely reflect the biomass of agricultural crops, especially sugar cane, and grasslands enhanced by clearing land for pasture. It is unclear whether humans influenced the ecological composition of the watershed prior to colonization. The human occupation of Puerto Rico probably began more than four thousand years BP (Burney et al., 1994) and the use of fire for land clearance and the cultivation of crops has been confirmed on the island as early as 3295 years BP (Pagán-Jiménez et al., 2015; Ramos et al., 2013). The expected impact of fire and/or agriculture on the bulk δ^{13}C ratios is an enrichment in ^{13}C. Within the time frame of pre-colonial occupation, two samples trend towards ^{13}C enrichment dated to 4342 and 872 years BP. Anthropogenic influence could most reasonably be invoked for the 872-year-old sample, which does reverse a clear trend in the δ^{13}C record. However, the δ^{13}C value of that sample (-21.39$^{o}/_{oo}$) is very close to the mean value of the Holocene δ^{13}C

distribution. It is hard to attribute these changes to human occupation without additional evidence of inhabitation of the watershed. Most pre-colonial settlements in Puerto Rico were established on the coast and relied on marine resources. The Luquillo Mountains were a sacred place and there are signs of ceremonial practice within the forest (Scatena, 1989). It is most likely that pre-colonial occupation did not significantly disrupt the ecosystem in the watershed.

5.6. Conclusions

Records of terrestrial change in the Rio Fajardo watershed confirm that the ecosystem composition and rates of geomorphic processes have changed in response to climatic forcing over the Quaternary period. Erosion rates track the trends in precipitation over time and tend to remain stable within timeframes. Vegetation dynamics reveal a shift in the abundance between C_3 and C_4 photosynthesizing plant groups that may be more strongly influenced by trends in temperature than in precipitation. Both systems appear to maintain a dynamic equilibrium with climate forcing through the Pleistocene-to-Holocene transition and during the first ~12 ky of the Holocene. Paleoclimate proxies suggest that approximately 5 ky BP changes in ENSO dynamics led to a climatic regime characterized by frequent, intense tropical storms in the Caribbean. Both systems apparently transition to a state of pulsed-response to disturbances at this time, evidenced by the degree of inter-sample variability and the overall magnitude of change. Contemporary studies suggest that perturbation-response characteristics explain the magnitude and rate of geomorphic processes and cycling of biomass and nutrient pools in the Luquillo Mountains. The greatest anomaly in both records is caused by post-colonial anthropogenic activity. This suggests that anthropogenic disruption of ecological and geomorphic systems can drive change that significantly exceeds the rate and magnitude of natural disturbance.

ACKNOWLEDGMENTS

Thanks to Dr. Isabel Rivera-Collazo at Scripps Institution of Oceanography and Dr. Todd Lange at the University of Arizona AMS Lab. Thanks are due as well to the LCZO community and to our friends in Naguabo, Puerto Rico. This research was supported by NSF grants 1651243 and 1331841 awarded to Dr. Jane K. Willenbring.

Chapter three has been prepared for submission to the journal Quaternary Science Reviews and may appear as: Harrison, E. J., Brocard, G. Y. and Willenbring, J. K., Quaternary record of terrestrial environmental change in response to climatic forcing and anthropogenic perturbations. *Quaternary Science Reviews.* (2020). The dissertation author was the primary investigator and author of this paper.

CHAPTER 4

GLOBAL RATES OF SOIL PRODUCTION INDEPENDENT OF SOIL DEPTH

Emma J. Harrison[1] • Jane K. Willenbring[1] • Gilles Y. Brocard[2]

[1] Scripps Institution of Oceanography, University of California San Diego, La Jolla, CA, USA.

[2] Institut des Sciences de la Terre, Observatoire des Sciences de l'Univers, University of Grenoble, France

ABSTRACT

Accelerated rates of soil erosion threaten the stability of ecosystems (Verheijen, Jones, Rickson, & Smith, 2009), nutrient cycles (Cease et al., 2012), and global food supplies (Montgomery, 2007) *if* the processes that produce soil cannot keep pace. Over millennial timescales, the rate of soil production is thought to keep pace with the rate of surface erosion through negative feedbacks between soil thickness and the rate at which soil is produced from the underlying mineral substrate. This paradigm in the Earth Sciences holds that an unknown underlying mechanism lowers the rate of soil production when soil is thick and increases the rate of soil production when soils are thin. This dynamic balance lends support to two observations: First, soil covers >90% of Earth's ice-free surface (NRCS) despite global erosion rates that vary by three orders of magnitude (Montgomery, 2007) and second, the thickness of soils on Earth exists within a relatively narrow range even in old and deeply weathered landscapes (Dixon & Riebe, 2014). However, the actual coupling mechanism between soil thickness and depth is unknown, and the functional form of the relationship is debated. Here, we question whether this balance exists and whether the apparent negative feedback instead arises from a computational

artefact of how soil production rates are calculated in landscapes with changing erosion rates. As evidence, we compared sites that have likely experienced constant erosion rates and climate over geologic timescales with sites that may experience transient erosion responses to environmental change in a global compilation of soil production versus soil thickness. We conclude that soil production resists self-arresting behaviour in some locations and is uniformly slow in arid and semi-arid settings - independent of soil depth. This result has drastic consequences for soil sustainability in the context of anthropogenically accelerated soil erosion such that an acceleration in modern erosion may not give rise to a concomitant, matched rise in soil production.

1. MAIN

The coupling between the depth of the soil mantle and the rate of soil production was first recognized by Gilbert in 1877 and was used in models of hillslope evolution years later (Carsen & Kirkby, 1972). Under this conceptual framework, soil production is a self-arresting process where rates are enhanced as bedrock comes closer to the surface and dampened as soil cover thickens. Here and in the references therein, "soil" is considered to mobile regolith. Powerful empirical evidence and a new geochemical methodology for measuring soil production rates was introduced by Heimsath el al.(Heimsath et al. 1997) whose results seemed to confirm the earlier hypothesis that soil production rates depend on soil thickness exponentially. The exponential form of this relationship, popularly named the soil production function (Heimsath et al. 1997), is frequently used to generate quantitative models of landscape evolution and soil formation and transport as well as fluxes of chemical weathering products. The soil production function contains two important theoretical predictions: self-arresting behaviour that causes soil production to effectively cease at a terminal soil thickness, and the existence of a maximum soil production rate governed by local climatic and lithologic conditions. Erosion rates exceeding the maximum soil production

rate result in increasing bedrock exposure (Dietrich et al., 1995) and diminished holding capacity for nutrients, carbon, and water across landscapes.

Over the past two-decades the dataset of empirical soil production rates has grown to represent the spectrum of topographies, climates, and ecosystems on Earth. This global dataset contains a population of study areas where the data appears to support an exponential soil production function (Heimsath, Chappell, Dietrich, Nishiizumi, & Finkel, 2000; Heimsath, Chappell, Dietrich, Nishiizumi, & Finkel, 2001; Heimsath, DiBiase, & Whipple, 2012; Heimsath et al., 1997; Heimsath, Furbish, & Dietrich, 2005; Larsen et al., 2014; Owen et al., 2011; Smith, Chandler, & Rose, 2009; Suresh, Dosseto, Hesse, & Handley, 2013) and another population of sites where it does not (Byun, Heimsath, Seong, & Lee, 2015; Dixon, Heimsath, & Amundson, 2009; Ferrier, Kirchner, & Finkel, 2011; Heimsath, Chadwick, Roering, & Levick, 2019; Owen et al., 2011; Riggins, Anderson, Anderson, & Tye, 2011; Wilkinson et al., 2005) (Figure 21). Prompted by the number of studies finding no soil production function and a new collection of a similar dataset from a tropical mountain range in Puerto Rico (Appendix B Table 12), we endeavoured to identify the common thread between sites defying the paradigm of depth-dependent soil production. However, the two populations are indistinguishable based on the soil forming factors (Jenny, 1994), extremes in aridity (Amundson, Heimsath, Owen, Yoo, & Dietrich, 2015), plant decomposition, or dust deposition rates. The behavioural difference cannot be explained by the position of the water table, hillslope gradients or propagation of the chemical weathering front. Ultimately, we propose that the difference is not caused by the landscape properties that control soil production, but instead by an artefact of the method used to measure soil production rates.

Soil production rates are measured by collecting a sample of material below the base of the soil mantle and measuring the concentration of the cosmogenic radionuclide ^{10}Be it contains (Dunai, 2010; Gosse & Phillips, 2001). ^{10}Be is produced within the mineral lattice of quartz at a rate that is a function of that sample's position on Earth and its depth below the surface (Lal, 1991). Mass removed from above the sample by chemical and physical erosion increases the ^{10}Be production rate because the energy catalysing the spallation reaction is attenuated as it passes through Earth materials. The ^{10}Be production rate for any sample is an exponential function depending on the bulk density of the overburden and the sampling depth. Therefore, for these measurements to be accurate, the sample depth must have remained constant over the time period of ^{10}Be accumulation (Heimsath et al., 1997). As such, authors have attempted to constrain these studies to areas that are in geomorphic steady-state, defined as a condition in which landscape uplift rate is equal to landscape lowering and erosion rates are constant throughout space. Evidence establishing this condition is typically gained by comparing landscape-scale rate measurements and allowing for variation to exist at finer spatial scales. In fact, gradient-controlled erosion across space predicts soil depth will vary as a function of hillslope curvature (Dietrich et al., 1995) and is the theoretical framework for the pioneering work by Heimsath et al. (1997).

Here, we present a model demonstrating that spatially variant rates of landscape lowering can produce a spurious exponential fit between soil production rates measured from ^{10}Be nuclide concentrations and soil depth measurements. We recast the studied landscapes as "transient" or "equilibrium" landscapes based on the likelihood that surface is lowering at spatially constant rates. All the study areas compiled in Figure 21 are upland erosional landscapes with hillslope gradients sufficient to transport sediment downslope. However, sites listed in panel B are topographic settings that are less likely to have spatially variant rates of hillslope processes. The

sites in South Korea and the Blue Mountains of Australia are plateaus, the sites in the Sierra Nevada of California (Dixon, Heimsath, & Amundson, 2009) and Luquillo Mountains of Puerto Rico are disconnected from the local base level (Brocard et al., 2016), the hillslope studied in Bodmin Moor, U.K. is a low-gradient parabola (Riggins et al., 2011), and the hyper-arid Atacama (Owen et al., 2011) and South African (Heimsath et al., 2019) sites have been tectonically and climatically stable for tens of thousands of years. In a study of semi-arid sites in the Chilean Atacama, the authors present data from a hillslope actively dissected by rill erosion, which conforms to the soil production function, and data from a stable hillslope that does not (Owen et al., 2011). Another sites included amongst the equilibrium population is a steep, rapidly eroding alpine setting (Ferrier et al., 2011) where spatially constant erosion is not likely. In this study, the authors collected samples for analysis at a constant depth. Their results, which do not find soil production rates dependent on soil depth, follow the functional mode of equilibrium landscapes where soil production may vary randomly around a place-specific mean rate.

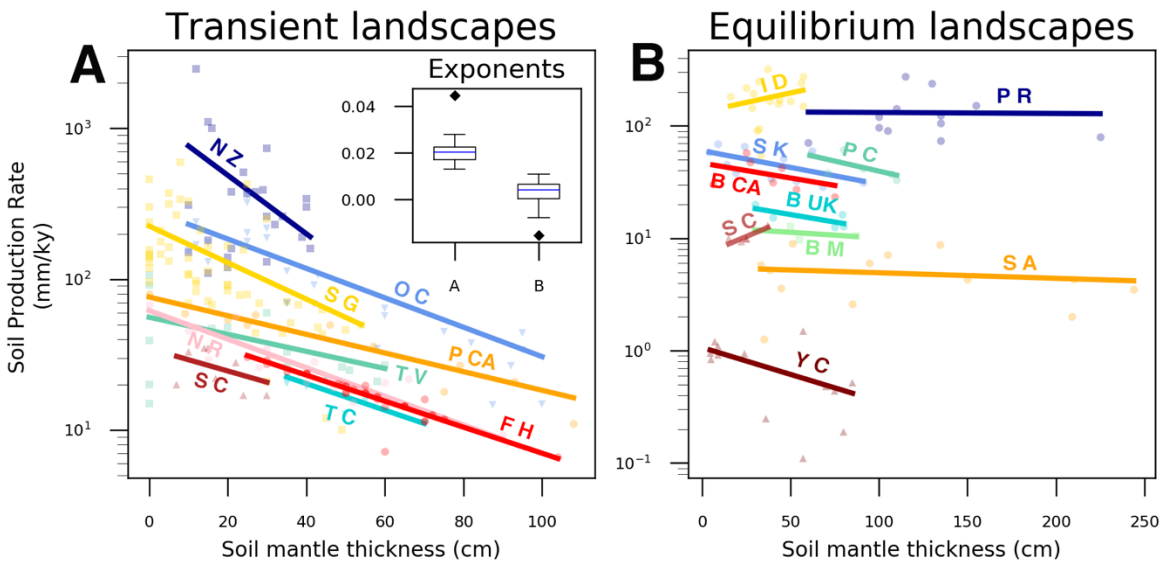

Figure 21 - Compilation of soil production functions from published literature. Global compilation of measurements comparing soil mantle thickness and soil production rates. Markers indicate point measurement data and have shapes corresponding to the dominant lithology in the study area. Circles are granite/diorite lithologies, upside-down triangles represent sandstone, triangles are mixed plutonic and volcanic rocks, and squares represents greywacke/schists. The colours grade from dark reds to blues representing the gradient in average annual precipitation between the sites. Fitted lines represent the best exponential fit to the dataset found with least squares regression. The exponent values for the fit lines in panels 1A and 1B are presented in the box plot inset in 1A. Study areas in 1A are as follows, N Z: Southern Alps, New Zealand; O C: Oregon Coast Range, Coos Bay OR; S G: San Gabriel Mountains, CA; P CA: Point Reyes, CA; T V : Tennessee Valley, CA; N R: Nunnock River, Bega Valley, Australia; F H: Frogs Hollow, Australia; T C: Tin Camp Creek, Australia; S C: La Serena, Chile. Study areas in 1B are as follows, I D: Idaho Batholith, Salmon, ID; P R: Luquillo Mountains, Puerto Rico; P C: Province Creek, Sierra Nevada, CA; S K: Daegwanryeong Plateau, South Korea; B CA: Blasingame, Sierra Nevada, CA; B UK: Bodmin Moor, UK; S C: La Serena, Chile; B M: Blue Mountains, Australia; S A: Kruger National Park, South Africa; Y C: Yungay, Chile. Map in Supplementary Material.

The transient landscapes grouped in Figure 21 panel A are uplifting sites with hillslope forms suggesting active connection to a locally incising baselevel. Two areas, the San Gabriel Mountains in California (Heimsath et al., 2012) and the Southern Alps in New Zealand (Larsen et al., 2014), are uplifting and eroding extremely rapidly and do not conform to the model of a geomorphic steady-state. The authors justify using measurements of ^{10}Be-derived to calculate soil production rates by 1) sampling only planar surface on ridge crests and 2) modelling the time required to "heal" ^{10}Be concentrations at depth following stochastic surficial erosion (Heimsath,

2006). The rest of these study areas share a similar topographic form: convex, soil mantled hillslopes with maximum curvature approaching the angle of material repose (Heimsath et al., 1997, 2005; Smith et al., 2009; Suresh et al., 2013). Numerical simulations of material transport laws predict the emergence of this specific land surface form in geomorphic steady-state (Hurst et al., 2013). These transport laws require the net conservation of mass but not uniform surface lowering in space (Gilbert, 1909). Rather, the material transport laws that have the best agreement with natural data on physical erosion are those in which the rate of transport is a function of hillslope curvature (Roering et al., 1999) – and curvature necessarily varies across space to drive the erosion of surface material.

We present the results of a simple, synthetic model simulation (Figure 22) demonstrating that spatially variant erosion may produce an apparent soil production function in plots comparing soil mantle thickness and soil production rate, due to the way soil production rates are calculated from the accumulation of ^{10}Be nuclides (code available online). We begin with a simulation of an equilibrium soil mantle, defined as uniform soil thickness across a topographic gradient. We populate the soil mantle with ^{10}Be nuclides, following the physical laws that cause production rates to attenuate with depth and material bulk density (Gosse & Phillips, 2001; Lal, 1991). We fix the concentration of ^{10}Be nuclides present, thereby defining the concentration values used to calculate soil production rates from samples collected beneath the soil cover. We simulate two landscape lowering scenarios: one in which the surface lowering is spatially constant and another where the surface is lowered by a thickness that varies in space as a function of the hillslope curvature. We then calculate the soil production rates across the hillslope given the new parameters for soil thickness.

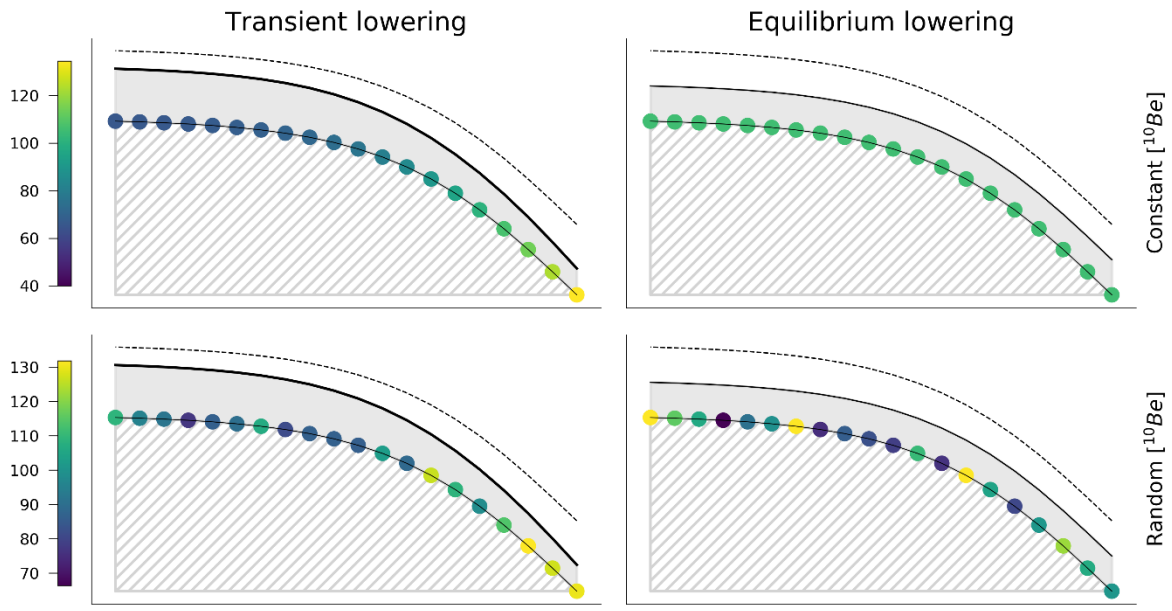

Figure 22 - Model simulations of apparent soil production rates under erosion scenarios. Results of a model simulating four scenarios of soil production measurements along a model hillslope. Upper left corner shows an initial condition of constant, equal ^{10}Be concentrations at the soil-bedrock interface and a surface lowering rate that is variable through space as a function of the hillslope profile curvature. Upper right corner shows an initial condition of constant, equal ^{10}Be concentrations at the soil-bedrock interface and a surface lowering rate that is constant through space. The bottom left and right corners show spatially variant and spatially constant surface lowering respectively, under the initial condition of random ^{10}Be concentrations at the soil-bedrock interface prior to erosion. The colour of the points along the profile indicate the apparent soil production rate at each point along the soil-bedrock interface. Colour bars are normalized to the initial ^{10}Be concentrations of for the model run.

We run the model from two different initial conditions. In the top panel, the initial ^{10}Be concentrations beneath the soil interface are all equal. In the bottom panel, we add random variance to the initial ^{10}Be concentrations prior to eroding the surface. In both simulations, equilibrium surface lowering results in soil production rates with no depth-dependence and transient lowering produces the appearance of depth-dependent soil production. This result arises because the observed depth of the sample is a key parameter input to determine the ^{10}Be production rate that is used to calculate the length of time required to accumulate the observed ^{10}Be concentration. Even when there is no evidence of transient erosion in time at the specific sample site (e.g. landslide scarring), unequal erosion across space can produce a false correlation between soil depth and soil production when the two variables are compared in a given landscape.

In the global compilation of landscapes with exponential soil production functions (Figure 21A), the functions fitting the data for each site have unique coefficient and exponent values. We find that varying the bulk density input parameter changes the exponent of the fit in our transient erosion model. This exponent value has been interpreted as a measure of the degree of coupling between the surface erosion and soil production. Rather, it is an artefact of the attenuation rate imposed in the calculation of ^{10}Be production rates with depth. Increasing the input value of soil bulk density causes linear growth in the exponent value of the apparent soil production function, shown in Figure 23 for the model simulations. Bulk density values reported in the literature range from 1.2 – 2.9 g cm^{-3}; varying this one parameter across the observed range produces many of the exponent values found in field studies. The second free parameter in the soil production function equation is a coefficient that accommodates the magnitude and variance of measured soil production rates in the dataset. Imposing a variety of external erosion rates while populating ^{10}Be concentrations in our model environment produces a range of fit coefficients that increase with the increasing magnitude of imposed erosion rates. By fixing this coefficient to a defined range of values (as a natural dataset of soil production rates would do) least-squares regression can produce the full range of exponent values published as soil production functions.

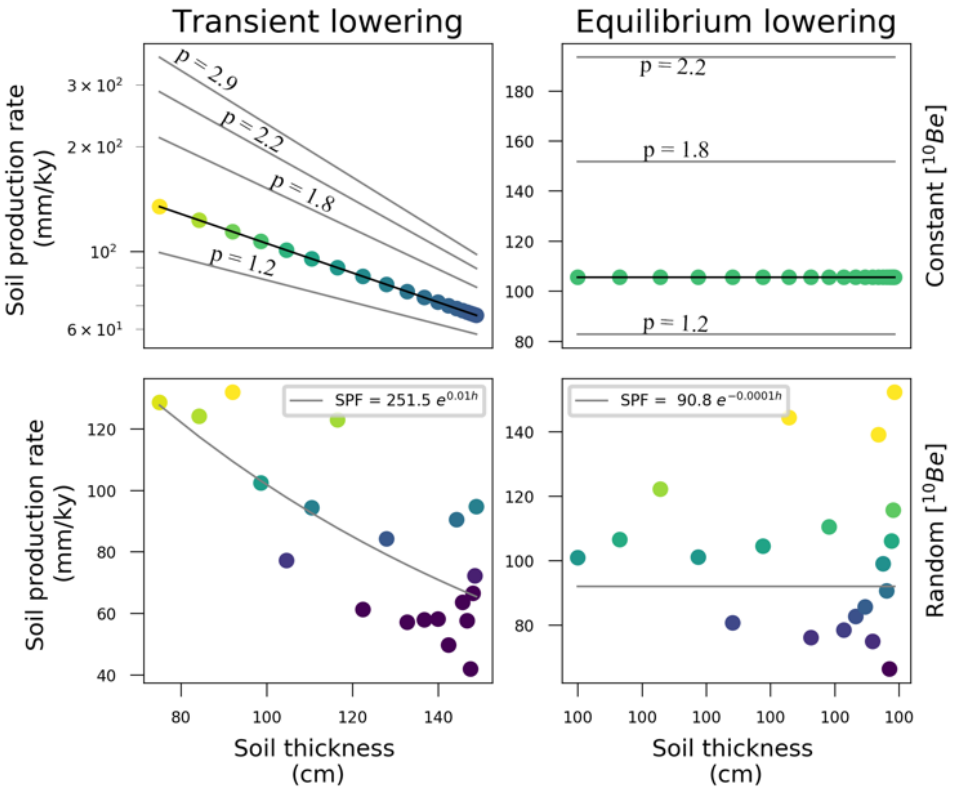

Figure 23 - Soil production functions for the four modelled scenarios. For each of the model outputs in Figure 22 we plot the soil production rates vs. soil depth in the corresponding panels in Figure 23. We fit the data to an exponential curve using a least squares regression analysis. For the bottom two panels showing the random-noise initial condition, the best fit equation is shown. For the top two panels showing the constant initial condition, we show the results of the exact same analysis but varying the bulk density input parameter used in the calculation of ^{10}Be production rate at depth and calculation of soil production rates from ^{10}Be concentrations. Bulk density input values are 1.2, 1.6, 1.8, 2.2, and 2.9 grams cm^{-3}

We conclude from this analysis that the prior measurements of an exponential soil production function is a computational artefact of the exponential decline of ^{10}Be production attenuated by depth and material density in landscapes where surface lowering rates vary across space. Clearly this implies that a decades-entrenched methodology for quantifying soil production rates is inappropriate and must be reimagined. Further implications of this work arise from the incorporation of these data and predictions arising from them in other analyses. Erroneous soil production rates are used to calculate the rate of flux of mass lost in solutes as weathering products (Dixon & Von Blanckenburg, 2012; Riebe, Kirchner, Granger, & Finkel, 2001) or mass gained

through the deposition of dust. Such fluxes inform calculations of the nutrient mass balance for many locations. As equilibrium landscapes provide no evidence for direct coupling between soil erosion and production, the result is a stark realization that anthropogenically accelerated erosion may not give rise to a concomitant, matched rise in soil production (Montgomery, 2007). Similarly, these data do not support the existence of a hypothesized maximum soil production rate (Dixon & Von Blanckenburg, 2012) or a negative feedback mechanism that arrests the mobilization of material at a certain depth, mechanisms that have informed modelling efforts with a range of intended applications (Furbish & Fagherazzi, 2001).

2. METHODS

2.1. Site Analysis

We examined the total number of studies publishing soil production rates and co-spatial soil depth measurements. We first differentiated between datasets conforming to an exponential soil production function (exponent value $\geq$ -0.01) from those that do not (exponent value <-0.01). Exponent values in most cases are included with the data in the original publications. For studies that do not quantify an exponential fit to their data, we ran a least squares regression on the soil production rates and soil depths using a computational approach detailed in the model description section of the methods in this manuscript.

We conducted an extensive literature review to compile site-specific value estimates for factors moderating either soil depth or soil production rate. For each study site, we identified as many of the following factors as possible: precipitation rate, average annual temperature and temperature extremes, vegetation type and percent cover, vegetation decomposition rates, bedrock lithologies, water table depth, chemical depletion of soil and saprolite relative to the bedrock, and

the average annual volume of dust deposition. These factors for each site and the references from which we obtain them are compiled in Appendix B. We used no statistical methods comparing the site factors, however none of the variables explain the split between the two populations. Other trends in the data, for example the mean soil production rate, vary systematically with climatic and geologic variables as has been described by other authors (Amundson et al., 2015).

To categorize the topographic setting at each site we use the primary author's site descriptions and photographs. Site descriptions identifying ridgelines as parabolic (constant curvature) we consider as likely to lower at a spatially constant rate, whereas convex, nonlinear ridgelines we consider as likely to lower at spatially variant rates. When available, we examined high resolution digital elevation models for the study areas and identified the point locations of the soil production samples. This allowed us to identify studies where field sampling targeted low-relief or hilly sections of the topography perched within a landscape that was elsewhere deeply incised and steeply convex. Such sections in a landscape have been described as "relict" topographies (Whipple et al., 2013), or locations in which hillslope gradients grade to an elevation higher than the local base level. Often, relict topographic sections are insulated from base-level lowering and relief driving processes acting on the broader landscape (Crosby & Whipple, 2006). Similarly, it is widely hypothesized that high relief plateaus are formed when a section of land is smoothed by geomorphic processes then subsequently uplifted and remains disconnected from the base level following uplift (Clark et al., 2005). We consider sites that are appeared to be disconnected from a locally lowering base level as more likely to be lowering at a spatially constant rate.

We also compared catchment-average denudation rates to point measurements of erosion on hillslopes. If the catchment average rates span the measured range of soil production rates, we

consider it evidence for spatially uniform surface lowering. If the catchment average denudation is higher than the soil production rates for a landscape, we consider it evidence for spatially variable surface lowering. Published values for catchment denudation are included in the site review of the Supplementary Information. For many of the studied locations, only one or few catchment averaged denudation rates are reported, or we were not able to identify which catchment contained the reported soil production sample. We include a figure in the Supplemental Information showing catchment-averaged denudation rates compared to the point measurements of soil production rates for five study areas, divided into "transient" and "equilibrium" landscapes as defined in the main text.

2.2. ^{10}Be derived soil production and measurements

Conventional methods for determining soil production rates in field studies were introduced by Heimsath et al. (Heimsath et al., 1997) and detailed descriptions of chemical extraction methods (Kohl & Nishiizumi, 1992) and calculations are available in review papers (Gosse & Phillips, 2001) and textbooks (Dunai, 2010). Simply put, a sample of Earth material is collected from below the base of the soil mantle, which is defined as the interface where material below retains the mineral fabric of the bedrock and the material above is disordered (Mudd & Yoo, 2010). The accumulation of *in situ* ^{10}Be contained in the samples is extracted chemically, purified, and measured with Accelerator Mass Spectrometry. The concentration (C) of ^{10}Be in atoms gram^{-1} is:

$$C_z = P_z * \left(\frac{1}{\lambda + \frac{\rho\epsilon}{\Lambda}}\right) \quad (1)$$

Soil production rates, or erosion rates, are calculated by convention using the online resource *CRONUS* (Balco et al., 2008). *CRONUS* computes a surficial ^{10}Be production rates from

the sampling latitude, longitude and elevation and user-defined scaling factor that accounts for the topographic or vegetative shielding at the site. Authors report scaling factors, surface production rates, and ^{10}Be concentrations along with soil production rates for reproducibility. Depth-dependent ^{10}Be production rates are derived in two ways: by including a depth-shielding factor as an input to *CRONUS* or by attenuating the surface production rate determined by the software for the sampling location. The ^{10}Be production rate at depth z (cm) is related to the surface production rate P_0 by:

$$P_z = P_0 e^{\frac{-z\rho}{\Lambda}} \quad (2)$$

Soil production rate is given by:

$$SP = \frac{\Lambda}{\rho}\left(\frac{P_z}{C_z}\right) \quad (3)$$

These are the three equations used in our model simulations and referenced in the model description below. Table 1 defines the variables, measurement units, and the assigned constant values we use in the model simulations.

Table 8. Variable descriptions and model input values for deriving soil production rates from ^{10}Be production rates and concentration measurements.

Variable	Variable description	Variable units	Model constants
C_z	^{10}Be concentration at depth	[atoms gram^{-1}]	Calculated
P_0	^{10}Be production rate at the surface	[atoms gram^{-1} year^{-1}]	7.0
P_z	^{10}Be production rate at depth	[atoms gram^{-1} year^{-1}]	Calculated
z	Depth below the surface	[cm]	Calculated
ρ	Bulk density	[grams cm^{-3}]	1.6
λ	^{10}Be decay constant ($ln2/t_{1/2}$)	[atoms year^{-1}]	0
ϵ	Surface erosion rate	[mm ky^{-1}]	40
Λ	Mean attenuation length	[cm^{-2}]	165

2.3. **Model description**

This model is written in Python 3.7. An annotated Jupyter notebook containing code to reproduce the model and figures in this manuscript is available online as part of the Supplementary Materials and in the corresponding author's GitHub repository.

First, a model hillslope was derived from the function for a sinusoidal curve. The function of this curve is given by:

$$y = \frac{1}{1+ e^{-x}} \tag{4}$$

where x is a linearly spaced array of 20 positive values. A second surface simulating a soil mantle was derived using the same curve function and adding an offset to simulate 200 cm of soil thickness.

Two erosional surfaces were generated. The first surface represents spatially constant erosion, where the thickness of the soil mantle is reduced to 100 cm but remains constant across the modelled hillslope profile. The second surface has a thickness that attenuates as a function of the curvature of the model profile, representing spatially variant surface lowering rates. Curvature at each point along the model profile is calculated as:

$$c(x) = \frac{|y^n|}{(1+y^{r2})^{3/2}} \quad (5)$$

where first and second derivatives are calculated using the python library autograd (Maclaurin, Duvenaud, Johnson, & Townsend) differation function grad. The curvature *k* at each point *x* is related to the sinusoidal hillslope profile as:

$$y_2 = -c^2 * f(x) \quad (6)$$

where *f(x)* is the equation for the hillslope surface. An initial vertical offset of 150 cm was imposed, and the height of y_2 above the soil-bedrock boundary layer changed along *x*.

At each point along *x* (n=20) we generated three numerical arrays containing values of the distance between the soil-bedrock interface and (1) the original surface (2) the constant erosional surface and (3) the variable erosion surface. These arrays are numerical representations of the depth to bedrock (or saprolite) along the profile under the different erosional scenarios and simulate pits that would be dug in a field study to collect samples for soil production rate calculations.

The concentration of ^{10}Be nuclides at the soil-saprolite boundary is calculated at each point along the profile using equation 1 from the prior methods. Equation inputs are the thickness of the pre-erosional surface under steady state conditions (*h*=200) and the output value from equation 2

for determining the ^{10}Be production rate at depth. For this simulation we impose as constant values an external erosion rate of 40 mm ky^{-1}, a soil bulk density of 1.6 g cm^{-3}, and a surface production rate of 7 atoms g^{-1} year^{-1} (see Methods Table 8). This concentration is stored as a fixed array and used in calculations for the steady-state model simulation. For the random-noise simulation, a random number generating function was used to produce an added noise value at each of the 20 points. The number generator created noise with a normal distribution around a mean of 0 with a standard deviation equal to 25% of the steady-state nuclide concentration.

We calculated ^{10}Be production rates at the soil-bedrock interface for each value representing the distance between the soil-bedrock boundary and the pre-erosional, constant erosion and variable erosion surfaces. ^{10}Be production rates and ^{10}Be concentrations from the steady-state and random noise simulation were used to calculate soil production rates following Equation 3 presented in the previous section. This results in five arrays of apparent soil production rates along *x*. For the pre-erosional surface, all the computed values are equal to the imposed external erosion rate value (40 for the model results in Figure 23). Steady-state and random-noise soil production values were calculated for the constant and variable erosional surfaces. These values are plotted as colours representing the range of calculated rates at point locations in the model hillslope profiles displayed in Figure 23 of this thesis.

A soil production function was added by performing a least squares regression on the data where the independent values are depths and the dependent values are the soil production rates simulated for each depth. Least squares regression is performed using the python library scipy.optimize (Virtanen, et al. 2019) function curve_fit. Curve_fit takes as an input the equation defining the form of the curve to be fit. This equation includes the number of free parameters that

may be constrained by the regression. For this exercise, we used a simple exponential equation having one coefficient and one exponent value:

$$y = a * x^k \quad (7)$$

Curve_fit returns the best fit parameters *a* and *k* for the xy value arrays. These parameters were used to define the soil production function for each of the model generated datasets, following the analytical convention of the published studies presented in Figure 21 of this manuscript.

We used an array of six bulk density values spanning the range used in published literature (1.2-2.9 g cm^{-3}) to calculate ^{10}Be concentrations and production rates for the pre-erosion surface and both erosional surfaces, following the procedures described here. For computational simplicity, this analysis was not performed for the random-noise condition. Least squares regression was performed using the same curve fitting function. The parameters for the coefficient and exponent of fit were used to plot the regression lines in Figure 23.

ACKNOWLEDGMENTS

This research was supported by NSF grants 1848637 and 1331841 awarded to Dr. Jane K. Willenbring.

Chapter four has been prepared for submission to the journal Nature and may appear as: Harrison, E. J., Brocard, G. Y. and Willenbring, J. K. Global rates of soil production independent of soil depth. *Nature*. (2020). The dissertation author was the primary investigator and author of this paper.

CHAPTER 5

CONCLUSIONS

1. RESEARCH OBJECTIVES AND CONCLUSIONS

The overall aim of this dissertation is to shed light on how climatic and tectonic perturbations are transmitted through geomorphic processes to alter functions in the critical zone. Each chapter follows this link through a different system in the Luquillo Mountains critical zone. In chapter two, we found that interactions between groundwater hydrology and the fluvial system are altered by tectonically-driven changes in critical zone architecture. We found that the groundwater table sets a local base level that drives fluvial incision in the relict topography, but that this process shuts off due to landscape adjustment downstream of the erosion front. In chapter three, we identified a state change in the coupling between the climate and the ecosystem composition and physical erosion in a watershed. We were able to further contrast the aspects of climate driving responses in the two terrestrial systems. In chapter four, we demonstrate that spatially variant rates of surface lowering led to the adoption of a paradigm in Earth Science that is not supported by the global data. Our reanalysis shows that soil production rates are likely not dynamically linked to the thickness of the overlaying soil.

2. RECOMMENDATIONS

We hope the work in this thesis will motivate further research and here we pose a series of recommendations for future pursuits.

2.1. **Water**

Future work to should assess the quantity of groundwater stored upstream/downstream of the erosion front and determine whether the groundwater residence time differs substantially across the watershed, which we predict following the results of our study. Short-lived radioactive isotope tracers, such as cosmogenic ^{22}Na (Kaste et al. 2016), and the isotopic ratios of dissolved ^{2}H and ^{18}O measured in the seep waters present useful approaches for identifying deep ground water circulation versus recent recharge in the aquifer.

A second direction for this research is to focus on interactions between the water table surface and the chemical weathering front. Geophysical methods such as ground penetrating radar, seismic surveys, or electromagnetic resistivity could be used to identify the depth of the chemical weathering front across the watershed. The groundwater table rises and falls beneath ridgelines, whereas the subsurface beneath floodplains is continually saturated. Contrasting the depth and structure of the chemical erosion front under these different topographic positions could elucidate the role of groundwater in the style and rate of chemical reactions.

2.2. **Ecosystems and erosion**

Floodplains exists adjacent to rivers worldwide and their stratigraphy records the watershed's paleo-erosion history. As geomorphic responses to climate change are still very much a subject of debate (Norton & Schlunegger, 2017; Willenbring & Jerolmack, 2015), we hope to see paleo-erosion records developed from floodplain stratigraphy in a range of environments with different paleoclimatic histories. Similarly, new studies that take the approach of tracking changes in physical erosion and ecosystems concomitantly could greatly increase our understanding of the feedbacks between plant communities and geomorphology. In marine sedimentary deposits, ^{10}Be/^{9}Be ratios have been used to constrain rates of physical and chemical erosion (Willenbring &

von Blanckenburg, 2010). Future work could focus on developing a methodology for analysing $^{10}Be/^{9}Be$ ratios in floodplains in addition to ^{10}Be concentrations.

2.3. Soils

New research aimed at identifying pedogenic processes that control the position of the soil-saprolite boundary should focus on mechanism that work at the base of the soil profile, rather than the surface. We believe that sub-critical granular creep, as has been isolated in laboratory experiments (Houssais, Ortiz, Durian, & Jerolmack, 2015), could explain the great depths of very old, very stable soils. Numerical modelling and comparisons to field data would be an appropriate approach to this problem. Accelerated rates of chemical weathering may occur as soil cover thins and explain the presence of soil in rapidly eroding landscapes. We recommend methods that explicitly target the timing of onset and extent of chemical weathering, such as uranium-series disequilibrium in depth profiles (Suresh et al., 2013).

3. CONTRIBUTIONS TO KNOWLEDGE

It is our hope that the research in this dissertation advances the disciplines of Critical Zone Science and Geomorphology. We contribute this in part through developing the ^{10}Be toolkit for Earth Science. Each chapter of this thesis presents an advance in the application of ^{10}Be by presenting a new empirical use, a novel application of ^{10}Be as a tracer, and the refinement of a widely-used ^{10}Be dating method. In chapter two, we generated a novel dataset with the first applied use of *in situ* ^{10}Be as a direct tracer of sapping incision by fluvial channels. In chapter three, we demonstrated the utility of meteoric ^{10}Be in a new landscape context. This work will make paleo-erosion studies possible in a considerable number of new locations thanks to the ubiquity of

floodplain deposits. In chapter four, we identified an inaccuracy in a popular ^{10}Be dating method and determined what conditions are required to apply this method correctly.

Chapter two of this thesis presents the first map of sapping channels in the Rio Blanco. The emergence of groundwater in seeps had not been previously studied in this landscape, despite the substantial groundwater contribution to river discharge (Shanley et al., 2011). Our analysis of spring properties above and below the erosion front revealed that topographic adjustment curbs sapping erosion through the exhumation of corestones. The presence of sapping erosion in the relict topography of the Rio Blanco is itself an advance in our understanding of the fluvial dynamics of groundwater–this process had only been demonstrated previously in settings where the substrate material is porous and homogenously-sized. Furthermore, we brought new empirical data to a fundamental question about the fluid mechanics of groundwater carving fluvial channels. The results of this study validate the theoretical prediction that transportation in groundwater carved channels is governed by parameters that are distinct from other fluvial networks.

Chapter three of this dissertation introduces a new historical record of terrestrial processes in the Rio Fajardo watershed. No similar long-term ecological records exist for the forest. This record shows the first arrival of tropical grasses in the watershed and shines light on the climate dynamics that increase their ecological, competitive advantage. Warming temperatures, more than precipitation trends, support tropical grasses at this site. Grasses are disadvantaged by the hurricane-driven disturbance regime that exists in the watershed today–which favours instead fast-growing shrubs and wetland plants. These coupling dynamics had not been identified by prior research. We create a new template for studying erosion and ecosystems simultaneously using a landscape context that generates cospatial records of both systems. Floodplains exists adjacent to rivers worldwide and their stratigraphy records the watershed's paleo-erosion history. Our work

in developing meteoric ^{10}Be as a tracer in floodplains has the potential to engender paleo-erosion studies in sites where this work was previously not possible.

Chapter four of this thesis demonstrates that a widely accepted paradigm in Earth Science is not supported by the global dataset. In our analysis, we demonstrate that there is not strong empirical evidence for coordination between rates of soil production and erosion. This work forces a shift in our intuitions about soil production processes: the action must be occurring at the soil-saprolite boundary rather than the soil surface.

APPENDIX A

Supplemental materials for Chapter 2

This appendix contains three data tables relevant to the analyses in Chapter 2: Dynamic Critical Zone architecture driven by subsurface flow in the Luquillo Mountains, Puerto Rico

Table 9. Measured discharges, drainage area, and erosion rates used in the model

Site ID	Drainage Area	Drainage Area	Type	Discharge	Norm*	Adjusted	Erosion rate	Erosion err
	m^2	km^2		$l\ s^{-1}$		$l\ s^{-1}$	$mm\ ky^{-1}$	$mm\ ky^{-1}$
IC-1	82450	0.0825	Spring	8.66	0.87	7.53	131	10
IC-2	27150	0.0272	Spring	0.68	0.87	0.59	85	7
SAB-3	16275	0.0163	Fluvial	0.87	1	0.87		
SAB-4	117275	0.117	Fluvial	3.6	1	3.6		
SAB-5	382975	0.383	Fluvial	7.9	1	7.9		
SAB-6	1596280	1.6	Fluvial	24.09	1	24.09		
SAB-7	127675	0.128	Fluvial	8.04	1	8.04		
SAB-14	9449.82	0.0095	Spring	0.94	1	0.94		
SAB-8	2609570	2.61	Fluvial	119	1	119.53		
IC-Gage	3367000	3.37	Fluvial	271	0.87	236.5		
CUY-18	2861	0.0029	Spring	0.05	1	0.05		
Sab-8	11495	0.0115	Spring				40	3
Sab-9	10079	0.0101	Spring				43	3
Sab-16	38882	0.0389	Spring				62	5
Cuy-UK	4012020	4.01	Fluvial				281	56
Pri-UK	3063690	3.06	Fluvial				87	12
IC-UK	3083650	3.08	Fluvial				100	16
Sab-UK	1909130	1.91	Fluvial				72	15
CC1	120000	0.12	Fluvial				69	5
EC1	10000	0.01	Fluvial				141	12

EC2	30000	0.03	Fluvial	150	12
IC0	130000	0.13	Fluvial	144	16
IC1	110000	0.11	Fluvial	172	15
IC2	110000	0.11	Fluvial	78	6
IC3	170000	0.17	Fluvial	153	12
IR1	20000	0.02	Fluvial	31	2
IR2	10000	0.01	Fluvial	31	2
IR3	60000	0.06	Fluvial	52	4
IR4	220000	0.22	Fluvial	142	10
SC1	240000	0.24	Fluvial	73	5
SC2	150000	0.15	Fluvial	85	7
SC3	4000	0.004	Fluvial	71	5
SR1	18790	0.03	Fluvial	15	1
m2	14310	0.0143	Spring		
m3	11387	0.0114	Spring		
m4	3166	0.0032	Spring		
m5	12976	0.013	Spring		
m6	10014	0.01	Spring		
1	4833	0.0048	Spring		
4	1769	0.0018	Spring		
12	9615	0.0096	Spring		
13	5655	0.0057	Spring		
19	4804	0.0048	Spring		
23	5210	0.0052	Spring		
25	4073	0.0041	Spring		
26	1593	0.0016	Spring		
29	995	0.001	Spring		
37	4438	0.0044	Spring		
40	951	0.001	Spring		
41	7407	0.0074	Spring		
57	2546	0.0026	Spring		
63	12546	0.0125	Spring		
68	3610	0.0036	Spring		
77	4254	0.0043	Spring		
85	3390	0.0034	Spring		
87	1391	0.0014	Spring		
94	1529	0.0015	Spring		
95	774	0.0008	Spring		
102	1533	0.0015	Spring		
110	3091	0.0031	Spring		
122	1362	0.0014	Spring		
130	1038	0.001	Spring		
138	1513	0.0015	Spring		
139	2051	0.0021	Spring		

140	869	0.0009	Spring
151	1752	0.0018	Spring
156	8305	0.0083	Spring
159	1880	0.0019	Spring
177	5536	0.0055	Spring
180	7448	0.0075	Spring
204	2698	0.0027	Spring
212	2046	0.0021	Spring
217	922	0.0009	Spring
218	5785	0.0058	Spring
222	2861	0.0029	Spring
226	7741	0.0077	Spring
228	1085	0.0011	Spring
233	3153	0.0032	Spring
238	1593	0.0016	Spring
247	4939	0.0049	Spring

Table 10. CRONUS inputs for deriving average erosion rates from ^{10}Be concentrations

Lat DD	Long DD	Elevation m	Thickness cm	Density g cm^{-3}	Shielding corr.	[10Be] atoms g^{-1}	Uncertainty atoms g^{-1}	std.
65.7884	18.2875	623	10	1.6	0.98	134982.9	4623.348	KNSTD
65.7884	18.28784	629	10	1.6	0.98	88491.23	1380.243	KNSTD
65.7971	18.2787	651	10	1.6	0.98	287066.6	5573.791	KNSTD
65.7962	18.2787	655	10	1.6	0.98	268924.4	4367.048	KNSTD
65.8029	18.2777	643	10	1.6	0.98	185315.3	3454.427	KNSTD

Table 11. Spring survey locations and geometric property measurements

Site	Long DD	Lat DD	Elevation m	Width m	Radius m	Aspect Ratio	Incision height m	Difference m
Sab	18.2776	-65.7957	653	11	2.9	3.793	680	28
Sab	18.2776	-65.7951	653	5.45	2.24	2.433	681	27
Sab	18.2764	-65.7948	653	9.6	3.65	2.63	670	17
Sab	18.2764	-65.7956	646	11.7	4	2.925	655	9
Sab	18.2764	-65.7958	642	14.7	3.7	3.973	653	11
Sab	18.2779	-65.7971	638	15.8	4.4	3.591	657	19
Sab	18.276	-65.7981	626	26.5	8.2	3.232	653	26
Sab	18.2769	-65.7974	634	30.5	12.5	2.44	659	24

Sab	18.2773	-65.7973	633	28.76	8.8	3.268	646	14
Sab	18.2777	-65.8	647	20.86	6.31	3.306	671	23
Sab	18.2771	-65.8018	649	14.5	4.8	3.021	684	35
Sab	18.2796	-65.7958	679	7.5	2.3	3.261	695	16
Sab	18.2791	-65.796	674	9.2	3.3	2.788	674	
Sab	18.2803	-65.7959	672	12	4.56	2.632	695	22
Sab	18.2813	-65.7977	663	7.8	2.48	3.145	676	13
Sab	18.282	-65.7971	670	5.62	1.74	3.23	680	10
Sab	18.2821	-65.7966	675	9.4	4	2.35	696	22
Sab	18.2839	-65.7965	671	17	5.1	3.333	685	14
Sab	18.2852	-65.7957	692	10.9	4.26	2.559	708	16
Sab	18.2849	-65.7967	676	6.4	2.5	2.56	687	11
Sab	18.2853	-65.7999	678	16	3.8	4.211	696	18
Sab	18.286	-65.7991	691	9.6	3.4	2.824	703	13
Sab	18.2858	-65.8002	683	8.5	2.97	2.862	695	12
Sab	18.2855	-65.8002	681	26.4	8.2	3.22	690	9
Sab	18.2846	-65.8021	678	18.6	6	3.1	697	19
Sab	18.2861	-65.8016	678	19.9	5.78	3.443	693	14
Sab	18.2853	-65.8025	688	14	4.8	2.917	712	25
Sab	18.285	-65.803	706	8.16	2.6	3.138	710	4
Sab	18.278	-65.8026	662	15.5	4.73	3.277	680	17
Sab	18.2782	-65.8029	660	9	2.6	3.462	690	30
Sab	18.2784	-65.8034	670	18.5	5.2	3.558	694	24
Sab	18.2814	-65.805	709	19.9	5.2	3.827	732	23
Sab	18.2799	-65.805	705	9.25	3.14	2.946	740	35
Sab	18.2864	-65.7982	686	12.64	3.57	3.541	710	24
Sab	18.2856	-65.7987	671	10.3	4.6	2.239	691	20
Sab	18.2866	-65.8001	703	18.4	5.2	3.538	717	15
Sab	18.2822	-65.8014	674	15	4.78	3.138	690	16
Sab	18.2834	-65.8022	682	8.36	3.42	2.444	695	13
Sab	18.284	-65.8051	725	12.8	4.2	3.048	730	5
Sab	18.2812	-65.8022	671	10.6	3.2	3.313	676	5
Icacos	18.2912	-65.7887	653	12.4	3.45	3.594	665	12
Icacos	18.2911	-65.7885	649	11.4	3.15	3.619	661	12
Icacos	18.291	-65.7892	641	16.2	6.4	2.531	648	7
Icacos	18.2914	-65.789	654	18.9	6.35	2.976	666	12
Icacos	18.2919	-65.7895	664	25.3	7	3.614	682	18
Icacos	18.2911	-65.7901	652	16.8	4.7	3.574	677	24
Icacos	18.2934	-65.789	706	14	4.6	3.043	722	17
Icacos	18.2923	-65.7895	674	14.4	3.9	3.692	682	8
Icacos	18.2899	-65.7894	651	5.6	2	2.8	665	14
Icacos	18.2897	-65.787	640	8	2.7	2.963	654	14
Icacos	18.2865	-65.7864	627	10.36	4.2	2.467	636	10

Icacos	18.288	-65.7872	632	14.28	4.3	3.321	651	19
Icacos	18.2888	-65.7867	628	8	2.15	3.721	636	8
Icacos	18.2884	-65.7886	631	90.8	32.3	2.811	654	23
Icacos	18.285	-65.7868	629	10.35	2.97	3.485	646	17
Icacos	18.2853	-65.7874	629	5.8	2.1	2.762	635	6
Icacos	18.2857	-65.7888	628	11.4	3.76	3.032	636	8
Icacos	18.2873	-65.7907	630	13.56	4.72	2.873	641	10
Icacos	18.2885	-65.7895	642	24.6	7.6	3.237	661	19
Icacos	18.286	-65.7855	639	35	12	2.917	651	12
Icacos	18.2816	-65.7835	636	23.6	7.43	3.176	656	20
Icacos	18.2824	-65.7852	648	7.9	2.7	2.926	676	27
Icacos	18.2824	-65.786	632	34.6	11.3	3.062	665	32
Icacos	18.2816	-65.7867	627	12	3.5	3.429	640	13
Icacos	18.2825	-65.7824	670	21.7	6	3.617	704	33
Icacos	18.282	-65.7821	660	9.86	3.17	3.11	677	17
Icacos	18.2824	-65.7821	669	13.56	3.78	3.587	676	7
Icacos	18.2844	-65.7823	680	13	4.3	3.023	689	9
Icacos	18.2859	-65.7844	653	68.2	22.6	3.018	682	29
Icacos	18.2763	-65.781	645	113.4	53.7	2.112	680	35
Icacos	18.2762	-65.7794	636	32	9.2	3.478	651	15
Icacos	18.2777	-65.7813	648	18.2	5.2	3.5	665	17
Icacos	18.2765	-65.7841	635	21.8	7.2	3.028	649	14
Icacos	18.277	-65.7869	626	7.8	2.2	3.545	643	17
Icacos	18.2789	-65.7851	629	8.9	3.17	2.808	640	11
Icacos	18.2726	-65.7824	641	29.6	9.8	3.02	663	22
Icacos	18.2725	-65.7817	665	10.3	2.6	3.962	684	19
Icacos	18.2754	-65.7837	632	7.8	2	3.9	650	18
Icacos	18.2756	-65.7781	647	34	11.6	2.931	664	18
Icacos	18.2696	-65.786	624	9.2	2.75	3.345	644	20
Cubuy	18.2771	-65.8129	746	7	2	3.5	786	40
Cubuy	18.2763	-65.8125	733	25.9	9.4	2.755	760	27
Cubuy	18.2761	-65.8133	745	11.7	2.8	4.179	779	34
Cubuy	18.2767	-65.8112	714	11.5	3.46	3.324	758	44
Cubuy	18.2725	-65.8099	667	17.2	5.98	2.876	680	13
Cubuy	18.2735	-65.8106	677	4.9	1.75	2.8	716	39
Cubuy	18.2747	-65.8094	677	21.79	6.78	3.214	698	21
Cubuy	18.2687	-65.8095	655	23.26	6.3	3.692	677	23
Cubuy	18.2685	-65.809	646	17	6.1	2.787	669	23
Cubuy	18.2688	-65.8085	634	9.8	3	3.267	657	23
Cubuy	18.2685	-65.8081	630	19.5	5.5	3.545	652	22
Cubuy	18.2693	-65.8101	660	10.2	2.9	3.517	670	11
Cubuy	18.271	-65.807	644	21.3	6.9	3.087	678	34
Cubuy	18.2671	-65.8078	618	9.3	3.7	2.514	627	10

Cubuy	18.2739	-65.8124	689	20	6	3.333	731	42
Cubuy	18.2746	-65.8135	736	36	9.9	3.636	765	29
Cubuy	18.2731	-65.8127	695	11.2	4	2.8	711	16
Cubuy	18.2733	-65.8129	706	12	3	4	716	10
Cubuy	18.273	-65.8148	659	32.6	15.635	2.085	679	20

APPENDIX B

Supplemental Materials for Chapter 4

Table 12. Soil production rate calculations for the Luquillo Mountains, Puerto Rico

Site ID	Lat	Long	Elev m	Density g cm^{-3}	Soil depth cm	Depth shield.	[10Be] atoms g^{-1}	AMS Uncert. atoms g^{-1} %	Erosion rate mm ky^{-1}	Rate Uncert. mm ky^{-1}
R191	18.291	-65.791	688	1.22	155	0.403	51700	2790 5.4%	152	6
ES A8	18.289	-65.798	766	1.47	110	0.513	57200	1090 1.9%	142	4
IC A6	18.288	-65.79	663	1.04	115	0.498	39300	903 2.3%	277	9
IC A7	18.287	-65.793	684	1.15	135	0.455	82100	1560 1.9%	124	5
IC A7 rep	18.287	-65.793	684	1.15	135	0.455	71100	3550 5%	106	3
IC A11	18.276	-65.787	630	1.78	105	0.545	68300	2120 3.1%	91	3
IC A12	18.277	-65.783	656	1.62	130	0.455	28100	1070 3.8%	239	8
T1OX	18.285	-65.787	650	1.6	135	0.455	81700	1550 1.9%	74	2
SA LL	18.279	-65.8	661	1.6	225	0.264	56600	1080 1.9%	80	3

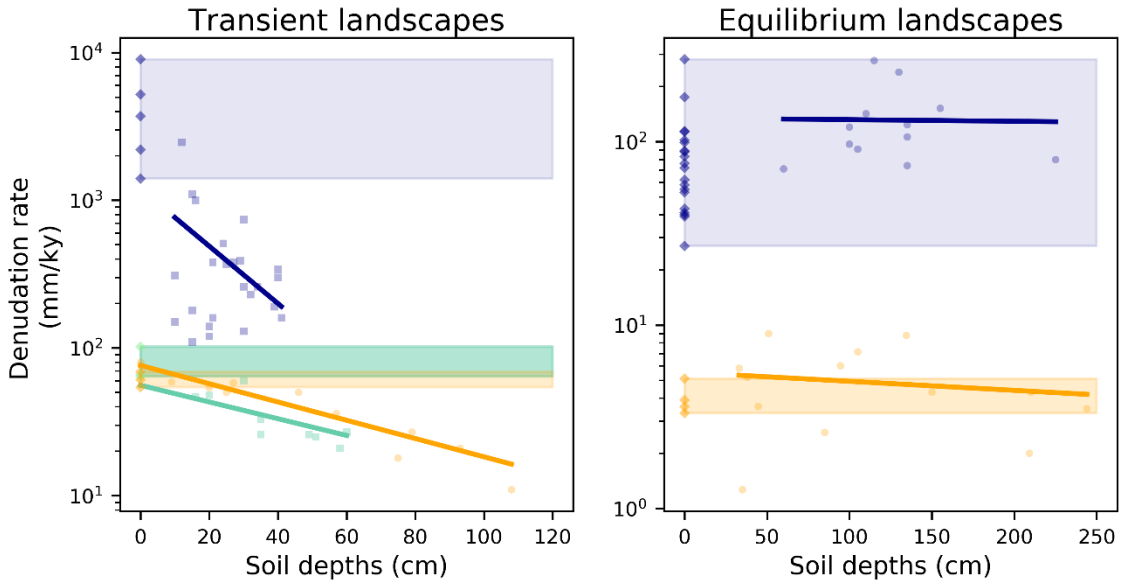

Figure 24 - Catchment averaged erosion rates versus soil production functions. Catchment average denudation rates plotted with diamonds and range of values indicated with coloured-shading. Soil production rates and soil production functions correspond to the same sites shown in Figure 21 of the chapter text.

Table 13. Site properties in transient landscapes

Site	Vegetation	MAP mm	MAT C	Dominant lithology
Oregon Coast	Dense coniferous	2300	11	sandstone
Tin Camp, AU	Open dry-sclerophyll forest with abundant seasonal grassland	1400	27	sandstone
Nunnock River, AU	Semi-arid eucalyptus grassland savannah	720	11.4	granite/granodiorite
Tennessee Valley, California	Coastal grassland and scrub	1200	14	greywacke/greenstone
New Zealand	Temperate rainforest and subalpine shrub	10000	5	schist
San Gabriels, CA	Mixed conifer, oak, chaparral	950	13	granite/metamorphic
La Serena, Chile	Desert scrub/succulents	100	13.6	plutonic/mixed
Frog Hollow, Australia	Semi-arid eucalyptus grassland savannah	600	16	granodiorite
Point Reyes CA	Conifer, oak, shrubland	940	15.5	granodiorite

Table 14. Vegetation fall and decomposition in transient sites

	Climate zone	Life form	Litterfall kg/ha/yr	Litter Residence Time years
Oregon Coast	Warm temperate	Needleleaf, Evergreen	4432	4.6
Tin Camp, AU	Mediterranean	Broadleaf, Evergreen	3042	3.7
Nunnock River, AU	Mediterranean	Broadleaf, Evergreen	3042	3.7
New Zealand	Cold temperate	Broadleaf, Deciduous	3854	10.2
Frog Hollow, Australia	Mediterranean	Broadleaf, Evergreen	3042	3.7
Point Reyes CA	Mediterranean	Broadleaf, Evergreen	3042	3.7

Table 15. Site properties in equilibrium landscapes

Site	Vegetation	MAP mm	MAT C	Dominant lithology
South Africa	Semiarid/sparse	600	22	granite
South Korea	Subalpine	1850	5	granite
Puerto Rico	Tropical rainforest	4500	27	quartz diorite
La Serena, Chile	Desert scrub/succulents	100	13.6	plutonic/mixed
Yungay, Chile	Hyperarid, no plant life	2	16	plutonic/mixed
Sierra Nevada, Province Creek	Upper mixed conifer	920	8.9	granodiorite
Sierra Nevada, Blasingame	Oak-grassland	370	16.6	tonalite
Blue Mtns, Australia	Wodland/Forest and "heath" or scrub	700	16.5	sandstone
Bodmin Moor, UK	Grasses	1250	10	granite
Idaho	Subalpine	660	14	granite/granodirite

Table 16. Vegetation fall and decomposition in equilibrium sites

	Climate zone	Life form	Litterfall kg/ha/yr	Litter Residence Time years
Puerto Rico	Tropical	Broadleaf, Evergreen	9369	2.6
La Serena, Chile	Semi-arid	Succulent	NA	NA
Yungay, Chile	Hyper-arid	None	NA	NA
Sierra Nevada, Province Creek	Warm temperate	Needleleaf, Evergreen	4432	4.6
Sierra Nevada, Blasingame	Mediterranean	Broadleaf, Evergreen	3042	3.7
Blue Mtns, Australia	Mediterranean	Broadleaf, Evergreen	3042	3.7

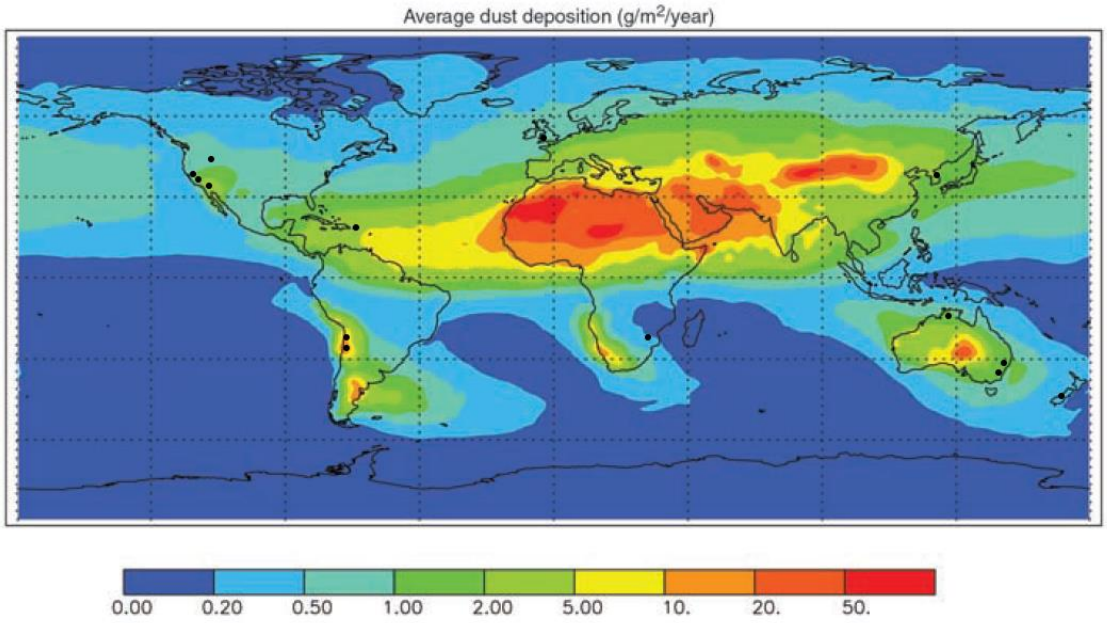

Figure 25- Global dust flux map with soil production sites identified. Average annual dust deposition for the world from Jickells et al., (2005). Soil production studies are identified with black circles

References

Abrams, D. M., Lobkovsky, A. E., Petroff, A. P., Straub, K. M., McElroy, B., Mohrig, D. C., … Rothman, D. H. (2009). Growth laws for channel networks incised by groundwater flow. *Nature Geoscience*, *2*(3), 193–196. https://doi.org/10.1038/ngeo432

Aide, T. ., Zimmerman, J. K., Herrera, L., Rosario, M., & Serrano, M. (1995). Forest recovery in abandoned tropical pastures in Puerto Rico. *Forest Ecology and Management*, *77*, 77–86.

Aide, T. M., Zimmerman, J. K., Pascarella, J. B., Rivera, L., & Marcano-Vega, H. (2000). Forest regeneration in a chronosequence of tropical abandoned pastures: Implications for restoration ecology. *Restoration Ecology*, *8*(4), 328–338. https://doi.org/10.1046/j.1526-100X.2000.80048.x

Aide, T. M., Zimmerman, J. K., Rosario, M., & Marcano-Vega, H. (1996). Forest Recovery in Abandoned Cattle Pastures Along an Elevational Gradient in Northeastern Puerto Rico. *Biotropica*, *28*(4), 537–548.

Amundson, R., Heimsath, A., Owen, J., Yoo, K., & Dietrich, W. E. (2015). Hillslope soils and vegetation. *Geomorphology*, *234*, 122–132. https://doi.org/10.1016/j.geomorph.2014.12.031

Amundson, R., Richter, D. D., Humphreys, G. S., Jobbágy, E. G., & Gaillardet, J. (2007). Coupling between biota and earth materials in the critical zone. *Elements*, *3*(5), 327–332. https://doi.org/10.2113/gselements.3.5.327

Arienzo, M. M., Swart, P. K., Broad, K., Clement, A. C., Pourmand, A., & Kakuk, B. (2017). Multi-proxy evidence of millennial climate variability from multiple Bahamian speleothems. *Quaternary Science Reviews*, *161*, 18–29. https://doi.org/10.1016/j.quascirev.2017.02.004

Arienzo, M. M., Swart, P. K., Pourmand, A., Broad, K., Clement, A. C., Murphy, L. N., … Kakuk, B. (2015). Bahamian speleothem reveals temperature decrease associated with Heinrich stadials. *Earth and Planetary Science Letters*, *430*, 377–386. https://doi.org/10.1016/j.epsl.2015.08.035

Balco, G., Briner, J., Finkel, R. C., Rayburn, J. A., Ridge, J. C., & Schaefer, J. M. (2009). Regional beryllium-10 production rate calibration for late-glacial northeastern North America. *Quaternary Geochronology*, *4*(2), 93–107. https://doi.org/10.1016/j.quageo.2008.09.001

Balco, G., Stone, J. O., Lifton, N. A., & Dunai, T. J. (2008, August). A complete and easily accessible means of calculating surface exposure ages or erosion rates from 10 Be and 26 Al measurements. *Quaternary Geochronology*, Vol. 3, pp. 174–195. https://doi.org/10.1016/j.quageo.2007.12.001

Barker, B. S., Rodríguez-Robles, J. A., & Cook, J. A. (2015). Climate as a driver of tropical insular diversity: Comparative phylogeography of two ecologically distinctive frogs in Puerto Rico. *Ecography*, *38*(8), 769–781. https://doi.org/10.1111/ecog.01327

Berenbrock, C., & Tranmer, A. W. (2008). Simulation of Flow , Sediment Transport , and

Sediment Mobility of the Lower Coeur d ' Alene River , Idaho. *U.S. Geological Survey Scientific Investigations Report*, 176.

Berger, W. H., Vincent, E., & Thierstein, H. R. (1981). THE DEEP SEA RECORD MAJOR STEPS IN CENOZOIC OCEAN EVOLUTION. *Society of Economic Paleontologists and Mineralogists*, (32), 489–504.

Bhatt, M. P., & McDowell, W. H. (2007). Controls on major solutes within the drainage network of a rapidly weathering tropical watershed. *Water Resources Research*. https://doi.org/10.1029/2007WR005915

Bird, M. I., Fyfe, W. S., Pinheiro-Dick, D., & Chivas, A. R. (1992). Partly Deforested Catchment. *Global Biogeochemical Cycles*, *6*(3), 293–306.

Boschi, V., & Willenbring, J. K. (2016). The effect of pH, organic ligand chemistry and mineralogy on the sorption of beryllium over time. *Environmental Chemistry*, *13*(4), 711–722. https://doi.org/10.1071/EN15107

Bouchez, J., Beyssac, O., Galy, V., Gaillardet, J., France-Lanord, C., Maurice, L., & Moreira-Turcq, P. (2010). Oxidation of petrogenic organic carbon in the Amazon floodplain as a source of atmospheric CO2. *Geology*, *38*(3), 255–258. https://doi.org/10.1130/G30608.1

Boye, K., Noël, V., Tfaily, M. M., Bone, S. E., Williams, K. H., Bargar, J. R., & Fendorf, S. (2017). Thermodynamically controlled preservation of organic carbon in floodplains. *Nature Geoscience*, *10*(6), 415–419. https://doi.org/10.1038/ngeo2940

Bradbury, J. P. (1997). Sources of glacial moisture in Mesoamerica. *Quaternary International*, *43–44*(97), 97–110.

Bradbury, J. P., Leyden, B., Salgado-Labouriau, M., Lewis, W. M., Schubert, C., Binford, M. W., … Weibezahn, F. H. (1981). Late Quaternary Environmental History of Lake Valencia, Venezuela. *Science*, *214*(4527), 1299 LP – 1305. https://doi.org/10.1126/science.214.4527.1299

Brantley, S. L., Goldhaber, M. B., & Vala Ragnarsdottir, K. (2007). Crossing disciplines and scales to understand the critical zone. *Elements*, *3*(5), 307–314. https://doi.org/10.2113/gselements.3.5.307

Brocard, G. Y., Willenbring, J. K., Miller, T. E., & Scatena, F. N. (2016). Relict landscape resistance to dissection by upstream migrating knickpoints. *Journal of Geophysical Research: Earth Surface*. https://doi.org/10.1002/2015JF003678

Brocard, G. Y., Willenbring, J. K., Scatena, F. N., & Johnson, A. H. (2015). Effects of a tectonically-triggered wave of incision on riverine exports and soil mineralogy in the Luquillo Mountains of Puerto Rico. *Applied Geochemistry*, *63*, 586–598. https://doi.org/10.1016/j.apgeochem.2015.04.001

Brokaw, N., & Grear, J. S. (1991). Forest Structure Before and After Hurricane Hugo at Three Elevations in the Luquillo Mountains , Puerto Rico. *Biotropica*, *23*(4), 317–323.

Brokaw, N. V. (1998). Cecropia schreberiana in the Luquillo Mountains of Puerto Rico. *Review Literature And Arts Of The Americas*, *64*(JUNE), 91–120.

Brown, E. T., Stallard, R. F., Larsen, M. C., Raisbeck, G. M., & Yiou, F. (1995). Denudation rates determined from the accumulation of in situ-produced 10Be in the luquillo experimental forest, Puerto Rico. *Earth and Planetary Science Letters*, *129*(1–4), 193–202. https://doi.org/10.1016/0012-821X(94)00249-X

Brown, S., Lugo, A. E., Silander, S., & Liegel, L. (1983). Research history and opportunities in the Luquillo Experimental Forest. *Gen. Tech. Rep. SO-44. New Orleans, LA: US Dept of Agriculture, Forest Service, Southern Forest Experiment Station. 132*, 44.

Buck, C., Christen, A. J., & James, G. N. (1999). BCal: an on-line Bayesian radiocarbon calibration tool. *Internet Archaeology*, *7*(7). Retrieved from http://bcal.sheffield.ac.uk

Burney, D. A., Burney, L. P., & MacPhee, R. D. E. (1994). Holocene charcoal stratigraphy from Laguna Tortuguero, Puerto Rico, and the timing of human arrival on the Island. *Journal of Archaeological Science*, *21*(2), 273–281. https://doi.org/10.1006/jasc.1994.1027

Burns, C. E., Mountney, N. P., Hodgson, D. M., & Colombera, L. (2017). Anatomy and dimensions of fluvial crevasse-splay deposits: Examples from the Cretaceous Castlegate Sandstone and Neslen Formation, Utah, U.S.A. *Sedimentary Geology*, *351*, 21–35. https://doi.org/10.1016/j.sedgeo.2017.02.003

Buss, H. L., Brantley, S. L., Scatena, F. N., Bazilievskaya, E. A., Blum, A., Schulz, M., … Cole, D. (2013). Probing the deep critical zone beneath the luquillo experimental forest, Puerto Rico. *Earth Surface Processes and Landforms*, *38*(10), 1170–1186. https://doi.org/10.1002/esp.3409

Buss, H. L., Sak, P. B., Webb, S. M., & Brantley, S. L. (2008). Weathering of the Rio Blanco quartz diorite, Luquillo Mountains, Puerto Rico: Coupling oxidation, dissolution, and fracturing. *Geochimica et Cosmochimica Acta*. https://doi.org/10.1016/j.gca.2008.06.020

Byun, J., Heimsath, A. M., Seong, Y. B., & Lee, S. Y. (2015). Erosion of a high-altitude, low-relief area on the Korean Peninsula: Implications for its development processes and evolution. *Earth Surface Processes and Landforms*, *40*(13), 1730–1745. https://doi.org/10.1002/esp.3749

Cai, D. L., Tan, F. C., & Edmond, J. M. (1988). Sources and transport of particulate organic carbon in the Amazon River and estuary. *Estuarine, Coastal and Shelf Science*, *26*(1), 1–14. https://doi.org/10.1016/0272-7714(88)90008-X

Carson, M. A., & Kirkby, M. J. (1972). *Hilslope form and Process*.

Cease, A. J., Elser, James, J., Ford, C. F., Hao, S., Kang, L., & Harrison, J. F. (2012). Heavy livestock grazing promotes locust outbreaks by lowering plant nitorgen content. *Warnell - School of Forest and Natural Resources*, *335*, 467–469.

Chabaux, F., Blaes, E., Stille, P., di Chiara Roupert, R., Pelt, E., Dosseto, A., … Brantley, S. L. (2013). Regolith formation rate from U-series nuclides: Implications from the study of a

spheroidal weathering profile in the Rio Icacos watershed (Puerto Rico). *Geochimica et Cosmochimica Acta*, *100*, 73–95. https://doi.org/10.1016/j.gca.2012.09.037

Chestnut, T. J., & McDowell, W. H. (2006). C and N dynamics in the riparian and hyporheic zones of a tropical stream, Luquillo Mountains, Puerto Rico. *Journal of the North American Benthological Society*. https://doi.org/10.2307/1468065

Chmeleff, J., von Blanckenburg, F., Kossert, K., & Jakob, D. (2010). Determination of the 10 Be half-life by multicollector ICP-MS and liquid scintillation counting. *Nuclear Instruments and Methods in Physics Research, Section B: Beam Interactions with Materials and Atoms*, *268*(2), 192–199. https://doi.org/10.1016/j.nimb.2009.09.012

Chorover, J., Kretzschmar, R., Garica-Pichel, F., & Sparks, D. L. (2007). Soil biogeochemicial processes within the critical zone. *Elements*, *3*(5), 321–326. https://doi.org/10.2113/gselements.3.5.321

Clark, M. K., House, M. A., Royden, L. H., Whipple, K. X., Burchfiel, B. C., Zhang, X., & Tang, W. (2005). Late Cenozoic uplift of southeastern Tibet. *Geology*, *33*(6), 525–528. https://doi.org/10.1130/G21265.1

Clement, A. C., Seager, R., & Cane, M. A. (2000). Suppression of El Niño during the mid-Holocene by changes in the Earth's orbit. *Paleoceanography*, *15*(6), 731–737. https://doi.org/10.1029/1999PA000466

Codilean, A. T. (2006). Calculation of the cosmogenic nuclide production topographic shielding scaling factor for large areas using DEMs. *Earth Surface Processes and Landforms*, *31*, 785–794. https://doi.org/10.1002/esp.1336

Collatz, G. J., Berry, A., & Clark, J. S. (1998). Effects of climate and atmospheric CO2 partial pressure on the global distribution of C4 grasses: present, past, and future. *Oecologia*, *114*, 441–454.

Collins, D. B. G., Bras, R. L., & Tucker, G. E. (2004). Modeling the effects of vegetation-erosion coupling on landscape evolution. *Journal of Geophysical Research*, *109*(F3), 1–11. https://doi.org/10.1029/2003jf000028

Comas, X., Wright, W., Hynek, S. A., Fletcher, R. C., & Brantley, S. L. (2018). Understanding fracture distribution and its relation to knickpoint evolution in the Rio Icacos watershed (Luquillo Critical Zone Observatory, Puerto Rico) using landscape-scale hydrogeophysics. *Earth Surface Processes and Landforms*. https://doi.org/10.1002/esp.4540

Crosby, B. T., & Whipple, K. X. (2006). Knickpoint initiation and distribution within fluvial networks: 236 waterfalls in the Waipaoa River, North Island, New Zealand. *Geomorphology*, *82*(1–2), 16–38. https://doi.org/10.1016/j.geomorph.2005.08.023

Derry, L. A., Pett-Ridge, J. C., Kurtz, A. C., & Troester, J. W. (2006). Ge/Si and 87Sr/86Sr tracers of weathering reactions and hydrologic pathways in a tropical granitoid system. *Journal of Geochemical Exploration*. https://doi.org/10.1016/j.gexplo.2005.08.054

DiBiase, R. A. (2018). Short communication: Increasing vertical attenuation length of

cosmogenic nuclide production on steep slopes negates topographic shielding corrections for catchment erosion rates. *Earth Surface Dynamics*, *6*(4), 923–931. https://doi.org/10.5194/esurf-6-923-2018

DiBiase, R. A., & Whipple, K. X. (2011). The influence of erosion thresholds and runoff variability on the relationships among topography, climate, and erosion rate. *Journal of Geophysical Research: Earth Surface*, *116*(4), 1–17. https://doi.org/10.1029/2011JF002095

Dietrich, W. E., Hsu, M., & Montgomery, D. R. (1995). A process based model for colluvial soil depth and shallow landsliding using digital elevation data. *Hydrological Processes*, *9*, 383–400.

Dietrich W.E., & Dunne, T. (1993). The Channel Head. In *Channel Network Hydrology* (pp. 175–219).

Dixon, J. L., Heimsath, A. M., & Amundson, R. (2009). The critical role of climate and saprolite weathering in landscape evolution. *Earth Surface Processes and Landforms*, *34*, 1507–1521.

Dixon, J. L., Heimsath, A. M., Kaste, J., & Amundson, R. (2009). Climate-driven processes of hillslope weathering. *Geology*, *37*(11), 975–978. https://doi.org/10.1130/G30045A.1

Dixon, J. L., & Riebe, C. S. (2014). Tracing and pacing soil across slopes. *Elements*, *10*(5), 363–368. https://doi.org/10.2113/gselements.10.5.363

Dixon, J. L., & von Blanckenburg, F. (2012). Soils as pacemakers and limiters of global silicate weathering. *Comptes Rendus - Geoscience*, *344*(11–12), 597–609. https://doi.org/10.1016/j.crte.2012.10.012

Donnelly, J. P., & Woodruff, J. D. (2007). Intense hurricane activity over the past 5,000 years controlled by El Niño and the West African monsoon. *Nature*, *447*(7143), 465–468. https://doi.org/10.1038/nature05834

Dosseto, A., Buss, H. L., & Suresh, P. O. (2011). The delicate balance between soil production and erosion, and its role on landscape evolution. *Applied Geochemistry*, *26*(SUPPL.). https://doi.org/10.1016/j.apgeochem.2011.03.020

Dosseto, Anthony, Buss, H. L., & Suresh, P. O. (2012). Rapid regolith formation over volcanic bedrock and implications for landscape evolution. *Earth and Planetary Science Letters*, *337–338*, 47–55. https://doi.org/10.1016/j.epsl.2012.05.008

Dunai, T. J. (2010). *Cosmogenic Nuclides: Principles, concepts and applications in the Earth surface sciences*. Cambridge University Press.

Dunai, T. J., & Lifton, N. A. (2014). The nuts and bolts of cosmogenic nuclide production. *Elements*, *10*(5), 347–350. https://doi.org/10.2113/gselements.10.5.347

Dunne, T. (1980). Formation and controls of channel networks. *Progress in Physical Geography*, *4*(2), 211–239. https://doi.org/10.1177/030913338000400204

Dunne, T. (1990). Hydrology and mechanics of erosion by subsurface flow. *Geological Society of America*, (Special Paper 252). Retrieved from https://www.researchgate.net/publication/313403172

Eidelman, S., & Group, P. D. (2004). Review of Particle Physics. *Physics Letters B*, *592*, 1–5. https://doi.org/10.1016/j.physletb.2004.06.001

Emmett, W. W. (1980). A field calibration of the sediment- trapping characteristics of the Helley-Smith bedload sampler. *US Geological Survey, Professional Paper*, *1139*.

Enfield, D. B. (1996). Relationships of inter-American rainfall to tropical Atlantic and Pacific SST variability. *Geophysical Research Letters*, *23*(23), 3305–3308. https://doi.org/10.1029/96GL03231

Enfield, D. B., & Alfaro, E. J. (1999). The dependence of Caribbean rainfall on the interaction of the tropical Atlantic and Pacific Oceans. *Journal of Climate*, *12*(7), 2093–2103. https://doi.org/10.1175/1520-0442(1999)012<2093:TDOCRO>2.0.CO;2

Fairbanks, R. G. (1989). A 17,000-year glacio-eustatic sea level record: influence of glacial melting rates on the Younger Dryas event and deep-ocean circulation. *Nature*, *342*, 637–642.

Farquhar, G. D., Ehleringer, J. R., & Hubick, K. T. (1989). CARBON ISOTOPE DISCRIMINATION AND PHOTOSYNTHESIS. *Annual Review of Plant Physiology and Plant Molecular Biology*, *40*, 503–537.

Fensterer, C., Scholz, D., Hoffmann, D. L., Spötl, C., Schröder-Ritzrau, A., Horn, C., … Mangini, A. (2013). Millennial-scale climate variability during the last 12.5ka recorded in a Caribbean speleothem. *Earth and Planetary Science Letters*, *361*, 143–151. https://doi.org/10.1016/j.epsl.2012.11.019

Ferrier, K. L., Kirchner, J. W., & Finkel, R. C. (2011). Estimating millennial-scale rates of dust incorporation into eroding hillslope regolith using cosmogenic nuclides and immobile weathering tracers. *Journal of Geophysical Research: Earth Surface*, *116*(3), 1–11. https://doi.org/10.1029/2011JF001991

Ferrier, K. L., Kirchner, J. W., Riebe, C. S., & Finkel, R. C. (2010). Mineral-specific chemical weathering rates over millennial timescales: Measurements at Rio Icacos, Puerto Rico. *Chemical Geology*. https://doi.org/10.1016/j.chemgeo.2010.07.013

Ferrier, K. L., Taylor Perron, J., Mukhopadhyay, S., Rosener, M., Stock, J. D., Huppert, K. L., & Slosberg, M. (2013). Covariation of climate and long-term erosion rates across a steep rainfall gradient on the Hawaiian island of Kaua'i. *Bulletin of the Geological Society of America*, *125*(7–8), 1146–1163. https://doi.org/10.1130/B30726.1

Fletcher, R. C., Buss, H. L., & Brantley, S. L. (2006). A spheroidal weathering model coupling porewater chemistry to soil thicknesses during steady-state denudation. *Earth and Planetary Science Letters*. https://doi.org/10.1016/j.epsl.2006.01.055

Franklin, J., Serra-Diaz, J. M., Syphard, A. D., & Regan, H. M. (2016). Global change and

terrestrial plant community dynamics. *Proceedings of the National Academy of Sciences*, *113*(14), 3725–3734. https://doi.org/10.1073/pnas.1519911113

Furbish, D., & Fagherazzi, S. (2001). Stability of creeping soil and implications for hillslope evolution. *Water Resources Research*, *37*(10), 2607–2618.

Gabet, E. J., & Mudd, S. M. (2009). A theoretical model coupling chemical weathering rates with denudation rates. *Geology*. https://doi.org/10.1130/G25270A.1

Galy, V., France-Lanord, C., & Lartiges, B. (2008). Loading and fate of particulate organic carbon from the Himalaya to the Ganga-Brahmaputra delta. *Geochimica et Cosmochimica Acta*, *72*(7), 1767–1787. https://doi.org/10.1016/j.gca.2008.01.027

García-Martinó, A. R., Warner, G. S., Scatena, F. N., & Civco, D. L. (1996). Rainfall, runoff and elevation relationships in the Luquillo Mountains of Puerto Rico. *Caribbean Journal of Science*.

Gardner, L. R., Michener, W. K., Blood, E. R., Williams, T. M., Lipscomb, D. J., & Jefferson, W. H. (1992). Ecological impact of Hurricane Hugo - salinization of a coastal forest. *Journal of Coastal Research, Special Issue*, *8*(8), 301–317.

Giannini, A., Cane, M. A., & Kushnir, Y. (2001). Interdecadal changes in the ENSO Teleconnection to the Caribbean Region and the North Atlantic Oscillation. *Journal of Climate*, *14*(13), 2867–2879. https://doi.org/10.1175/1520-0442(2001)014<2867:ICITET>2.0.CO;2

Giannini, A., Kushnir, Y., & Cane, M. A. (2000). Interannual Variability of Caribbean Rainfall, ENSO, and the Atlantic Ocean. *Journal of Climate*, (13.2), 297–311.

Gilbert, G. K. (1877). Report on the Geology of the Henry Mountains. In *U.S. Geological Survey of the Rocky Mountain region*.

Gilbert, G. K. (1909). The Convexity of Hilltops. *The Journal of Geology*, *17*(4), 344–350. https://doi.org/10.1086/621620

Giry, C., Felis, T., Kölling, M., Scholz, D., Wei, W., Lohmann, G., & Scheffers, S. (2012). Mid- to late Holocene changes in tropical Atlantic temperature seasonality and interannual to multidecadal variability documented in southern Caribbean corals. *Earth and Planetary Science Letters*, *331–332*, 187–200. https://doi.org/10.1016/j.epsl.2012.03.019

González, G., García, E., Cruz, V., Borges, S., Zalamea, M., & Rivera, M. M. (2007). Earthworm communities along an elevation gradient in Northeastern Puerto Rico. *European Journal of Soil Biology*, *43*(SUPPL. 1). https://doi.org/10.1016/j.ejsobi.2007.08.044

González, L. A., & Gómez, R. (2002). HIGH RESOLUTION SPELEOTHEM PALEOCLIMATOLOGY OF NORTHERN VENEZUELA: A PROGRESS REPORT. *Bol. Soc. Venezolana Espel.*, *36*, 27–29.

Gosse, J. C., & Phillips, F. M. (2001). Terrestrial in situ cosmogenic nuclides: Theory and application. *Quaternary Science Reviews*, *20*(14), 1475–1560.

https://doi.org/10.1016/S0277-3791(00)00171-2

Graly, J. A., Bierman, P. R., Reusser, L. J., & Pavich, M. J. (2010). Meteoric 10Be in soil profiles - A global meta-analysis. *Geochimica et Cosmochimica Acta*, *74*(23), 6814–6829. https://doi.org/10.1016/j.gca.2010.08.036

Graly, J. A., Reusser, L. J., & Bierman, P. R. (2011). Short and long-term delivery rates of meteoric 10Be to terrestrial soils. *Earth and Planetary Science Letters*, *302*(3–4), 329–336. https://doi.org/10.1016/j.epsl.2010.12.020

Granger, D. E., Kirchner, J. W., & Finkel, R. (1996). Spatially Averaged Long-Term Erosion Rates Measured from in Situ-Produced Cosmogenic Nuclides in Alluvial Sediment. *The Journal of Geology*. https://doi.org/10.1086/629823

Grieve, S. W. D., Mudd, S. M., & Hurst, M. D. (2016). How long is a hillslope? *Earth Surface Processes and Landforms*. https://doi.org/10.1002/esp.3884

Hack, J. T. (1960). *Interpretation of erosional topography in humid temperate regions*. Bobbs-Merrill.

Harden, C. P., & Scruggs, P. D. (2003). Infiltration on mountain slopes: A comparison of three environments. *Geomorphology*, *55*(1–4), 5–24. https://doi.org/10.1016/S0169-555X(03)00129-6

Harnois, L. (1988). The CIW index: A new chemical index of weathering. *Sedimentary Geology*, *55*(3–4), 319–322. https://doi.org/10.1016/0037-0738(88)90137-6

Harrison, E. J., Brocard, G. Y., & Willenbring, J. K. (2017). Resisting Self-Arrest: the Soil Production Function in Relict Landscapes. *American Geophysical Union Annual Meeting*.

Haug, G. H., Haug, G. H., Hughen, K. A., Sigman, D. M., Peterson, L. C., & Ro, U. (2011). *Southward Migration of the Intertropical Convergence Zone Through the Holocene*. *1304*(2001), 1304–1309. https://doi.org/10.1126/science.1059725

Heaton, T. H. E. (1999). Spatial, species, and temporal variations in the 13C/12C ratios of C3 plants: Implications for palaeodiet studies. *Journal of Archaeological Science*, *26*(6), 637–649. https://doi.org/10.1006/jasc.1998.0381

Hedges, J. I., Mayorga, E., Tsamakis, E., McClain, M. E., Aufdenkampe, A., Quay, P., … Maurice, L. (2000). Organic matter in Bolivian tributaries of the Amazon River: A comparison to the lower mainstream. *Limnology and Oceanography*, *45*(7), 1449–1466. https://doi.org/10.4319/lo.2000.45.7.1449

Hedges, J. I., Turin, H. J., & Ertel, J. R. (1984). Sources and distributions of sedimentary organic matter in the Columbia River drainage basin, Washington and Oregon. *Limnology and Oceanography*, *29*(1), 35–46. https://doi.org/10.4319/lo.1984.29.1.0035

Heikkilä, U., Beer, J., Abreu, J. A., & Steinhilber, F. (2013, June). On the atmospheric transport and deposition of the cosmogenic radionuclides (10Be): A review. *Space Science Reviews*, Vol. 176, pp. 321–332. https://doi.org/10.1007/s11214-011-9838-0

Heimsath, A. M., Chappell, J., Dietrich, W. E., Nishiizumi, K., & Finkel, R. C. (2000). Soil production on a retreating escarpment in southeastern Australia. *Geology*, *28*(9), 787–790. https://doi.org/10.1130/0091-7613(2000)28<787:SPOARE>2.0.CO;2

Heimsath, Arjun M. (2006). Eroding the land: Steady state and stochastic rates and processes through a cosmogenic lens. *Geochimica et Cosmochimica Acta*, *70*(18), A241. https://doi.org/10.1016/j.gca.2006.06.487

Heimsath, Arjun M., Chadwick, O. A., Roering, J. J., & Levick, S. R. (2019). Quantifying erosional equilibrium across a slowly eroding, soil mantled landscape. *Earth Surface Processes and Landforms*, 0–2. https://doi.org/10.1002/esp.4725

Heimsath, Arjun M., Chappell, J., Dietrich, W. E., Nishiizumi, K., & Finkel, R. C. (2001). Late Quaternary erosion in southeastern Australia: A field example using cosmogenic nuclides. *Quaternary International*, *82*(85), 169–185. https://doi.org/10.1016/S1040-6182(01)00038-6

Heimsath, Arjun M., DiBiase, R. A., & Whipple, K. X. (2012). Soil production limits and the transition to bedrock-dominated landscapes. *Nature Geoscience*, *5*(3), 210–214. https://doi.org/10.1038/ngeo1380

Heimsath, Arjun M., Dietrichs, W. E., Nishiizuml, K., & Finkel, R. C. (1997). The soil production function and landscape equilibrium. *Nature*, *388*(6640), 358–361. https://doi.org/10.1038/41056

Heimsath, Arjun M., Furbish, D. J., & Dietrich, W. E. (2005). The illusion of diffusion: Field evidence for depth-dependent sediment transport. *Geology*, *33*(12), 949–952. https://doi.org/10.1130/G21868.1

Herman, F., & Champagnac, J.-D. (2015). Plio-Pleistocene increase of erosion rates in mountain belts in response to climate change. *Terra Nova*, *28*(1). Retrieved from https://doi.org/10.1111/ter.12186

Higgins, C. G. (1982). Drainage systems developed by sapping on Earth and Mars. *Geology*, *10*(3), 147–152. https://doi.org/10.1130/0091-7613(1983)11<55b:carods>2.0.co;2

Hilley, G. E., & Arrowsmith, J. R. (2008). Geomorphic response to uplift along the Dragon's Back pressure ridge, Carrizo Plain, California. *Geology*, *36*(5), 367–370. https://doi.org/10.1130/G24517A.1

Hilley, G. E., Chamberlain, C. P., Moon, S., Porder, S., & Willett, S. D. (2010). Competition between erosion and reaction kinetics in controlling silicate-weathering rates. *Earth and Planetary Science Letters*. https://doi.org/10.1016/j.epsl.2010.01.008

Hobgood, J. S., & Cerveny, R. S. (1988). Ice-age hurricanes and tropical storms. *Nature*, *333*(6170), 243–245. https://doi.org/10.1038/333243a0

Hodell, D., Curtis, J., Jones, G., Higuera-Gundy, A., Brenner, M., Binford, M., & Dorsey, K. (1991). Reconstruction of Caribbean climate change over the past 10,500 years. *Nature*, *352*, 790–793.

Hoegh-Guldberg, O., Jacob, D., Taylor, M., M. Bindi, S. B., Camilloni, I., Diedhiou, A., … Zhou, G. (2018). Impacts of 1.5°C Global Warming on Natural and Human Systems. In *Global Warming of 1.5°C. An IPCC Special Report on the impacts of global warming of 1.5°C above pre-industrial levels and related global greenhouse gas emission pathways, in the context of strengthening the global response to the threat of climate change,*.

Hofman, C. L., Bright, A. J., & Ramos, R. R. (2010). CROSSING THE CARIBBEAN SEA: TOWARDS A HOLISTIC VIEW OF PRE-COLONIAL MOBILITY AND EXCHANGE. *Journal of Caribbean Archaeology*.

Homer, Huang, C. C., Yang, L., Wylie, B., & Coan, M. (2004). Development of a 2001 National Landcover Database for the United States. *Photogrammetric Engineering and Remote Sensing*, *70*(7), 829–840.

Houssais, M., Ortiz, C. P., Durian, D. J., & Jerolmack, D. J. (2015). Onset of sediment transport is a continuous transition driven by fluid shear and granular creep. *Nature Communications*, *6*, 1–8. https://doi.org/10.1038/ncomms7527

Howard, A. D. (1988). Groundwater Sapping Experiments and Modeling. In *Groundwater sapping experiments and modeling. Sapping Features of the Colorado Plateau: A Comparative Planetary Geology Field Guide* (pp. 71–83).

Howard, A. D. (1995). Simulation modeling and statistical classification of escarpment planforms. *Geomorphology*, *12*(3), 187–214. https://doi.org/10.1016/0169-555X(95)00004-O

Howard, A. D., & Mclane, C. F. (1988). Erosion of Cohensionless Sediment by Groundwater Seepage. *Water Resources*, *24*(10), 1659–1674. https://doi.org/10.1029/WR024i010p01659

Huang, Y., Street-Perrott, F. A., Metcalfe, S. E., Brenner, M., Moreland, M., & Freeman, K. H. (2001). Climate change as the dominant control on glacial-interglacial variations in C3 and C4 plant abundance. *Science*, *293*(5535), 1647–1651. https://doi.org/10.1126/science.1060143

Humphreys, G. S., & Wilkinson, M. T. (2007). The soil production function: A brief history and its rediscovery. *Geoderma*, *139*(1–2), 73–78. https://doi.org/10.1016/j.geoderma.2007.01.004

Hurst, M. D., Mudd, S. M., Attal, M., & Hilley, G. E. (2013). Hillslopes record the growth and decay of landscapes. *Science*, *341*(August), 868–872. https://doi.org/10.1126/science.1241791

Islebe, G. A., Hooghiemstra, H., Brenner, M., Curtis, J. H., & Hodell, D. A. (1996). A holocene vegetation history from lowland Guatemala. *Holocene*, *6*(3), 265–271. https://doi.org/10.1177/095968369600600302

Jagercikova, M., Cornu, S., Bourlès, D., Antoine, P., Mayor, M., & Guillou, V. (2015). Understanding long-term soil processes using meteoric 10 Be: A first attempt on loessic deposits. *Quaternary Geochronology*, *27*, 11–21.

https://doi.org/10.1016/j.quageo.2014.12.003

Jenny, H. (1994). *Factors of soil formation: a system of quantitative pedology*. Courier Corporation.

Jickells, T. D., An, Z. S., Andersen, K. K., Baker, A. R., Bergametti, C., Brooks, N., … Torres, R. (2005). Global iron connections between desert dust, ocean biogeochemistry, and climate. *Science*, *308*(5718), 67–71. https://doi.org/10.1126/science.1105959

Jungers, M. C., Bierman, P. R., Matmon, A., Nichols, K., Larsen, J., & Finkel, R. (2009). Tracing hillslope sediment production and transport with in situ and meteoric ^{10}Be. *Journal of Geophysical Research: Earth Surface*, *114*(4). https://doi.org/10.1029/2008JF001086

Khan, N. S., Ashe, E., Horton, B. P., Dutton, A., Kopp, R. E., Brocard, G., … Scatena, F. N. (2017). Drivers of Holocene sea-level change in the Caribbean. *Quaternary Science Reviews*, *155*, 13–36. https://doi.org/10.1016/j.quascirev.2016.08.032

Kirby, E., & Whipple, K. X. (2012). Expression of active tectonics in erosional landscapes. *Journal of Structural Geology*, *44*, 54–75. https://doi.org/10.1016/j.jsg.2012.07.009

Koch, A., Brierley, C., Maslin, M. M., & Lewis, S. L. (2019). Earth system impacts of the European arrival and Great Dying in the Americas after 1492. *Quaternary Science Reviews*, *207*, 13–36. https://doi.org/10.1016/j.quascirev.2018.12.004

Kohl, C. P., & Nishiizumi, K. (1992). Chemical isolation of quartz for measurement of in-situ produced cosmogenic nuclides. *Geochimica et Cosmochimica Acta*, *56*, 3583–3587.

Kohn, M. J. (2010). *Carbon isotope compositions of terrestrial C3 plants as indicators of (paleo)ecology and (paleo)climate*. *107*(46). https://doi.org/10.1073/pnas.1004933107/-/DCSupplemental

Kraus, M. J., & Aslan, A. (1993). Eocene hydromorphic paleosols: significance for interpreting ancient floodplain processes. *Journal of Sedimentary Petrology*, *63*(3), 453–463. https://doi.org/10.1306/D4267B22-2B26-11D7-8648000102C1865D

Kurtz, A. C., Lugolobi, F., & Salvucci, G. (2011). Germanium-silicon as a flow path tracer: Application to the Rio Icacos watershed. *Water Resources Research*. https://doi.org/10.1029/2010WR009853

Laity, J., & Malin, M. (1985). Sapping processes and the development of theater-headed valley networks on the Colorado Plateau. *Geological Society of America Bulletin*, *96*(February), 203–217.

Lal, D. (1991). Cosmic ray labeling of erosion surfaces: in situ nuclide production rates and erosion models. *Earth and Planetary Science Letters*, *104*, 424–439.

Lal, D., & Peters, B. (1967). Cosmic Ray Produced Radioactivity on the Earth. In *HANDBOOK OF PHYSICS* (VOLUME 46/, pp. 551–612). https://doi.org/10.1007/978-3-642-46079-1_7

Lamb, M. P., Howard, A. D., Dietrich, W. E., & Perron, J. T. (2007). Formation of amphitheater-

headed valleys by waterfall erosion after large-scale slumping on Hawai'i. *Bulletin of the Geological Society of America*. https://doi.org/10.1130/B25986.1

Lamb, M. P., Howard, A. D., Johnson, J., Whipple, K. X., Dietrich, W. E., & Perron, J. T. (2006). Can springs cut canyons into rock? *Journal of Geophysical Research E: Planets*. https://doi.org/10.1029/2005JE002663

Larsen, I. J., Almond, P. C., Eger, A., Stone, J. O., Montgomery, D. R., & Malcolm, B. (2014). Rapid soil production and weathering in the Southern Alps, New Zealand. *Science*, *343*(6171), 637–640. https://doi.org/10.1126/science.1244908

Larsen, I. J., & Montgomery, D. R. (2012). Landslide erosion coupled to tectonics and river incision. *Nature Geoscience*, *5*(7), 468–473. https://doi.org/10.1038/ngeo1479

Larsen, M. C., & Torres Sanchez, A. J. (1992). Landslides triggered by Hurricane Hugo in eastern Puerto Rico, September 1989. *Caribbean Journal of Science*, *28*(3–4), 113–125.

Larsen, Matthew C., Torres-Sánchez, A. J., & Concepción, I. M. (1999). Slopewash, surface runoff and fine-litter transport in forest and landslide scars in humid-tropical steeplands, Luquillo Experimental Forest, Puerto Rico. *Earth Surface Processes and Landforms*, *24*(6), 481–502. https://doi.org/10.1002/(SICI)1096-9837(199906)24:6<481::AID-ESP967>3.0.CO;2-G

Larsen, Matthew C, & Torres-Sanchez, A. J. (1998). The frequency and distribution of recent landslides in three montane tropical regions of Puerto Rico. *Geomorphology*, *24.4*, 309–331.

Leyden, B. W. (2009). Late Quaternary Aridity and Holocene Moisture Fluctuations in the Lake Valencia Basin , Venezuela Author (s): Barbara W . Leyden Published by : Ecological Society of America Stable URL : http://www.jstor.org/stable/1939181 LATE QUATERNARY ARIDITY AND HO. *America*, *66*(4), 1279–1295.

Leyden, B. W., Brenner, M., Hodell, D. A., & Curtis, J. H. (1994). Orbital and internal forcing of climate on the Yucatan Peninsula for the past ca. 36 ka. *Palaeogeography, Palaeoclimatology, Palaeoecology*, *109*(2–4), 193–210. https://doi.org/10.1016/0031-0182(94)90176-7

Lisiecki, L. E., & Raymo, M. E. (2005). A Pliocene-Pleistocene stack of 57 globally distributed benthic d18O records. *Paleoceanography*, *20*(1), 1–17. https://doi.org/10.1029/2004PA001071

Lodge, D. J., McDowell, W. H., & McSwiney, C. P. (1994). The importance of nutrient pulses in tropical forests. *Trends in Ecology and Evolution*, *9*(10), 384–387. https://doi.org/10.1016/0169-5347(94)90060-4

Lodge, D. Jean, Scatena, F. N., Asbury, C. E., & Sanchez, M. J. (1991). Fine Litterfall and Related Nutrient Inputs Resulting From Hurricane Hugo in Subtropical Wet and Lower Montane Rain Forests of Puerto Rico. *Biotropica*, *23*(4a), 336–342.

Lodge, D Jean, & McDowell, W. H. (1991). Summary of Ecosystem-Level Effects of Caribbean

Hurricane. *Biotropica*, *23*(4), 373–378.

Louchouarn, P., Lucotte, M., Canuel, R., Gagné, J. P., & Richard, L. F. (1997). Sources and early diagenesis of lignin and bulk organic matter in the sediments of the Lower St. Lawrence Estuary and the Saguenay Fjord. *Marine Chemistry*, *58*(1–2), 3–26. https://doi.org/10.1016/S0304-4203(97)00022-4

Louchouarn, P., Lucotte, M., & Farella, N. (1999). Historical and geographical variations of sources and transport of terrigenous organic matter within a large-scale coastal environment. *Organic Geochemistry*, *30*(7), 675–699. https://doi.org/10.1016/S0146-6380(99)00019-4

Lugo, A. E. (2004). The outcome of alien tree invasions in Puerto Rico. *Frontiers in Ecology and the Environment*, *2*(5), 265–273. https://doi.org/10.1890/1540-9295(2004)002[0265:TOOATI]2.0.CO;2

Lugo, A. E., Francis, J. K., & Frangi, J. L. (1998). Prestoea montana (R. Graham) Nichols. Sierra Palm. Palmaceae. Palm family. *Rio Piedras, Puerto Rico: US Department of Agriculture, Forest Service, International Institute of Tropical Forestry;*, *9 p.(SO-IT*.

Lugo, A. E., & Helmer, E. (2004). Emerging forests on abandoned land: Puerto Rico's new forests. *Forest Ecology and Management*, *190*(2–3), 145–161. https://doi.org/10.1016/j.foreco.2003.09.012

Lugo, A. E., & Scatena, F. N. (1996). Background and Catastrophic Tree Mortality in Tropical Moist , Wet , and Rain Forests. *Biotropica*, *28*(4), 585–599.

Lyell, C., & Deshayes, G. P. (1830). *Principles of Geology: Being an Attempt to Explain the Former Changes of the Earth's Surface by References to Causes Now in Operation*.

Mackey, B. H., Roering, J. J., & Lamb, M. P. (2011). Landslide-dammed paleolake perturbs marine sedimentation and drives genetic change in anadromous fish. *Proceedings of the National Academy of Sciences of the United States of America*, *108*(47), 18905–18909. https://doi.org/10.1073/pnas.1110445108

Maclaurin, D., Duvenaud, D., Johnson, M., & Townsend, J. (n.d.). Autograd. Retrieved from https://github.com/HIPS/autograd

Maher, K. (2010). The dependence of chemical weathering rates on fluid residence time. *Earth and Planetary Science Letters*. https://doi.org/10.1016/j.epsl.2010.03.010

Maher, K. (2011). The role of fluid residence time and topographic scales in determining chemical fluxes from landscapes. *Earth and Planetary Science Letters*. https://doi.org/10.1016/j.epsl.2011.09.040

Marin-Spiotta, E., Silver, W. L., Swanston, C. W., & Ostertag, R. (2009). Soil organic matter dynamics during 80 years of reforestation of tropical pastures. *Global Change Biology*, *15*(6), 1584–1597. https://doi.org/10.1111/j.1365-2486.2008.01805.x

Marshall, J. A., Roering, J. J., Bartlein, P. J., Gavin, D. G., Granger, D. E., Rempel, A. W., …

Hales, T. C. (2015). Earth Sciences: Frost for the Trees: Did climate increase erosion in unglaciated landscapes during the late Pleistocene? *Science Advances*, *1*(10). https://doi.org/10.1126/sciadv.1500715

McDowell, W. H., & Asbury, C. E. (1994). Export of carbon, nitrogen, and major ions from three tropical montane watersheds. *Limnology and Oceanography*. https://doi.org/10.4319/lo.1994.39.1.0111

Metcalfe, S. E., Bimpson, A., Courtice, A. J., O'Hara, S. L., & Taylor, D. M. (1997). Climate change at the monsoon/westerly boundary in Northern Mexico. *Journal of Paleolimnology*, *17*(2), 155–171. https://doi.org/10.1023/A:1007905824147

Meyer, D. L., Bries, J. M., Greenstein, B. J., & Debrot, A. O. (2003). Preservation of in situ reef framework in regions of low hurricane frequency: Pleistocene of Curaçao and Bonaire, southern Caribbean. *Lethaia*, *36*(3), 273–286. https://doi.org/10.1080/00241160310004675

Miller, P. W., Mote, T. L., & Ramseyer, C. A. (2019). An Empirical Study of the Relationship between Seasonal Precipitation and Thermodynamic Environment in Puerto Rico. *Weather and Forecasting*, *34*(2), 277–288. https://doi.org/10.1175/waf-d-18-0127.1

Montgomery, D. R. (2007). Soil erosion and agricultural sustainability. *Proceedings of the National Academy of Sciences of the United States of America*, *104*(33), 13268–13272. https://doi.org/10.1073/pnas.0611508104

Moore, R. D. (2004a). Introduction to salt dilution gauging for streamflow measurement Part 1. *Streamline Watershed Management Bulletin*, *7*(4), 20–23. https://doi.org/10.1592/phco.23.9.1S.32890

Moore, R. D. (2004b). Introduction to Salt Dilution Gauging for Streamflow Measurement Part 2: Constant-rate Injection. *Streamline Watershed Management Bulletin*, *8*(1), 1–15. https://doi.org/10.1002/bip.360310619

Moyer, R. P., Bauer, J. E., & Grottoli, A. G. (2013). Carbon isotope biogeochemistry of tropical small mountainous river, estuarine, and coastal systems of Puerto Rico. *Biogeochemistry*, *112*(1–3), 589–612. https://doi.org/10.1007/s10533-012-9751-y

Mudd, S. M., & Yoo, K. (2010). Reservoir theory for studying the geochemical evolution of soils. *Journal of Geophysical Research: Earth Surface*, *115*(3), 1–13. https://doi.org/10.1029/2009JF001591

Murphy, S. F., Stallard, R. F., Scholl, M. A., González, G., & Torres-Sánchez, A. J. (2017). Reassessing rainfall in the Luquillo Mountains, Puerto Rico: Local and global ecohydrological implications. *PLoS ONE*. https://doi.org/10.1371/journal.pone.0180987

Nishiizumi, K., Imamura, M., Caffee, M. W., Southon, J. R., Finkel, R. C., & McAninch, J. (2007). Absolute calibration of 10 Be AMS standards. *Nuclear Instruments and Methods in Physics Research, Section B: Beam Interactions with Materials and Atoms*, *258*(2), 403–413. https://doi.org/10.1016/j.nimb.2007.01.297

Norton, K. P., & Schlunegger, F. (2017). Lack of a weathering signal with increased Cenozoic

erosion? *Terra Nova*, *29*(5). Retrieved from https://doi.org/10.1111/ter.12278

NRCS. (n.d.). *NRCS Global Soil Regions map*. Retrieved from http://soils.usda.gov/use/worldsoils/mapindex/order.html

Nyberg, J., Malmgren, B. A., Kuijpers, A., & Winter, A. (2002). A centennial-scale variability of tropical North Atlantic surface hydrography during the late Holocene. *Palaeogeography, Palaeoclimatology, Palaeoecology*, *183*(1–2), 25–41. https://doi.org/10.1016/S0031-0182(01)00446-1

O'Leary, M. H. (1988). Carbon Isotopes in Photosynthesis. *BioScience*, *38*(5), 328–336. https://doi.org/10.2307/1310735

Onstad, G. D., Canfield, D. E., Quay, P. D., & Hedges, J. I. (2000). Sources of particulate organic matter in rivers from the continental USA: Lignin phenol and stable carbon isotope compositions. *Geochimica et Cosmochimica Acta*, *64*(20), 3539–3546. https://doi.org/10.1016/S0016-7037(00)00451-8

Orlando, J., Comas, X., Hynek, S. A., Buss, H. L., & Brantley, S. L. (2016). Architecture of the deep critical zone in the Río Icacos watershed (Luquillo Critical Zone Observatory, Puerto Rico) inferred from drilling and ground penetrating radar (GPR). *Earth Surface Processes and Landforms*. https://doi.org/10.1002/esp.3948

Owen, J. J., Amundson, R., Dietrich, W. E., Nishiizumi, K., Sutter, B., & Chong, G. (2011). The sensitivity of hillslope bedrock erosion to precipitation. *Earth Surface Processes and Landforms*, *36*(1), 117–135. https://doi.org/10.1002/esp.2083

Pagán-Jiménez, J. R., Rodríguez-Ramos, R., Reid, B. A., van den Bel, M., & Hofman, C. L. (2015). Early dispersals of maize and other food plants into the Southern Caribbean and Northeastern South America. *Quaternary Science Reviews*, *123*, 231–246. https://doi.org/10.1016/j.quascirev.2015.07.005

Pauli Virtanen, Ralf Gommers, Travis E. Oliphant, Matt Haberland, Tyler Reddy, David Cournapeau, Evgeni Burovski, Pearu Peterson, Warren Weckesser, Jonathan Bright, Stéfan J. van der Walt, Matthew Brett, Joshua Wilson, K. Jarrod Millman, Nikolay Mayorov, and S. 1. . C. (2019). *SciPy 1.0–Fundamental Algorithms for Scientific Computing in Python*.

Pestle, W. J., Curet, L. A., Ramos, R. R., & López, M. R. (2013). New Questions and Old Paradigms: Reexamining Caribbean Culture History. *Latin American Antiquity*, *24*(03), 243–261. https://doi.org/10.7183/1045-6635.24.3.243

Peten, L., Curtis, J. H., Brenner, M., Hodell, D. A., Balser, R. A., Islebe, G. A., & Hooghiemstra, H. (1998). A multi-proxy study of Holocene environmental change in the Maya. *Journal of Paleolimnology*, *19*, 139–159. https://doi.org/10.1023/a:1007968508262

Peterson, L. C., & Haug, G. H. (2006). Variability in the mean latitude of the Atlantic Intertropical Convergence Zone as recorded by riverine input of sediments to the Cariaco Basin (Venezuela). *Palaeogeography, Palaeoclimatology, Palaeoecology*, *234*(1), 97–113. https://doi.org/10.1016/j.palaeo.2005.10.021

Petroff, A. P., Devauchelle, O., Abrams, D. M., Lobkovsky, A. E., Kudrolli, A., & Rothman, D. H. (2011). Geometry of valley growth. *Journal of Fluid Mechanics*, *673*, 245–254. https://doi.org/10.1017/S002211201100053X

Phillips, C. B., & Jerolmack, D. J. (2016). Self-organized river channels are a critical filter on climate signals. *Science*, *352*(6286), 694–697. https://doi.org/10.1126/science.aad3348

Pike, A. S., Scatena, F. N., & Wohl, E. E. (2010). Lithological and fluvial controls on the geomorphology of tropical montane stream channels in Puerto Rico. *Earth Surface Processes and Landforms*. https://doi.org/10.1002/esp.1978

Planavsky, N., Partin, C., & Bekker, A. (2016). Carbon Isotopes as a Geochemical Tracer. In *Encyclopedia of Astrobiology* (pp. 366–371). https://doi.org/10.1007/978-3-662-44185-5_228

Plug, L. J., Gosse, J. C., McIntosh, J. J., & Bigley, R. (2007). Attenuation of cosmic ray flux temperate forest. *Journal of Geophysical Research: Earth Surface*, *112*(2). https://doi.org/10.1029/2006JF000668

Porder, S., Xing, H. X., Brocard, G. Y., Pett-Ridge, J., Johnson, A. H., & Goldsmith, S. (2015). Linking geomorphology, weathering and cation availability in the Luquillo Mountains of Puerto Rico. *Geoderma*. https://doi.org/10.1016/j.geoderma.2015.03.002

Ramos, R. R., Jiménez, J. P., Santiago-Blay, J., Lambert, J. B., & Craig, P. R. (2013). Some indigenous uses of plants in pre-Columbian Puerto Rico. *Life: The Excitement of Biology*, *1*(1), 83–90. https://doi.org/10.9784/leb1(1)rodriguez.09

Ramseyer, C. A., Miller, P. W., & Mote, T. L. (2019). Future precipitation variability during the early rainfall season in the El Yunque National Forest. *Science of the Total Environment*, *661*, 326–336. https://doi.org/10.1016/j.scitotenv.2019.01.167

Rau, G. (1978). Carbon-13 depletion in a subalpine lake: Carbon flow implications. *Science*, *201*(4359), 901–902.

Raymo, M. E., & Ruddiman, W. F. (1992). Tectonic forcing of late Cenozoic climate. *Nature*, *359*(6391), 117–122. https://doi.org/10.1038/359117a0

Reiners, P. W., Ehlers, T. A., Mitchell, S. G., & Montgomery, D. R. (2003). Coupled spatial variations in precipitation and long-term erosion rates across the Washington Cascades. *Nature*, *426*(6967), 645–647. https://doi.org/10.1038/nature02111

Reinhardt, L. J., Bishop, P., Hoey, T. B., Dempster, T. J., & Sanderson, D. C. W. (2007). Quantification of the transient response to base-level fall in a small mountain catchment: Sierra Nevada, southern Spain. *Journal of Geophysical Research: Earth Surface*, *112*(3). https://doi.org/10.1029/2006JF000524

Rempe, D. M., & Dietrich, W. E. (2014). A bottom-up control on fresh-bedrock topography under landscapes. *Proceedings of the National Academy of Sciences*, *11*(18), 6576–6581. https://doi.org/10.1073/pnas.1404763111

Rempe, D. M., & Dietrich, W. E. (2018). Direct observations of rock moisture, a hidden component of the hydrologic cycle. *Proceedings of the National Academy of Sciences*. https://doi.org/10.1073/pnas.1800141115

Retallack, G. J. (2008). *Soils of the past: an introduction to paleopedology.* John Wiley & Sons.

Rico, P., Larsen, M. C., & Simon, A. (1993). A Rainfall Intensity-Duration Threshold for Landslides in a Humid-Tropical Environment. In *Source: Geografiska Annaler. Series A, Physical Geography* (Vol. 75).

Riebe, C. S., Kirchner, J. W., & Finkel, R. C. (2004). Erosional and climatic effects on long-term chemical weathering rates in granitic landscapes spanning diverse climate regimes. *Earth and Planetary Science Letters*. https://doi.org/10.1016/j.epsl.2004.05.019

Riebe, C. S., Kirchner, J. W., Granger, D. E., & Finkel, R. C. (2001). Strong tectonic and weak climatic control of long-term chemical weathering rates. *Geology*, *29*(6), 511–514. https://doi.org/10.1130/0091-7613(2001)029<0511:STAWCC>2.0.CO;2

Riggins, S. G., Anderson, R. S., Anderson, S. P., & Tye, A. M. (2011). Solving a conundrum of a steady-state hilltop with variable soil depths and production rates, Bodmin Moor, UK. *Geomorphology*, *128*(1–2), 73–84. https://doi.org/10.1016/j.geomorph.2010.12.023

Rivera-Collazo, I., Winter, A., Scholz, D., Mangini, A., Miller, T., Kushnir, Y., & Black, D. (2015). Human adaptation strategies to abrupt climate change in Puerto Rico ca. 3.5 ka. *Holocene*, *25*(4), 627–640. https://doi.org/10.1177/0959683614565951

Robert Bierman, P., & Nichols, K. K. (2004). Rock To Sediment—Slope To Sea With 10 Be—Rates of Landscape Change . *Annual Review of Earth and Planetary Sciences*, *32*(1), 215–255. https://doi.org/10.1146/annurev.earth.32.101802.120539

Rodbell, D. T., Seltzer, G. O., Anderson, D. M., Abbott, M. B., Enfield, D. B., & Newman, J. H. (1999). An ~15,000-year record of El Nino-driven alluviation in Southwestern Ecuador. *Science*, *283*(5401), 516–520. https://doi.org/10.1126/science.283.5401.516

Roering, J. J., Kirchner, J. W., & Dietrich, W. E. (1999). Evidence for nonlinear, diffusive sediment transport on hillslopes and implications for landscape morphology. *Water Resources Research*, *35*(3), 853–870. https://doi.org/10.1029/1998WR900090

Roering, J. J., Mackey, B. H., Handwerger, A. L., Booth, A. M., Schmidt, D. A., Bennett, G. L., & Cerovski-Darriau, C. (2015). Beyond the angle of repose: A review and synthesis of landslide processes in response to rapid uplift, Eel River, Northern California. *Geomorphology*, Vol. 236. https://doi.org/10.1016/j.geomorph.2015.02.013

Sandweiss, D. H., Richardson, J. B., Reitz, E. J., Rollins, H. B., & Maasch, K. A. (1996). Geoarchaeological Evidence from Peru for a 5000 Years B.P. Onset of El Niño. *Science*, *273*(5281), 1531–1533.

Sanford, R. L., Parton, W. J., Ojima, D. S., & Lodge, J. D. (1991). *Hurricane Effects on Soil Organic Matter Dynamics and Forest Production in the Luquillo Experimental Forest , Puerto Rico : Results of Simulation Modeling*. *23*(4), 364–372.

Sarmiento, J. L., & Gruber, N. (2002). Sinks for anthropogenic carbon. *Physics Today*, *55*(8), 30. https://doi.org/10.1063/1.1510279

Scatena, F. N. (1989). *An introduction to the physiography and history of the Bisley Experimental Watersheds in the Luquillo Mountains of Puerto Rico*.

Scatena, F.N., Blanco, J. F., Beard, K. H., Waide, R. B., Lugo, A. E., Brokaw, N., … Zimmerman, J. K. (2012). Disturbance Regime. In *A Caribbean Forest Tapestry: the Multidimensional Nature of Disturbance and Response* (pp. 164–200). New York: Oxford University Press.

Scatena, Frederik N., & Larsen, M. C. (1991). Physical Aspects of Hurricane Hugo in Puerto Rico. *Biotropica*, *23*(4), 317–323.

Scatena, Fredrick N., Moya, S., Estrada, C., & Chinea, J. D. (1996). The First Five Years in the Reorganization of Aboveground Biomass and Nutrient Use Following Hurricane Hugo in the Bisley Experimental Watersheds , Luquillo Experimental Forest. *Ecosystems*, *28*(4), 424–440.

Scheingross, J. S., Hovius, N., Dellinger, M., Hilton, R. G., Repasch, M., Sachse, D., … Turowski, J. M. (2019). Preservation of organic carbon during active fluvial transport and particle abrasion. *Geology*. https://doi.org/10.1130/G46442.1

Schellekens, J., Bruijnzeel, L. A., Scatena, F. N., Bink, N. J., & Holwerda, F. (2000). Evaporation from a tropical rain forest, Luquillo Experimental Forest, eastern Puerto Rico. *Water Resources Research*. https://doi.org/10.1029/2000WR900074

Schellekens, J., Scatena, F. N., Bruijnzeel, L. A., van Dijk, A. I. J. M., Groen, M. M. A., & van Hogezand, R. J. P. (2004). Stormflow generation in a small rainforest catchment in the Luquillo experimental forest, Puerto Rico. *Hydrological Processes*. https://doi.org/10.1002/hyp.1335

Scholl, M. A., Shanley, J. B., Murphy, S. F., Willenbring, J. K., Occhi, M., & González, G. (2015). Stable-isotope and solute-chemistry approaches to flow characterization in a forested tropical watershed, Luquillo Mountains, Puerto Rico. *Applied Geochemistry*. https://doi.org/10.1016/j.apgeochem.2015.03.008

Schulze, E. D., Ellis, R., Schulze, W., Trimborn, P., & Ziegler, H. (1996). Diversity, metabolic types and δ13C carbon isotope ratios in the grass flora of Namibia in relation to growth form, precipitation and habitat conditions. *Oecologia*, *106*(3), 352–369. https://doi.org/10.1007/BF00334563

Seiders, V. M. (1971). *Geologic map of the El Yunque quadrangle, Puerto Rico*. *658*.

Shanley, J. B., McDowell, W. H., & Stallard, R. F. (2011). Long-term patterns and short-term dynamics of stream solutes and suspended sediment in a rapidly weathering tropical watershed. *Water Resources Research*. https://doi.org/10.1029/2010WR009788

Shields, A. (1936). Application of similarity principles and turbulence research to bed-load movement. In *Hydrodynamic laboratory California Institute of Technology Pubublication*

no. 167. U.S. Department of Agriculture Soil Conservation Serivce Cooperative Laboratory.

Silver, W L, Scatena, F. N., Johnson, A. H., Siccama, T. G., & Sanchez, M. J. (1994). Nutrient availability in a montane wet tropical forest : Spatial patterns and methodological considerations. *Plant and Soil*, *164*(1), 129–145.

Silver, Whendee L., Hall, S. J., & González, G. (2014). Differential effects of canopy trimming and litter deposition on litterfall and nutrient dynamics in a wet subtropical forest. *Forest Ecology and Management*, *332*, 47–55. https://doi.org/10.1016/j.foreco.2014.05.018

Smith, A. L., Schellekens, J. H., & Diaz, A.-L. M. (1998). Batholiths as markers of tectonic change in the northeastern Caribbean. In E. G. Lidiak & D. K. Larue (Eds.), *Geological Society of America* (Tectonics). Boulder Colorado.

Smith, B. N., & Epstein, S. (1971). Two categories of c/c ratios for higher plants. *Plant Physiology*, *47*(3), 380–384.

Smith, J. S., Chandler, J., & Rose, J. (2009). Quantitative reconstruction of Late Cenozoic landscapes: a case study in the Sierra de Atapuerca (Burgos, Spain). *Earth Surface Processes and Landforms*, *34*(August 2007), 155–161. https://doi.org/10.1002/esp

Stallard, R. F. (2012). Weathering, landscape equilibrium, and carbon in four watersheds in eastern Puerto Rico: Chapter H in Water quality and landscape processes of four watersheds in eastern Puerto Rico. *No. 1789-H. US Geological Survey*, No. 1789-H, pp. 199–248.

Suresh, P. O., Dosseto, A., Hesse, P. P., & Handley, H. K. (2013, October 1). Soil formation rates determined from Uranium-series isotope disequilibria in soil profiles from the southeastern Australian highlands. *Earth and Planetary Science Letters*, Vol. 379, pp. 26–37. https://doi.org/10.1016/j.epsl.2013.08.004

Swanson, K. M., Watson, E., Aalto, R., Lauer, J. W., Bera, M. T., Marshall, A., … Dietrich, W. E. (2008). Sediment load and floodplain deposition rates: Comparison of the Fly and Strickland rivers, Papua New Guinea. *Journal of Geophysical Research: Earth Surface*, *113*(1), 2–17. https://doi.org/10.1029/2006JF000623

Tartaglione, C. A., Smith, S. R., & O'Brien, J. J. (2003). ENSO impact on hurricane landfall probabilities for the Caribbean. *Journal of Climate*, *16*(17), 2925–2931. https://doi.org/10.1175/1520-0442(2003)016<2925:EIOHLP>2.0.CO;2

Taylor, C. M., Silander, S., Waide, R. B., & Pfeiffer, W. J. (1995). Recovery of a tropical forest after gamma irradiation: a 23-year chronicle. In *Tropical forests: management and ecology* (pp. 258–285). New York: Springer.

Ten Brink, U. (2005). Vertical motions of the Puerto Rico Trench and Puerto Rico and their cause. *Journal of Geophysical Research: Solid Earth*, *110*(6), 1–16. https://doi.org/10.1029/2004JB003459

Thomlinson, J. R., Serrano, M. I., Lopez, T. M., Aide, T. M., & Zimmerman, J. K. (1996). Land-Use Dynamics in a Post-Agricultural Puerto Rican Landscape (1936-1988). *Biotropica*, *28*(4), 525–536.

Thurman, E. M. (2012). *Organic geochemistry of natural waters* (Vol. 2). Springer Science & Business Media.

Tieszen, L. L. (1991). Natural variations in the carbon isotope values of plants: Implications for archaeology, ecology, and paleoecology. *Journal of Archaeological Science*, *18*(3), 227–248. https://doi.org/10.1016/0305-4403(91)90063-U

Turner, B. F., Stallard, R. F., & Brantley, S. L. (2003). Investigation of in situ weathering of quartz diorite bedrock in the Rio Icacos basin, Luquillo experimental forest, Puerto Rico. *Chemical Geology*. https://doi.org/10.1016/j.chemgeo.2003.05.001

Valletta, R. D., Willenbring, J. K., Lewis, A. R., Ashworth, A. C., & Caffee, M. (2015). Extreme decay of meteoric beryllium-10 as a proxy for persistent aridity. *Scientific Reports*, *5*, 1–7. https://doi.org/10.1038/srep17813

Van Gestel, J. P., Mann, P., Grindlay, N. R., & Dolan, J. F. (1999). Three-phase tectonic evolution of the northern margin of Puerto Rico as inferred from an integration of seismic reflection, well, and outcrop data. *Marine Geology*, *161*(2–4), 257–286. https://doi.org/10.1016/S0025-3227(99)00035-3

Verheijen, F. G. A., Jones, R. J. A., Rickson, R. J., & Smith, C. J. (2009). Tolerable versus actual soil erosion rates in Europe. *Earth-Science Reviews*, *94*(1–4), 23–38. https://doi.org/10.1016/j.earscirev.2009.02.003

von Blanckenburg, F. (2004). Cosmogenic nuclide evidence for low weathering and denudation in the wet, tropical highlands of Sri Lanka. *Journal of Geophysical Research*, *109*(F3). https://doi.org/10.1029/2003jf000049

von Blanckenburg, F. (2005). The control mechanisms of erosion and weathering at basin scale from cosmogenic nuclides in river sediment. *Earth and Planetary Science Letters*, *237*(3–4), 462–479. https://doi.org/10.1016/j.epsl.2005.06.030

von Blanckenburg, F., Bouchez, J., & Wittmann, H. (2012). Earth surface erosion and weathering from the 10Be (meteoric)/9Be ratio. *Earth and Planetary Science Letters*, *351–352*, 295–305. https://doi.org/10.1016/j.epsl.2012.07.022

Von Blanckenburg, F., & Willenbring, J. K. (2014). Cosmogenic nuclides: Dates and rates of earth-surface change. *Elements*, *10*(5), 341–346. https://doi.org/10.2113/gselements.10.5.341

Walter J. Bawiec. (1999). Geology, Geochemistry, Geophysics, Mineral Occurrences and Mineral Resource Assessment for the Commonwealth of Puerto Rico. *U.S. Geological Survey Open-File Report 98-038*. Retrieved from http://pubs.usgs.gov/of/1998/of98-038/

Weerts, H. J. T., & Bierkens, M. F. P. (1993). Geostatistical analysis of overbank deposits of anastomosing and meandering fluvial systems; Rhine-Meuse delta, The Netherlands. *Sedimentary Geology*, *85*(1–4), 221–232. https://doi.org/10.1016/0037-0738(93)90085-J

Weiner, J. S., & Yu, P. Y. (1987). Calculations of the Critical Shear Stress for Motion of Uniform and Heterogeneous Sediments. *Water Resources Research*, *23*(8), 1471–1480.

Whipple, K.X., DiBiase, R. A., & Crosby, B. T. (2013). Bedrock Rivers. *Treatise on Geomorphology*, 550–573. https://doi.org/10.1016/B978-0-12-374739-6.00254-2

Whipple, Kelin X., & Tucker, G. E. (1999). Dynamics of the stream-power river incision model: Implications for height limits of mountain ranges, landscape response timescales, and research needs. *Journal of Geophysical Research*, *104*, 661–674.

Whipple, Kelin X., & Tucker, G. E. (2002). Implications of sediment-flux-dependent river incision models for landscape evolution. *Journal of Geophysical Research*, *107*(B2). https://doi.org/10.1029/2000jb000044

White, A. F., Blum, A. E., Schulz, M. S., Vivit, D. V, Stonestrom, D. A., Larsen, M., … Eberl, D. (1998). Chemical weathering in a tropical watershed, Luquillo Mountains, Puerto Rico: I. Long-term versus short-term weathering fluxes. *Geochimica et Cosmochimica Acta*, *62.2*, 209–226.

Wilkinson, M. T., Chappell, J., Humphreys, G. S., Fifield, K., Smith, B., & Hesse, P. (2005). Soil production in heath and forest, Blue Mountains, Australia: Influence of lithology and palaeoclimate. *Earth Surface Processes and Landforms*, *30*(8), 923–934. https://doi.org/10.1002/esp.1254

Willenbring, J. K., Gasparini, N. M., Crosby, B. T., & Brocard, G. Y. (2013). What does a mean mean? The temporal evolution of detrital cosmogenic denudation rates in a transient landscape. *Geology*, *41*(12), 1215–1218. https://doi.org/10.1130/G34746.1

Willenbring, J. K., & Jerolmack, D. J. (2015). The null hypothesis: globally steady rates of erosion, weathering fluxes and shelf sediment accumulation during Late Cenozoic mountain uplift and glaciation. *Terra Nova*, *28*(1). Retrieved from https://doi.org/10.1111/ter.12185

Willenbring, J. K., & von Blanckenburg, F. (2010, January 1). Meteoric cosmogenic Beryllium-10 adsorbed to river sediment and soil: Applications for Earth-surface dynamics. *Earth-Science Reviews*, Vol. 98, pp. 105–122. https://doi.org/10.1016/j.earscirev.2009.10.008

Willenbring, J. K., & Von Blanckenburg, F. (2010b). Long-term stability of global erosion rates and weathering during late-Cenozoic cooling. *Nature*, *465*(7295), 211–214. https://doi.org/10.1038/nature09044

Winter, A., Ishioroshi, H., Watanabe, T., Oba, T., & Christy, J. (2000). Caribbean sea surface temperatures: Two-to-three degrees cooler than present during the Little Ice Age. *Geophysical Research Letters*, *27*(20), 3365–3368. https://doi.org/10.1029/2000GL011426

Wohl, E., & Ogden, F. L. (2013). Organic carbon export in the form of wood during an extreme tropical storm, Upper Rio Chagres, Panama. *Earth Surface Processes and Landforms*, *38*(12), 1407–1416. https://doi.org/10.1002/esp.3389

Wolf, J., Brocard, G., Willenbring, J. K., Porder, S., & Uriarte, M. (2016). Abrupt change in forest height along a tropical elevation gradient detected using Airborne LiDAR. *Remote Sensing*, *8*(10). https://doi.org/10.3390/rs8100864

Wolman, M. G., & Leopold, L. B. (1957). *River Flood Plains: some observations on their*

formation.

Wood, T. E., González, G., Silver, W. L., Reed, S. C., & Cavaleri, M. A. (2019). On the shoulders of giants: Continuing the legacy of large-scale ecosystem manipulation experiments in Puerto Rico. *Forests*, *10*(3), 1–18. https://doi.org/10.3390/f10030210

Woodruff, J. D., Donnelly, J. P., Mohrig, D., & Geyer, W. R. (2008). Reconstructing relative flooding intensities responsible for hurricane-induced deposits from Laguna Playa Grande, Vieques, Puerto Rico. *Geology*, *36*(5), 391–394. https://doi.org/10.1130/G24731A.1

You, C. F., Lee, T., & Li, Y. H. (1989). The partition of Be between soil and water. *Chemical Geology*, *77*(2), 105–118. https://doi.org/10.1016/0009-2541(89)90136-8

Zimmerman, A. J. K., Pulliam, W. M., Lodge, D. J., Fetcher, N., Parrotta, J. A., Asbury, C. E., … Fetcher, N. (1995). Nitrogen Immobilization by Decomposing Woody Debris and the Recovery of Tropical Wet Forest from Hurricane Damage. *Oikos*, *72*(3), 314–322.

Zimmerman, J. K., Hogan, J. A., Shiels, A. B., Bithorn, J. E., Carmona, S. M., & Brokaw, N. (2014). Seven-year responses of trees to experimental hurricane effects in a tropical rainforest, Puerto Rico. *Forest Ecology and Management*, *332*, 64–74. https://doi.org/10.1016/j.foreco.2014.02.029

Zwoliński, Z. (1992). Sedimentology and geomorphology of overbank flows on meandering river floodplains. *Geomorphology*, *4*(6), 367–379. https://doi.org/10.1016/0169-555X(92)90032-J